

The EUMETSAT Network of Satellite Application Facilities	 NWP SAF Numerical Weather Prediction	RTTOV-11 Science and Validation Report	Doc ID : NWPSAF-MO-TV-032 Version : 1.1 Date : 16/8/2013
---	--	---	--

RTTOV-11 SCIENCE AND VALIDATION REPORT

**Roger Saunders¹, James Hocking¹, David Rundle¹, Peter Rayer¹,
Marco Matricardi², Alan Geer², Cristina Lupu²,
Pascal Brunel³, Jérôme Vidot³**

Affiliations:

¹*Met Office, U.K.*

²*European Centre for Medium Range Weather Forecasts*

³*MétéoFrance*

This documentation was developed within the context of the EUMETSAT Satellite Application Facility on Numerical Weather Prediction (NWP SAF), under the Cooperation Agreement dated 1 December, 2006, between EUMETSAT and the Met Office, UK, by one or more partners within the NWP SAF. The partners in the NWP SAF are the Met Office, ECMWF, KNMI and Météo France.

Copyright 2013, EUMETSAT, All Rights Reserved.

Change record			
Version	Date	Author / changed by	Remarks
0.1	23/1/13	R W Saunders	First draft version requesting input from partners
0.2	30/1/13	R W Saunders	Added Lambertian reflection section
0.3	26/7/13	R W Saunders	Incorporated other inputs
1.0	1/8/13	R W Saunders	Comments on final draft incorporated
1.1	16/8/13	R W Saunders	Added 2 references for SSU section

<p>The EUMETSAT Network of Satellite Application Facilities</p>		<p>RTTOV-11 Science and Validation Report</p>	<p>Doc ID : NWPSAF-MO-TV-032 Version : 1.1 Date : 16/8/13</p>
---	---	---	---

Table of contents

TABLE OF CONTENTS	2
1. INTRODUCTION AND DOCUMENTATION.....	3
2. SCIENTIFIC CHANGES FROM RTTOV-10 TO RTTOV-11.....	3
2.1 <i>VISIBLE/NIR SIMULATIONS</i>	4
2.2 <i>A NEW LAND SURFACE BRDF ATLAS.....</i>	19
2.2.1 <i>Validation of the VIS/NIR land surface reflectance.....</i>	20
2.3 <i>UPDATES TO PC-RTTOV.....</i>	21
2.4 <i>ADDITION OF NEW AEROSOL SCATTERING COEFFICIENTS</i>	23
2.4.1 <i>Volcanic ash</i>	23
2.4.2 <i>Asian dust</i>	24
2.5 <i>A NEW PARAMETERISATION OF ICE CLOUD OPTICAL PROPERTIES IN THERMAL INFRARED.....</i>	24
2.5.1 <i>Validation of New Parameterisation of Ice Cloud Optical Properties in Thermal Infrared</i>	26
2.6 <i>NON-LTE FOR IR SOUNDERS.....</i>	28
2.6.1 <i>Introduction</i>	28
2.6.2 <i>Calculating Non-LTE radiances</i>	29
2.6.3 <i>Obtaining a radiance correction</i>	30
2.7 <i>LAMBERTIAN SURFACE REFLECTANCE</i>	32
2.8 <i>IMPROVED SSU SIMULATIONS</i>	35
2.9 <i>OPTIMISING NUMBER OF LEVELS IN RADIOMETER COEFFICIENT FILES</i>	38
2.10 <i>MODIFICATIONS TO PROFILE INTERPOLATION</i>	41
2.11 <i>REFINEMENTS IN THE LINE-BY-LINE TRANSMITTANCE DATABASES</i>	43
2.11.1 <i>Infrared transmittances</i>	43
2.11.2 <i>Microwave transmittances.....</i>	45
2.12 <i>CHANGES TO THE MICROWAVE SCATTERING CODE FOR RTTOV-11.....</i>	45
3. TESTING AND VALIDATION OF RTTOV-11.....	46
3.1 <i>VALIDATION OF TOP OF ATMOSPHERE RADIANCES</i>	47
3.1.1 <i>Comparison of simulations.....</i>	47
3.1.2 <i>Comparison with observations</i>	51
3.2 <i>COMPARISON OF JACOBIANS</i>	55
4. SUMMARY.....	57
5. ACKNOWLEDGEMENTS.....	58
6. REFERENCES	58

<p>The EUMETSAT Network of Satellite Application Facilities</p>		<p>RTTOV-11 Science and Validation Report</p>	<p>Doc ID : NWPSAF-MO-TV-032 Version : 1.1 Date : 16/8/13</p>
---	---	---	---

1. Introduction and Documentation

The purpose of this report is to document the scientific aspects of the latest version of the NWP SAF fast radiative transfer model, RTTOV v11.1, referred to hereafter as RTTOV-11, which are different from the previous model RTTOV-10.2 and present the results of the validation tests which have been carried out. The enhancements to this version, released in June 2013, have been made as part of the activities of the EUMETSAT NWP-SAF. The RTTOV-11 software is available at no charge to users on request from the NWP SAF web site. The licence agreement to complete is on the NWP SAF web site at: http://research.metoffice.gov.uk/research/interproj/nwpsaf/request_forms/. The RTTOV-11 documentation, including the latest version of this document can be viewed on the NWP SAF web site at: <http://research.metoffice.gov.uk/research/interproj/nwpsaf/rtm/index.html> which may be updated from time to time. Technical documentation about the software and how to run it can be found in the RTTOV-11 user's guide which can be downloaded from the link above and is provided as part of the distribution file to users.

The baseline document for the original version of RTTOV is available from ECWMF as Eyre (1991) and the basis of the original model is described in Eyre and Woolf (1988). This was updated for RTTOV-5 (Saunders *et al.* 1999a, Saunders *et al.*, 1999b) and for RTTOV-6, RTTOV-7, RTTOV-8 and RTTOV-9 (Matricardi *et al.*, 2004) with the respective science and validation reports for each version hereafter referred to as R7REP2002, R8REP2006, R9REP2008, R10REP2010 respectively all available from the NWP SAF web site at the link above. The changes described here only relate to the scientific differences from RTTOV-10.2. For details on the technical changes to the software, user interface etc. the reader is referred to the RTTOV-11 user manual available from the RTTOV-11 web pages linked from: http://research.metoffice.gov.uk/research/interproj/nwpsaf/rtm/rtm_rtov11.html.

This document also describes comparisons and validations of the output values from this new version of the model by comparing with previous versions, other models and observations. Only aspects related to new and improved science are presented in this report. Many of the details of the science and validation are given in other reports which are referenced in this document and so only a summary is presented here in order to keep this document manageable in size.

2. Scientific Changes from RTTOV-10 to RTTOV-11

The main scientific changes from RTTOV-10 to RTTOV-11 are described below in detail. In summary they are:

- Extension of wavelength range which can be simulated to include visible and near infrared channels simulations.
- New land surface bidirectional reflectance distribution function (BRDF) atlas to specify input surface reflectance for visible channel simulations
- Improved profile interpolation from user levels to RTTOV coefficient levels and back again
- Improved definition of RTTOV coefficient file levels for IR and MW radiometers
- New volcanic ash and Asian dust aerosol scattering parameters.
- New Baran parameterisation for ice particle optical parameters
- Capability to include non-LTE effects for high resolution IR sounders
- Option to treat surface as a Lambertian reflector for the reflected downwelling radiance

		RTTOV-11 Science and Validation Report	Doc ID : NWPSAF-MO-TV-032 Version : 1.1 Date : 16/8/13
---	---	---	--

- PC-RTTOV can now be run over clear and cloudy ocean and for IASI PCs can now be computed for limited spectral bands
- All IR coefficients updated with latest spectroscopy from LBLRTMv12.2 and AER 3.2
- Updated SSU coefficients based on latest spectroscopy LBLRTMv12.0 and option to allow for changes in cell pressure
- Updated HIRS and AMSU-A spectral responses used to provide alternative coefficients which should provide more accurate simulations
- Minor improvements to microwave scattering code

All technical changes (e.g. code improvements, optimisation) between RTTOV-10.2 and v11 are given in the user guide and performance test report.

2.1 *Visible/NIR simulations*

RTTOV v9 introduced the capability to include the effects of solar radiation in short-wave IR channels for IASI and AIRS (Matricardi 2003, Matricardi 2005). This required the use of a new set of predictors, denoted “v9 predictors”, which were selected to give good performance when trained over the wider range of zenith angles required when considering solar illumination.

RTTOV v11 extends this capability to simulate satellite channels for any instrument channel down to 0.4 μ m. The optical depth calculation is based on the same predictor scheme described in Matricardi (2003). For non-hyperspectral visible/near-IR/IR instruments the only variable trace gases allowed for in the coefficients are water vapour and ozone. The existing “v7 predictor” coefficient files are still valid and useful for these instruments and may be found to offer superior performance if visible/near-IR channel simulations are not required (see section 2.1.1).

The new v9 predictor solar coefficient files allow simulations for satellite and solar zenith angles up to 84° which may be useful for geostationary instruments. By default solar radiation may be included for channels below 5 μ m. However it is possible to include the effects of solar illumination in IR window channels if desired: sun-glint has been observed to affect such channels over ocean surfaces. The user guide describes how to enable this.

For the purposes of RTTOV solar simulations, channels below 3 μ m are classed as visible/near-IR (VIS/NIR). For these channels *only* solar radiation is included in the simulations for efficiency: emitted (thermal) radiation is ignored. The line-by-line calculations used to derive the coefficients for the optical depth calculation account for extinction due to atmospheric (clear-sky) Rayleigh scattering. For channels below 2 μ m the RTTOV simulations include a parameterisation for clear-sky atmospheric Rayleigh single-scattering into the satellite line-of-sight (described in section 2.1.2).

Note that very broad channels such as the SEVIRI High-Resolution Visible (HRV) channel are not simulated well due to the large spectral variation in the solar source function (and potentially also surface reflectance) across the channel.

The internal surface reflectance scheme for sea surfaces is described in Matricardi (2003). Over land surfaces a bi-directional reflectance function (BRDF) atlas has been developed which is described in section 2.2.

The simple cloudy scheme which takes as input a single cloud top pressure and cloud fraction has been extended to VIS/NIR channels (see section 2.1.3). This is intended for qualitative applications.

Finally, the single scattering parameterisation for aerosols and clouds has also been extended to VIS/NIR channels (see section 2.1.4). At shorter wavelengths the single-scattering assumption begins to break down, particularly for water clouds which exhibit very strong scattering at visible wavelengths. This can result in very large biases in the simulated radiances. Therefore the current VIS/NIR scattering implementation should be considered experimental: more details are provided below. It is planned to investigate possibilities for a more accurate scheme in a future version of RTTOV.

2.1.1 v7 vs v9 predictors

This section provides some indication of the relative performance of v7 and v9 predictors for IR channels (no solar radiation). Simulations were performed for the eight SEVIRI infra-red channels using recent forecast data as input to RTTOV. Clear-sky radiances are compared to observations and the differences are shown below.

Figure 1 shows the mean, standard deviation and RMSE of observations minus simulations using the 54-level v7 and v9 predictor RTTOV coefficient files for the 00 UTC slot on 26th May 2013. Only clear-sky pixels up to satellite zenith angles of 65° are included in the statistics: this zenith angle was chosen as it is the maximum used in the training of the v7 predictor coefficients. Simulations were carried out for every fourth SEVIRI pixel horizontally and vertically using spatially interpolated NWP atmospheric and surface fields.

Figure 2 shows the differences between the v7 and v9 O-B statistics: positive values imply v9 predictors are better and negative values imply v7 predictors are better. The dashed boxes show the NEdT in each SEVIRI channel.

The results for this slot are broadly representative of the general case. The most important point to note is that the standard deviation of the O-B is very similar between the v7 and v9 predictors and the difference is well within the instrument noise. The v9 predictors show a larger bias in the water vapour channels (5 and 6) compared to the v7 predictors although the difference is again within the channel noise level. The v9 predictors show a significantly lower bias in the CO₂ channel (11) than the v7 predictors.

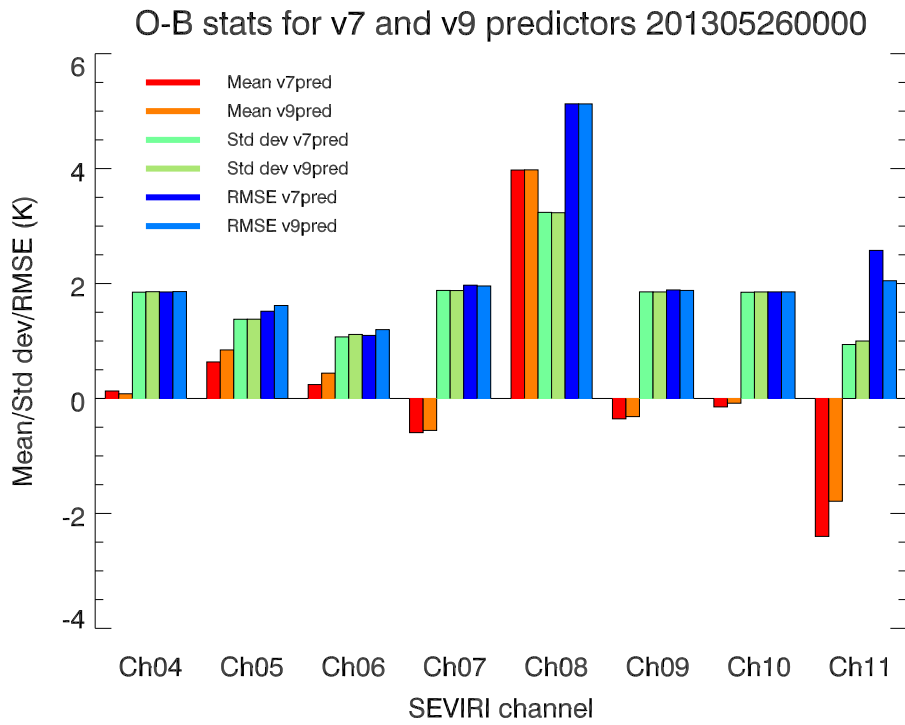


Figure 1: statistics for observed minus simulated brightness temperatures for clear-sky pixels for the 8 IR SEVIRI channels for a single SEVIRI image

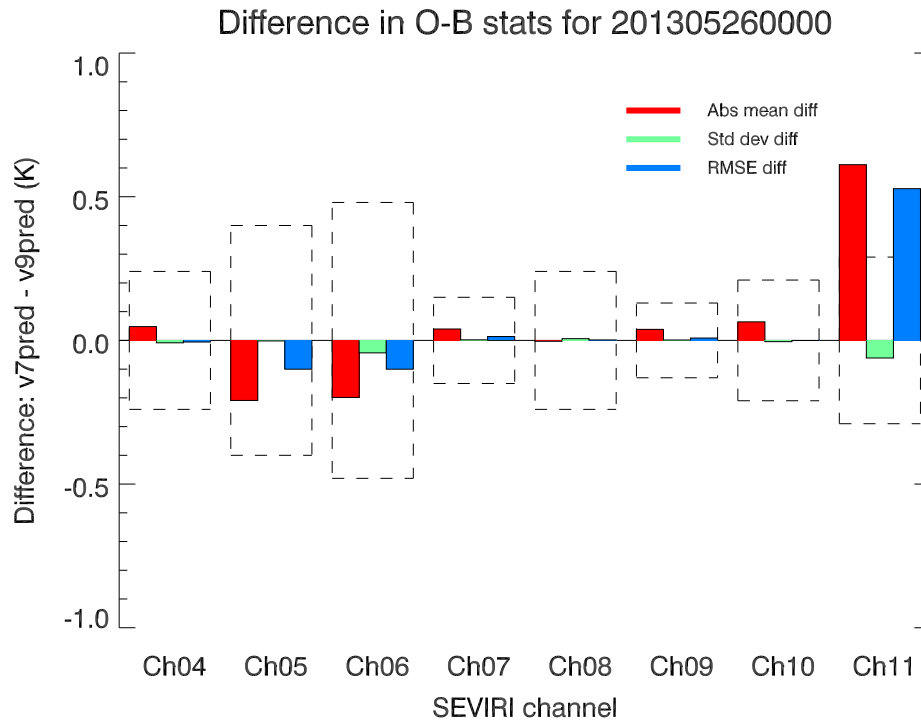


Figure 2: differences between the v7 and v9 statistics in Figure 1. Dashed boxes show the NEdT for each SEVIRI channel.

2.1.2 Clear-sky simulations (Rayleigh scattering)

Atmospheric (clear-sky) Rayleigh scattering has a significant effect on radiances at visible wavelengths. To account for this a simple single-scattering parameterisation has been implemented and is applied to channels below $2\mu\text{m}$.

Bucholzt (1995) gives the Rayleigh scattering cross-section as:

$$\sigma_s = \frac{24\pi^3 (n_s^2 - 1)^2}{\lambda^4 N_s^2 (n_s^2 + 2)^2} \left(\frac{6 + 3\rho_n}{6 - 7\rho_n} \right) \quad (2.1.1)$$

where λ is the wavelength, n_s is the refractive index of standard air at λ , N_s is the molecular number density $2.54743 \times 10^{19} \text{ cm}^{-3}$ for standard air, and ρ_n is the depolarization factor - a term that accounts for the anisotropy of the air molecule and that varies with wavelength. Standard air is defined as dry air containing 0.03% CO₂ by volume at normal pressure 1013.25 hPa and having an air temperature of 288.15K.

Bucholzt gives an analytic formula for σ_s (in units of cm^2) which fits eq (2.1.1) to within 0.2% for wavelengths in the range 0.25 - $0.5\mu\text{m}$ and to within 0.1% for wavelengths greater than $0.5\mu\text{m}$:

$$\sigma_s = A\lambda^{-(B+C\lambda+D/\lambda)} \quad (2.1.2)$$

where λ is given in μm and the coefficients A - D are given in Table 1:

Coefficient	$0.2 < \lambda \leq 0.5\mu\text{m}$	$\lambda > 0.5 \mu\text{m}$
A	3.01577×10^{-28}	4.01061×10^{-28}
B	3.55212	3.99668
C	1.35579	1.10298×10^{-3}
D	0.11563	2.71393×10^{-2}

Table 1: Coefficients for Rayleigh scattering

The phase function for Rayleigh scattering can be approximated as:

$$P(\Theta) = \frac{3}{4}(1 + \cos^2 \Theta) \quad (2.1.3)$$

for scattering angle Θ . This does not take account of molecular anisotropy (which is wavelength dependent) which results in differences of around 1.5% at the forward and backward scattering angles and at scattering angles around 90° . The scattering angle is given by:

$$\cos \Theta = \cos \theta_{sat} \cos \theta_{sol} + \sin \theta_{sat} \sin \theta_{sol} \cos(\phi_{sat} - \phi_{sol}) \quad (2.1.4)$$

where θ_{sat} and θ_{sol} are the local satellite and solar zenith angles, and ϕ_{sat} and ϕ_{sol} are the local satellite and solar azimuth angles.

The upwelling and downwelling source terms (J^\uparrow and J^\downarrow) due to Rayleigh scattering of the direct solar beam at (monochromatic) wavelength λ from a thin slice of atmosphere of vertical depth dz at height z are given by:

<p>The EUMETSAT Network of Satellite Application Facilities</p>		<p>RTTOV-11 Science and Validation Report</p>	<p>Doc ID : NWPSAF-MO-TV-032 Version : 1.1 Date : 16/8/13</p>
---	---	---	---

$$J^{\uparrow/\downarrow}(\lambda, \theta_{sat}, \theta_{sun}) = F_{sun} \tau_{sun} \frac{P(\Theta^{\uparrow/\downarrow})}{4\pi} \sigma_s N(z) \frac{dz}{\cos \theta_{sat}} \quad (2.1.5)$$

where F_{sun} is the solar irradiance at the top of the atmosphere, τ_{sun} is the transmittance from the sun to the level at height z , $N(z)$ is the number of particles per unit volume at height z , and θ_{sat} is the local satellite zenith angle. The phase function is evaluated for the upward (Θ^{\uparrow}) and downward (Θ^{\downarrow}) scattering angles along the satellite line-of-sight. The factor of $1/4\pi$ normalises the phase function. (Note the dependence on the relative sun-satellite azimuth angle is omitted for clarity).

The Rayleigh contribution to the total clear-sky radiance is then given by:

$$L(\lambda, \theta_{sat}, \theta_{sun}) = \int_{\tau_s}^1 J^{\uparrow}(\lambda, \theta_{sat}, \theta_{sun}) d\tau + r_s(\lambda, \theta_{sat}) \tau_s^2 \int_{\tau_s}^1 \frac{J^{\downarrow}(\lambda, \theta_{sat}, \theta_{sun})}{\tau^2} d\tau \quad (2.1.6)$$

where τ_s is the surface-to-space transmittance along the satellite line-of-sight and $r_s(\lambda, \theta_{sat})$ is the surface reflectance for the downward incoming radiance and upward outgoing radiance along the satellite line-of-sight. In fact this value is not available within RTTOV so the input BRDF for the incoming solar and outgoing satellite surface zenith angles (multiplied by the cosine of the satellite zenith angle) is used instead. In general this should not cause significant errors since the surface-reflected downwelling radiation is very much smaller in magnitude than the upward-scattered component.

In practice the upwelling and downwelling contributions are calculated for each layer of the input user level profile. The solar and satellite angles (and hence the phase function) are assumed constant through each layer. We obtain a value for the source term for atmospheric layer i (bounded by levels i and $i+1$) by integrating eq (2.1.5) over the layer:

$$J_i^{\uparrow/\downarrow}(\lambda, \theta_{sat}, \theta_{sun}) = F_{sun} \tau_{sun,i} \frac{P(\Theta_i^{\uparrow/\downarrow})}{4\pi} \frac{\sigma_s}{\cos \theta_{sat,i}} \int_{z_{i+1}}^{z_i} N(z') dz' \quad (2.1.7)$$

where $\tau_{sun,i}$ is the transmittance from space to level i , $\Theta_i^{\uparrow/\downarrow}$ are the upward and downward scattering phase functions calculated for layer i , and $\theta_{sat,i}$ is the satellite zenith angle in layer i , and z_i is the height of level i . Using the hydrostatic equation we obtain an expression for the integrated particle number density over layer i :

$$\int_{z_{i+1}}^{z_i} N(z') dz' = \frac{N_A (p(z_{i+1}) - p(z_i))}{g M_i} \quad (2.1.8)$$

where N_A is Avogadro's constant, $p(z_i)$ is the pressure at level i , g is the acceleration due to gravity (assumed constant throughout the atmosphere) and M_i is the average molar mass of layer i . Thus the upwelling and downwelling Rayleigh source terms for each layer are expressed in quantities that are either available or easily calculable within RTTOV.

Figures 3 and 4 below show the difference and relative difference between the simulated and observed reflectances (bi-directional reflectance factors, BRFs) for SEVIRI channels 1, 2 and 3

(0.6, 0.8 and 1.6 μm respectively) as a function of solar zenith angle. Plots are shown for two slots for which the simulated radiances were calculated for every fourth SEVIRI pixel. Only clear-sky pixels over sea surfaces away from sun glint are included: in this case *calcrefl* was set to true so that for these pixels the only contribution to the simulated radiances comes from the Rayleigh scattering as the calculated sea surface reflectance away from sun glint is zero. The thick lines represent the mean differences, and the thin lines show the mean \pm one standard deviation.

The simulated reflectances show a small consistent negative bias compared to the observations which is not unexpected: the Rayleigh scheme would be expected to under-estimate the contribution due to clear-sky Rayleigh scattering as it does not account for diffuse radiation. In addition, the inclusion of some undetected cloudy pixels and the fact that the true surface reflectance is slightly greater than zero will also contribute to the observed bias. The absolute differences are relatively stable up to solar zenith angles of around 70-80°. The relative differences are reasonably consistent across all solar zenith angles.

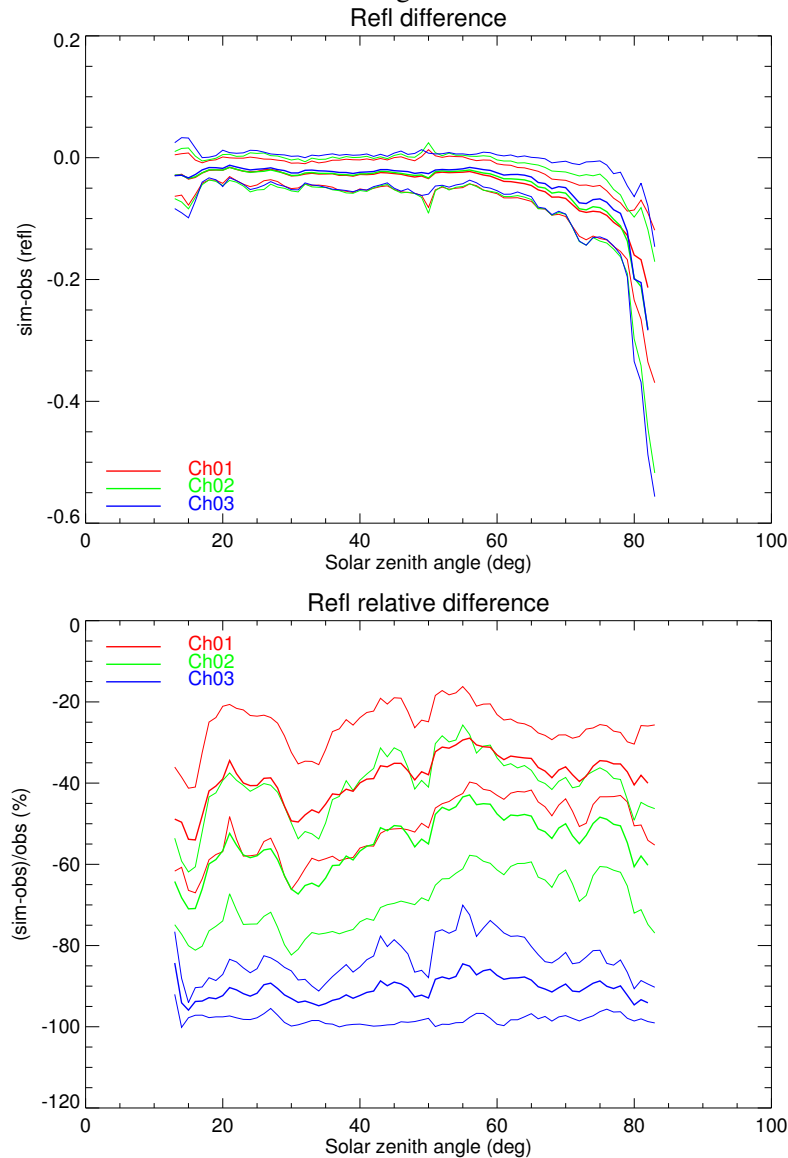


Figure 3: Absolute and relative differences between clear sky simulated and observed reflectances for SEVIRI channels 1, 2 and 3 for 1200UTC 26th May 2013.

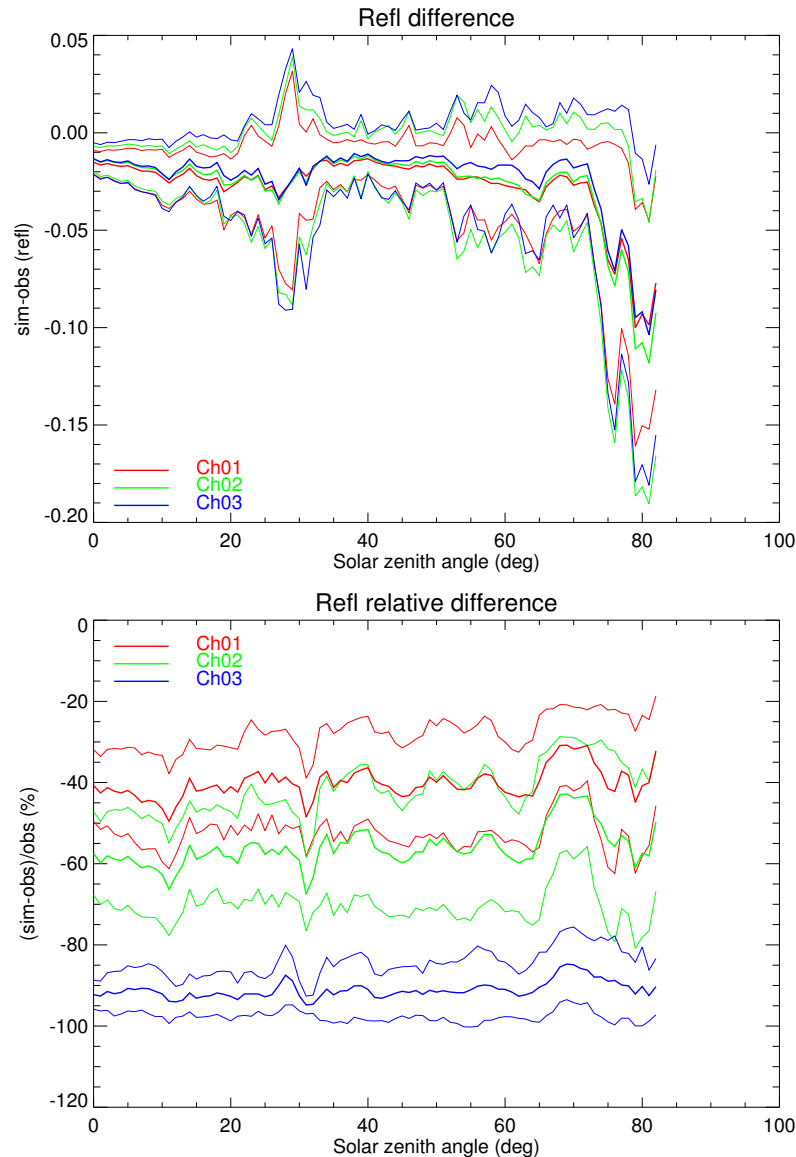


Figure 4: Absolute and relative differences between clear sky simulated and observed reflectances for SEVIRI channels 1, 2 and 3 for 1500UTC 23rd May 2013.

2.1.3 Simple cloudy simulations

The simple cloud scheme takes as input a cloud top pressure and cloud fraction and returns the linear combination of clear-sky and 100% cloudy radiances weighted according to the cloud fraction. For IR channels the cloudy radiances are calculated assuming the cloud top is perfectly emissive and therefore no solar contribution is included for any channels down to $3\mu\text{m}$. For VIS/NIR channels (i.e. below $3\mu\text{m}$), the cloud top is treated as a Lambertian surface with default BRDF values of $0.7/\pi$ for channels below $1\mu\text{m}$ and $0.6/\pi$ for channels above $1\mu\text{m}$. It is possible to specify alternative values for the cloud top BRDF for each simulated channel when calling RTTOV. The resulting radiances comprise the solar radiation directly reflected from the cloud top and the contribution of atmospheric Rayleigh scattering above the cloud.

Figures 5 and 6 show observed and simulated examples for SEVIRI channels 1 ($0.6\mu\text{m}$) and 3 ($1.6\mu\text{m}$). The cloud top pressure and cloud fraction used for the simulated images were retrieved from the operational SEVIRI processing system at the Met Office.

The simulations typically underestimate the reflectance of high cumulous cloud tops, while the reflectance of lower water cloud is overestimated. Ice cloud appears too bright in both channels. At $0.6\mu\text{m}$ the effective cloud fractions input to RTTOV may be too large, failing to account for the semi-transparent nature of cirrus. At $1.6\mu\text{m}$ ice cloud is much too bright in the simulated images because the default cloud top reflectance does not take account of the difference in reflectivity between water and ice clouds at this wavelength. Results for the $0.8\mu\text{m}$ channel are very similar to those for the $0.6\mu\text{m}$ channel and hence are not shown. Due to the simplistic assumptions of this scheme it is primarily intended for qualitative rather than quantitative applications.

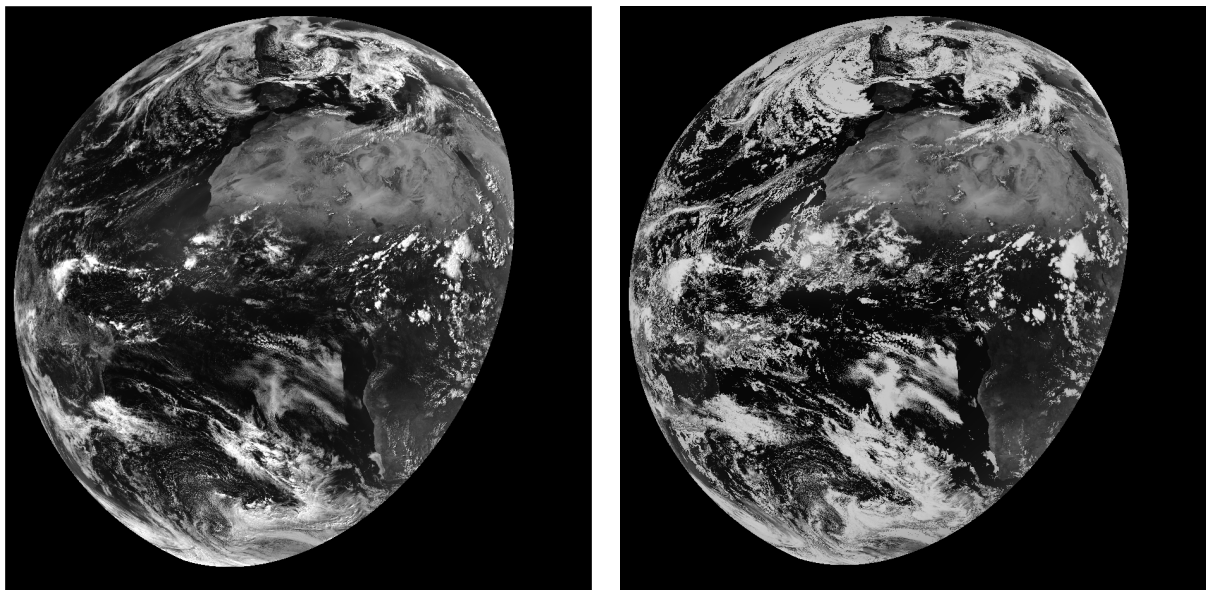


Figure 5: SEVIRI $0.6\mu\text{m}$ observed (left) and simulated (right) reflectances using the simple cloud scheme for 1500UTC 23rd May 2013.

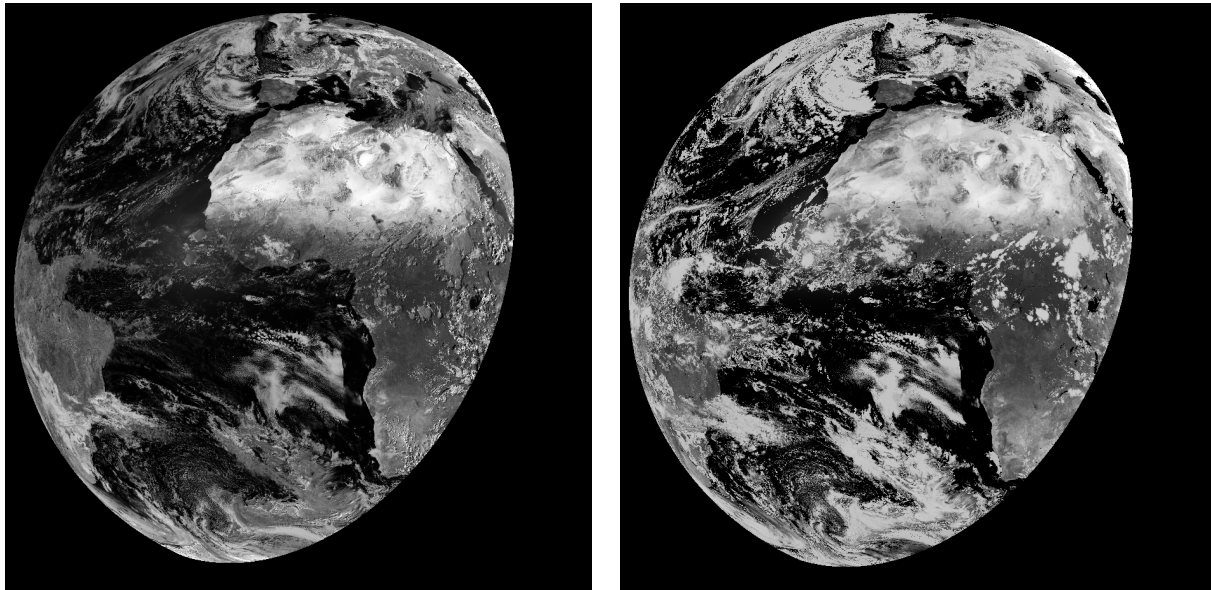


Figure 6: SEVIRI 1.6 μ m observed (left) and simulated (right) reflectances using the simple cloud scheme for 1500UTC 23rd May 2013.

2.1.4 Scattering simulations

The existing solar single-scattering capability for short-wave AIRS and IASI channels (Matricardi 2005) has been applied to VIS/NIR channels. The only difference in the implementation to that described in the reference is that the phase functions are no longer azimuthally averaged, but instead are interpolated to the specific scattering angles determined by the sun and satellite angles as this gives better results for the single-scattering parameterisation (see below).

The failure to account for multiple-scattering leads to significant errors for strongly-scattering particles and this is especially true at shorter wavelengths. In particular water cloud particles are so strongly scattering that the resulting radiances exhibit very large errors indeed. The same is true for some of the pre-defined RTTOV aerosol particle types. For this reason no aerosol or cloud coefficient files have been created for use with the v9 predictor solar optical depth coefficient files (except for the existing AIRS and IASI coefficient files). Instead the solar scattering calculations must be carried out by supplying profiles of the scattering parameters explicitly as described in the user guide.

A further caveat of the solar scattering simulations is that in a forward scattering geometry (i.e. where the satellite and solar zenith angles are very similar and the relative sun-satellite azimuth angle is very small) there is a very strong positive bias in the simulations which results from the strong forward peak in the phase function. This effect typically increases with shorter wavelengths. With azimuthal averaging of phase functions, the impact of the forward peak was spread to all cases where the zenith angles were similar, regardless of relative azimuth, and so this was a motivating factor for modifying the v10 scattering implementation as noted above.

In order to evaluate the scattering scheme, comparisons of RTTOV and DISORT were made for solar scattering simulations in SEVIRI channels 1-3 (0.6 μ m, 0.8 μ m and 1.6 μ m). A copy of RTTOV was modified to call DISORT instead of the *rttov_integrate* subroutine which carries out the integration of the radiative transfer equation. The DISORT simulations used the optical depths calculated by RTTOV. The coefficients for the Legendre expansions of the phase functions were

derived from the phase functions recalculated at high angular resolution to ensure a good fit of the resulting polynomial expansion to the original. The surface is treated as a Lambertian reflector by DISORT with BRDF given by that input to RTTOV.

For the RTTOV simulations the clear-sky Rayleigh scattering parameterisation (described in 2.1.2) was excluded from the simulations as this was not included in the DISORT simulations.

Simulations were run for satellite and solar zenith angles between 0° and 60° in steps of 10°. Surface BRDFs were either 0.1 or 0.01: the smaller the surface BRDF the higher the ratio of aerosol signal to surface reflected signal, so the tests using the lower BRDF value give a better indication of the errors in the scattering parameterisation.

Simulations were run separately for two fixed phase functions corresponding to the insoluble (INSO) and water soluble at 99% relative humidity (WASO) particle types for which pre-calculated parameters are available in RTTOV. The INSO phase functions have a much stronger forward peak than the WASO ones (see figure 7).

The simulations were run for a 54 level input profile with a fixed number density profile representing a homogenous aerosol layer between around 600 and 900 hPa. The absorption (*abs*) and scattering (*sca*) parameters were varied to investigate the sensitivity of the RTTOV-DISORT differences to overall aerosol density (controlled here by the magnitude of *abs* and *sca*) and the single scattering albedo (controlled by the ratio *abs:sca*).

In general it is expected that for stronger scattering the RTTOV parameterisation will show larger differences to the DISORT simulations, and the RTTOV reflectances should be smaller than the DISORT ones since the RTTOV calculations omit the contribution from multiple-scattering. This is indeed what is found: as the single scattering albedo (SSA) increases, the absolute RTTOV-DISORT differences increase, and as the overall aerosol density increases (regardless of SSA) the differences increase. The exception is in the forward scattering case (noted above) where the RTTOV reflectances are much higher as a result of the forward peak in the phase function.

Figures 8-15 below show the relative difference between RTTOV and DISORT reflectances calculated as (RTTOV-DISORT)/DISORT over a range of satellite and solar zenith angles for the INSO phase functions. For this set of tests the relative azimuth angle was set to 90°. Note that the colour scale varies from plot to plot according to the size of the differences.

The input aerosol number density was 5.0cm⁻³. The *abs* and *sca* parameters used are given in table 2 below. Tests 01 and 02 use equal values for *abs* and *sca* with different magnitudes, representing medium and high aerosol concentrations. Tests 11 and 12 have *abs* << *sca* to test larger SSA values.

Test number	<i>abs</i> (cm ⁻¹)	<i>sca</i> (cm ⁻¹)
01	0.001	0.001
02	0.1	0.1
11	0.00001	0.01
12	0.00001	0.1

Table 2. Absorption and scattering values used in the tests.

Figures 8 and 9 show good agreement between RTTOV and DISORT for modest aerosol concentrations where the SSA is far from 1.0. Figures 10 and 11 show differences of up to ~50% when the aerosol concentration is high.

Figures 12 and 13 show relative differences of up to ~10% for higher surface reflectance and ~40% for lower surface reflectance with modest aerosol concentration and higher SSA.

Figures 14 and 15 show much larger differences in the case where both the SSA and the aerosol concentration are high.

In all cases the strong bias when both zenith angles are zero is a result of the forward peak of the phase function.

Tests 01 and 11 were repeated with relative azimuth angles of 45°, 135° and 180° using a surface BRDF of 0.01. The results are shown in figures 16-21. For test 01 ($abs = sca$), the differences remain within ~10%. For test 11 ($abs < sca$), the largest differences are around 60%.

Tests 01 and 11 were repeated using the WASO (99% relative humidity) phase function and a surface BRDF of 0.01 with a relative azimuth of 90°. The results are shown in figures 22 and 23. The effect of the smaller forward peaks in the phase functions are evident when comparing the INSO and WASO results, but aside from that the RTTOV-DISORT differences are broadly similar between the phase functions. The impact of varying relative azimuth angle on the WASO simulations (results not shown) is smaller than for INSO which is to be expected as the WASO phase functions vary less with scattering angle.

Since numerous factors contribute to the size of the errors in the RTTOV simulations it is difficult to concisely characterise the errors. It is clear that the existing parameterisation cannot be used effectively for strongly scattering particles or for high particle density. The same conclusions apply to clouds as well as aerosols: for water clouds the strong scattering at VIS/NIR wavelengths results in very large errors rendering the scattering parameterisation essentially unusable. The aim is to investigate an improved parameterisation of solar scattering for a future version of RTTOV.

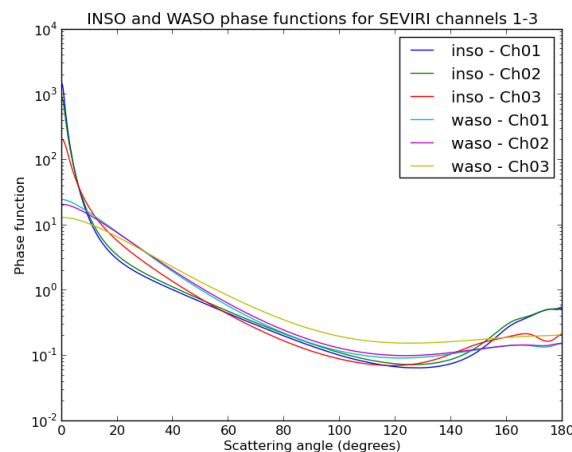


Figure 7: INSO and WASO particle type phase functions for SEVIRI channels 1-3.

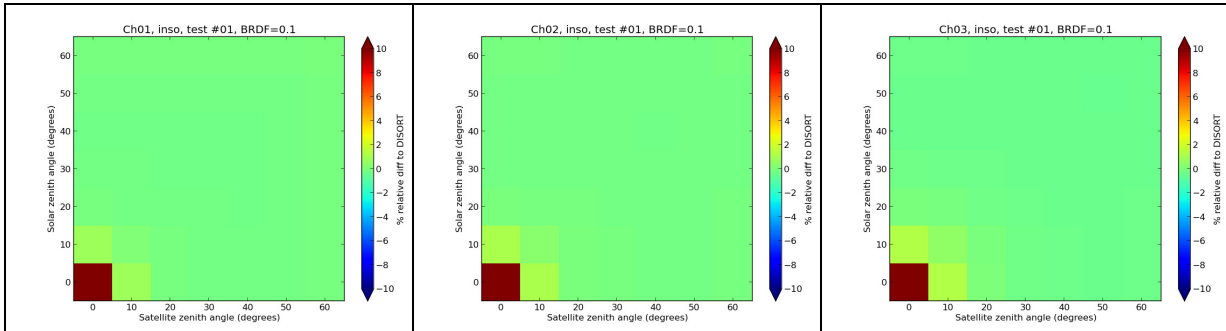


Figure 8: relative difference between DISORT and RTTOV reflectances for test 01 (equal abs and sca) with BRDF=0.1. Note scale: -10% to 10%.

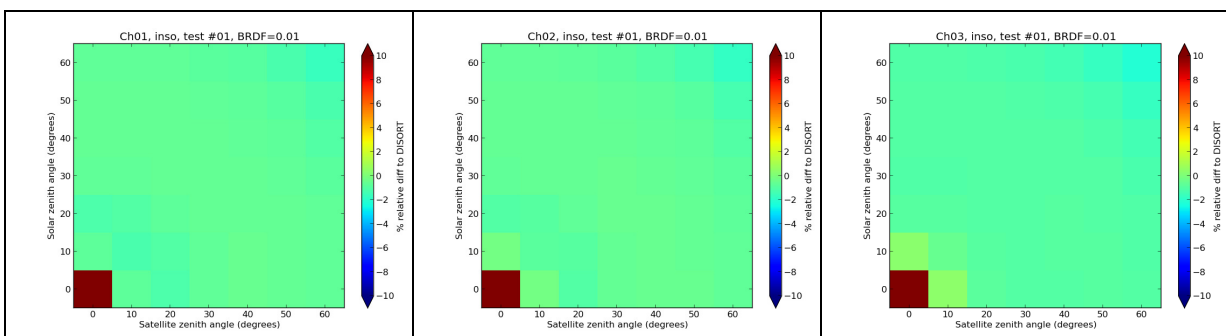


Figure 9: relative difference between DISORT and RTTOV reflectances for test 01 (equal abs and sca) with BRDF=0.01. Note scale: -10% to 10%.

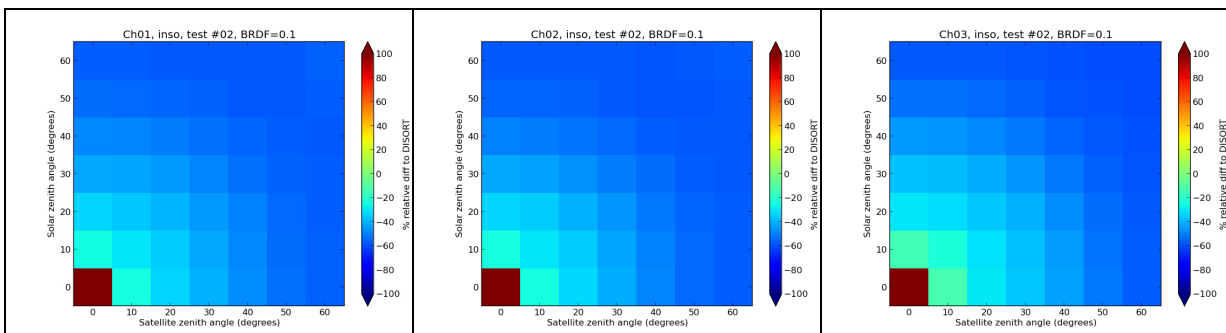


Figure 10: relative difference between DISORT and RTTOV reflectances for test 02 (equal abs and sca, larger value) with BRDF=0.1. Note scale: -100% to 100%.

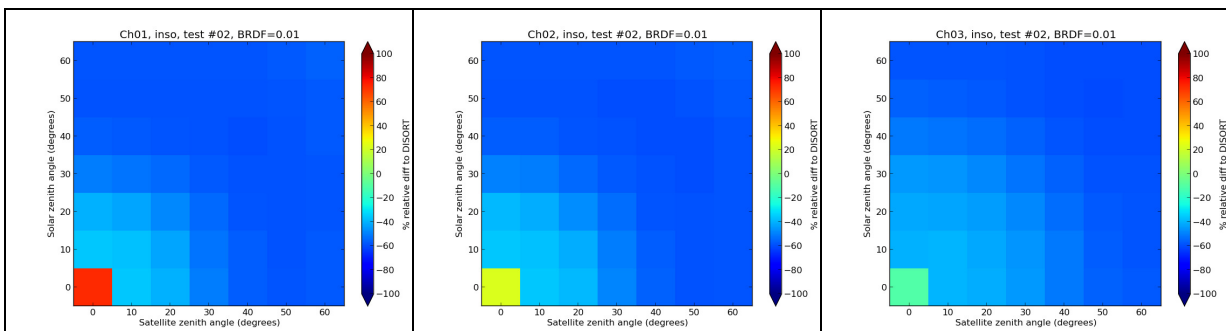


Figure 11: relative difference between DISORT and RTTOV reflectances for test 02 (equal abs and sca, larger value) with BRDF=0.01. Note scale: -100% to 100%.

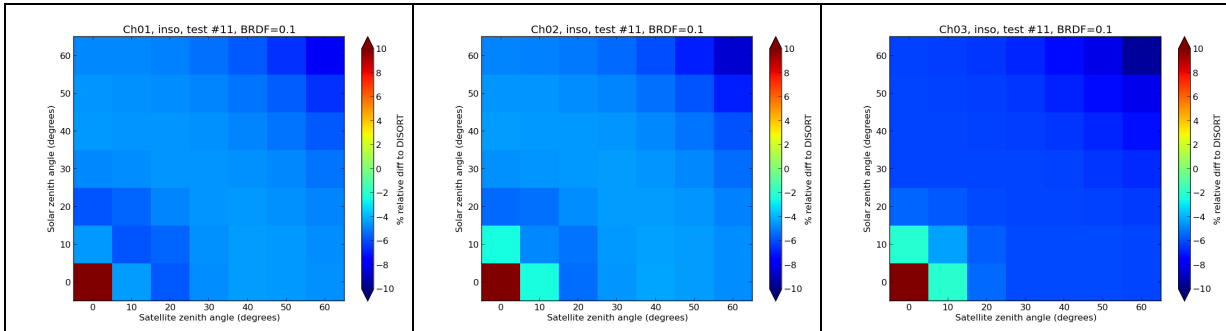


Figure 12: relative difference between DISORT and RTTOV reflectances for test 11 ($abs < sca$) with BRDF=0.1. Note scale: -10% to 10%.

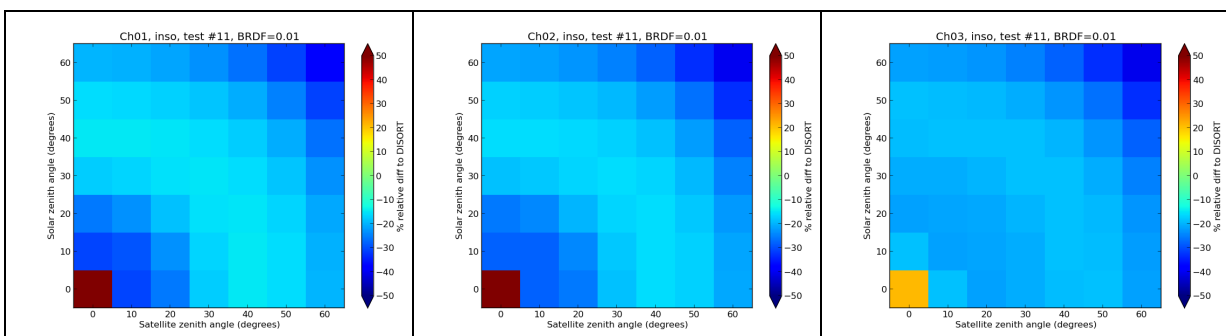


Figure 13: relative difference between DISORT and RTTOV reflectances for test 11 ($abs < sca$) with BRDF=0.01. Note scale: -50% to 50%.

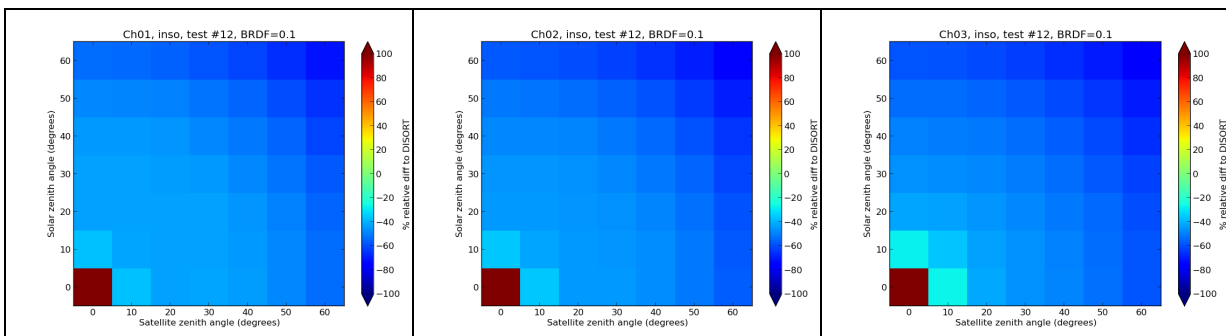


Figure 14: relative difference between DISORT and RTTOV reflectances for test 12 ($abs < sca$, larger sca value) with BRDF=0.1. Note scale: -100% to 100%.

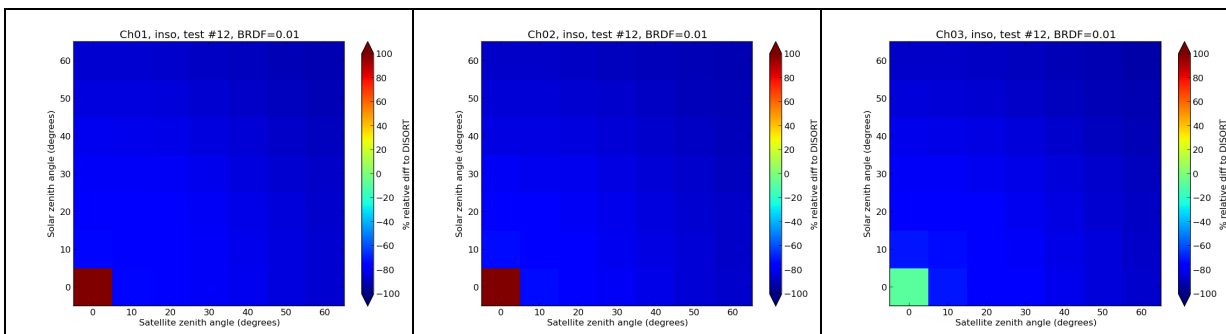


Figure 15: relative difference between DISORT and RTTOV reflectances for test 12 ($abs < sca$, larger sca value) with BRDF=0.01. Note scale: -100% to 100%.

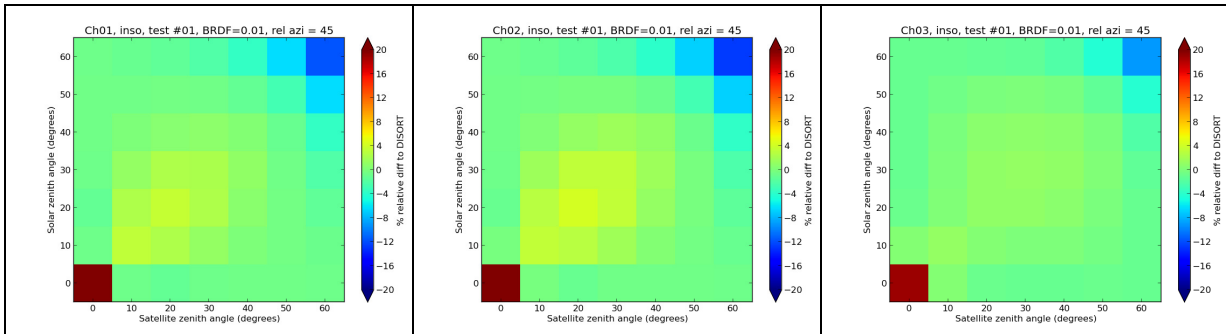


Figure 16: relative difference between DISORT and RTTOV reflectances for test 01 (equal abs and sca) with BRDF=0.01 and rel. azimuth 45°. Note scale: -20% to 20%.

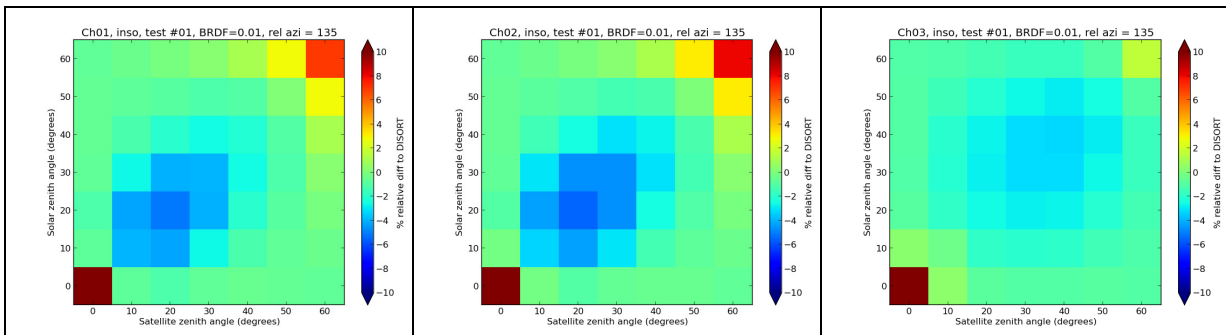


Figure 17: relative difference between DISORT and RTTOV reflectances for test 01 (equal abs and sca) with BRDF=0.01 and rel. azimuth 135°. Note scale: -10% to 10%.

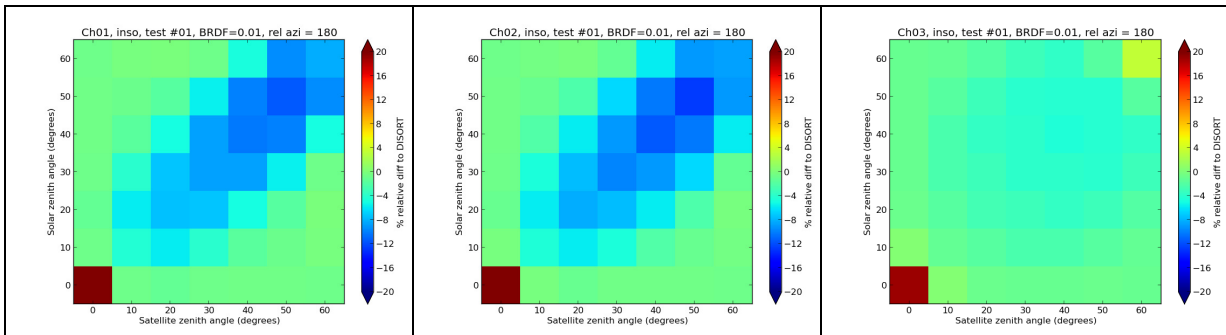


Figure 18: relative difference between DISORT and RTTOV reflectances for test 01 (equal abs and sca) with BRDF=0.01 and rel. azimuth 180°. Note scale: -20% to 20%.

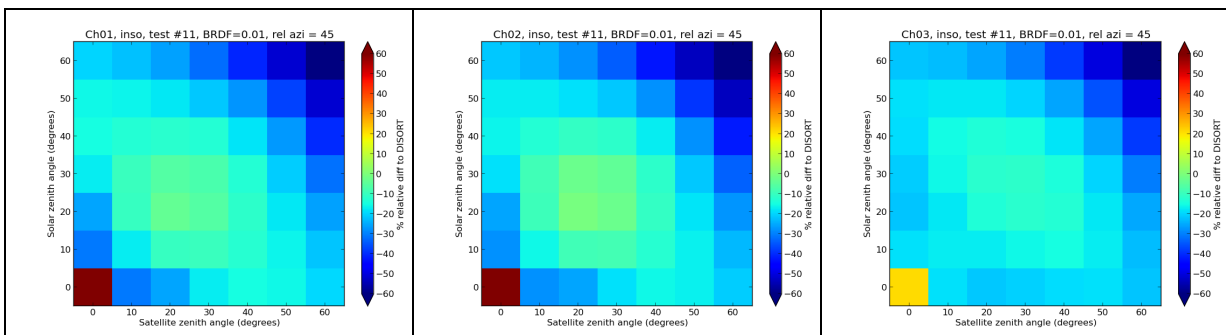


Figure 19: relative difference between DISORT and RTTOV reflectances for test 11 (abs < sca) with BRDF=0.01 and rel. azimuth 45°. Note scale: -60% to 60%.

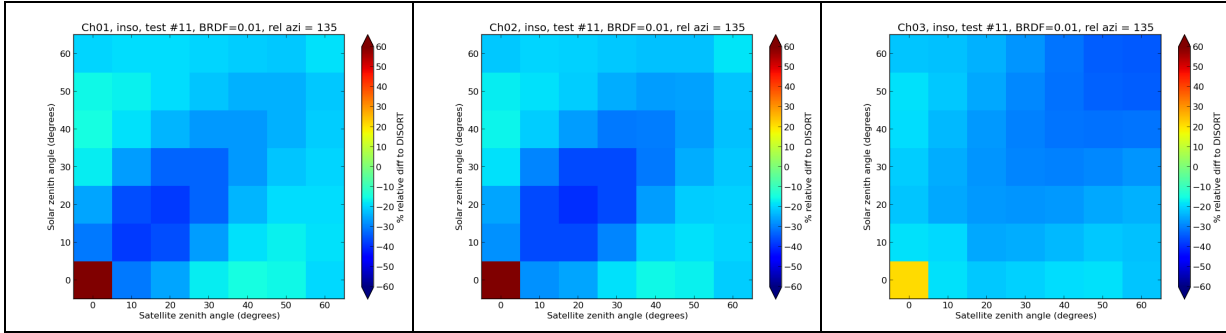


Figure 20: relative difference between DISORT and RTTOV reflectances for test 11 ($abs < sca$) with $BRDF=0.01$ and rel. azimuth 135° . Note scale: -60% to 60%.

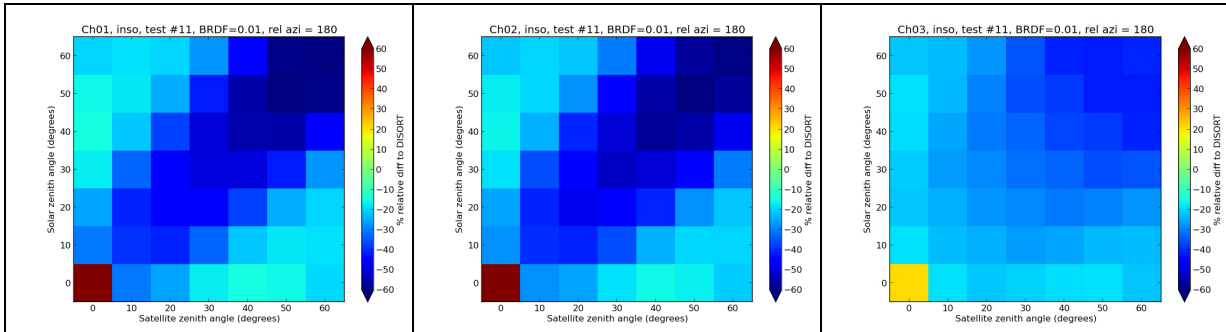


Figure 21: relative difference between DISORT and RTTOV reflectances for test 11 ($abs < sca$) with $BRDF=0.01$ and rel. azimuth 180° . Note scale: -60% to 60%.

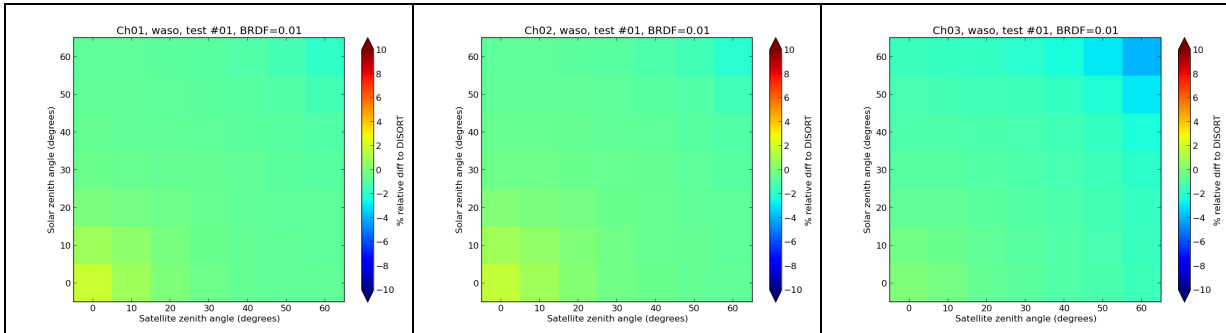


Figure 22: relative difference between DISORT and RTTOV reflectances for test 01 (equal abs and sca) using WASO phase functions with $BRDF=0.01$ and rel. azimuth 90° . Note scale: -10% to 10%.

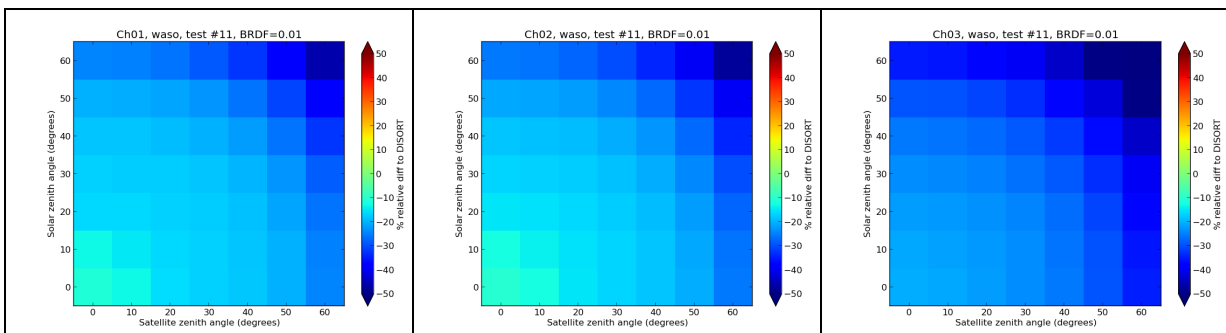


Figure 23: relative difference between DISORT and RTTOV reflectances for test 11 ($abs < sca$) using WASO phase functions with $BRDF=0.01$ and rel. azimuth 90° . Note scale: -50% to 50%.

		RTTOV-11 Science and Validation Report	Doc ID : NWPSAF-MO-TV-032 Version : 1.1 Date : 16/8/13
---	---	---	--

2.2 A new land surface BRDF Atlas

A VIS/NIR land surface reflectance atlas was implemented in RTTOV to describe the spectral and the geometrical dependencies of the surface optical properties needed to simulate TOA radiances in the VIS/NIR. The atlas provides a global (at a spatial resolution of 0.1°) and monthly mean land surface Bidirectional Reflectance Distribution Function (BRDF) for any instrument containing channels with a central wavelength between 0.4 and 2.5 μm , as well as a quality index of the BRDF. The methodology was developed in a similar way to the RTTOV UWIREMIS infrared land surface emissivity atlas (Borbas and Ruston, 2010). The concept is to reconstruct hyperspectral BRDF spectra by constraining/fitting satellite-derived BRDF retrievals at specific channels with the principal components (PC) of a representative set of hyperspectral surface reflectance laboratory spectra. The BRDF of any instrument with channels having central wavelengths in the VIS/NIR is then estimated by interpolation from the reconstructed hyperspectral BRDF spectra.

For this purpose, we used the MODIS MCD43C1 Level 3 BRDF kernel-driven product (Gao *et al.*, 2005). Globally, MODIS products are able to capture the seasonal cycle of snow-free surface albedo with an accuracy lower than 0.05 but are less satisfactory for high solar zenith angles (Liu *et al.*, 2009). The MODIS BRDF is modeled by using the semi empirical linear model of Ross-Li (Lucht *et al.*, 2000) that is given by:

$$R(\theta_{sat}, \theta_{sol}, \Delta\phi, \lambda) = f_{iso}(\lambda) + f_{vol}(\lambda)K_{vol}(\theta_{sat}, \theta_{sol}, \Delta\phi) + f_{geo}(\lambda)K_{geo}(\theta_{sat}, \theta_{sol}, \Delta\phi) \quad (2.2.1)$$

where θ_{sat} , θ_{sol} and $\Delta\phi$ are the satellite zenith angle, the solar zenith angle, and the azimuth difference between satellite and solar directions, respectively; λ is the wavelength. The first BRDF model parameter f_{iso} is due to isotropic scattering. The second BRDF model parameter f_{vol} is due to radiative transfer-type volumetric scattering from horizontally homogeneous leaf canopies. The third BRDF model parameter f_{geo} is due to geometric-optical surface scattering from scenes containing 3-D objects that cast shadows and are mutually obscured from views at off-nadir angles. The collection 5 MODIS product contains three retrieved BRDF model parameters (f_{iso} , f_{vol} and f_{geo}) for each MODIS VIS/NIR channel (at 0.470, 0.555, 0.659, 0.865, 1.24, 1.64 and 2.13 μm) and three associated pieces of information on retrieval quality and inputs.

The representative set of hyperspectral surface reflectance spectra were obtained by selecting 126 spectra (100 spectra for soils, rocks, and mixtures of both and 26 spectra for vegetation) from the United States Geological Survey (USGS) hyperspectral laboratory measurements database (Clark *et al.*, 2007). The central wavelengths of the MODIS channels have been chosen as fitting points for the principal component analysis (PCA) regression method.

The monthly mean RTTOV BRDF atlas was obtained by averaging the best retrievals from MCD43C1 data selected by iterative tests. For that, we combined the MODIS albedo retrieval quality (called hereafter QA), the percentage of inputs between 0% and 100% (called hereafter PI) and the percentage of snow coverage between 0% and 100% (called hereafter PS). The methodology was as follows: For all original MODIS MCD43C1 retrievals within a month, we extracted the information for a 4 by 4 pixel box (from an original MODIS pixel resolution at 0.05° to a final grid at 0.1°). First of all, the land/water mask from the UWIREMIS atlas is used (see Table 3). Then, the first test is applied. If at least one pixel is found within the final grid over a month, the quality index is associated and the values of the three BRDF model parameters f are calculated by the value of the best original pixel or by the mean value if more than one original pixel is found. If no pixel is found, then the second test is applied, and so on until all pixels are tested.

Quality Index	Name	Criteria			Description
		QA	PI	PS	
0	WATER				Land/water mask from UWIREMIS atlas
1	GOOD	0-1	$\geq 80\%$	0%	No snow, best and good MCD43C1 quality for 80% inputs or more
2	MEDIUM	2-3	$\geq 80\%$	0%	No snow, medium MCD43C1 quality for 80% inputs or more
3	LOW	0-4	$< 80\%$	0%	Remaining no snow pixels
4	SNOW	0-4	0-100%	100%	Full snow
5	BAD	0-4	0-100%	$\neq 0\%$ $\neq 100\%$	Remaining pixels containing snow
6	NO DATA				Remaining pixel from land/water mask with no BRDF retrieval

Table 3: Iterative test criteria for the Quality Index and the calculation of the RTTOV BRDF atlas.

The panel of Figure 24 shows the monthly RTTOV BRDF quality index for January 2010 (left) and July 2010 (right). Night persistent areas in high latitudes or cloudy persistent areas (as in India in July) are classified as having no BRDF data. Antarctic and Arctic areas, as well as snow-covered areas in the winter are well classified (most of Europe and the USA experienced heavy snowfalls this year). Areas often classified with a medium quality index, as in the northern part of South America, in Central Africa or in Asia, are explained by the difficulty to retrieve BRDF model parameters in the presence of clouds. When removing pixels with water and no data, the coverage percentages are 29.2% and 74.3% with a good quality index for January and July 2010, 9.2% and 14% with a medium quality index, 5.3% and 6.3% with a filled quality index, 56.3% and 5.2% with snow pixels and 0.3% and 0.2% with a bad quality index, respectively.

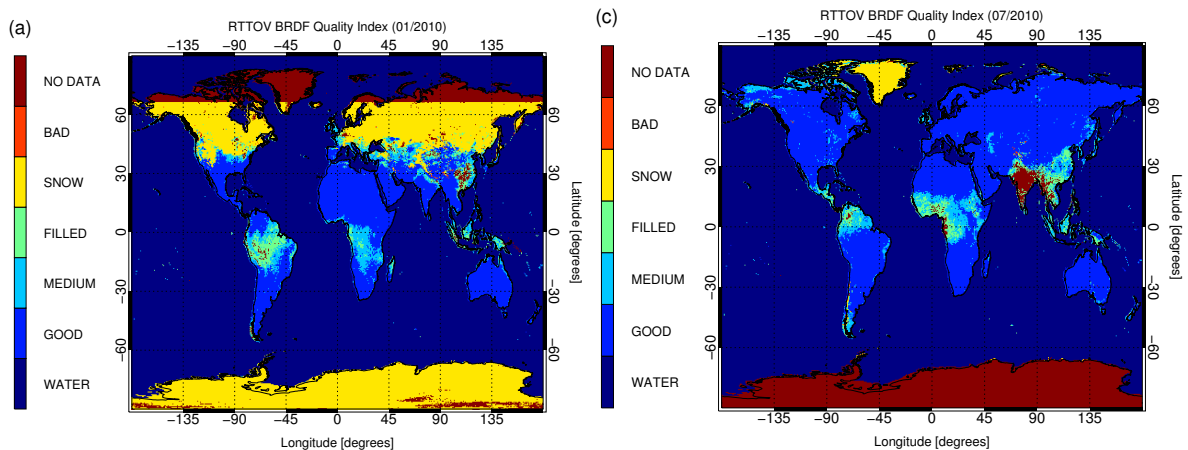


Figure 24: RTTOV BRDF quality index for 2010: January (left) and July (right)

2.2.1 Validation of the VIS/NIR land surface reflectance

For the validation of the RTTOV BRDF atlas, we simulated land surface BRDF using SEVIRI VIS/NIR channels and compared them with land surface albedo products (Geiger *et al.*, 2008) from the EUMETSAT Land-SAF. We were not able to validate the BRDF itself since the BRDF is not an operational product from the Land SAF team. We used the Land SAF directional hemispherical

reflectance (DHR) or black-sky albedo (BSA) products for both narrowband and broadband averaged at 0.1° spatial resolution from the original spatial resolution of SEVIRI. The Land SAF surface albedo product has been validated with ground measurements and MODIS collection 4 products (Carrer *et al.*, 2010). Here, we compared one daily Land SAF narrowband BSA product (called MDAL) that is provided in three SEVIRI channels ($0.6 \mu\text{m}$, $0.8 \mu\text{m}$ and $1.6 \mu\text{m}$) with simulated RTTOV narrowband BSA.

The RTTOV narrowband BSA α_{bs} were calculated from the MODIS BRDF kernel-driven product (Lucht *et al.*, 2000) by the following equation:

$$\alpha_{bs}(\theta_{ref}, \lambda) = f_{iso}(\lambda)(g_{0iso} + g_{1iso}\theta_{ref}^2 + g_{2iso}\theta_{ref}^3) + f_{vol}(\lambda)(g_{0vol} + g_{1vol}\theta_{ref}^2 + g_{2vol}\theta_{ref}^3) + f_{iso}(\lambda)(g_{0geo} + g_{1geo}\theta_{ref}^2 + g_{2geo}\theta_{ref}^3) \quad (2.2.2)$$

where the different coefficients g are given in Lucht *et al.* (2000) and θ_{ref} is the reference angle at local solar noon. Figure 25a depicts the SEVIRI channel 1 (at $0.6 \mu\text{m}$) Land SAF narrowband BSA product on 25th August 2011 averaged on a 0.1° grid. In Figure 25b the monthly mean RTTOV narrowband BSA for August 2011 in channel 1 is depicted.

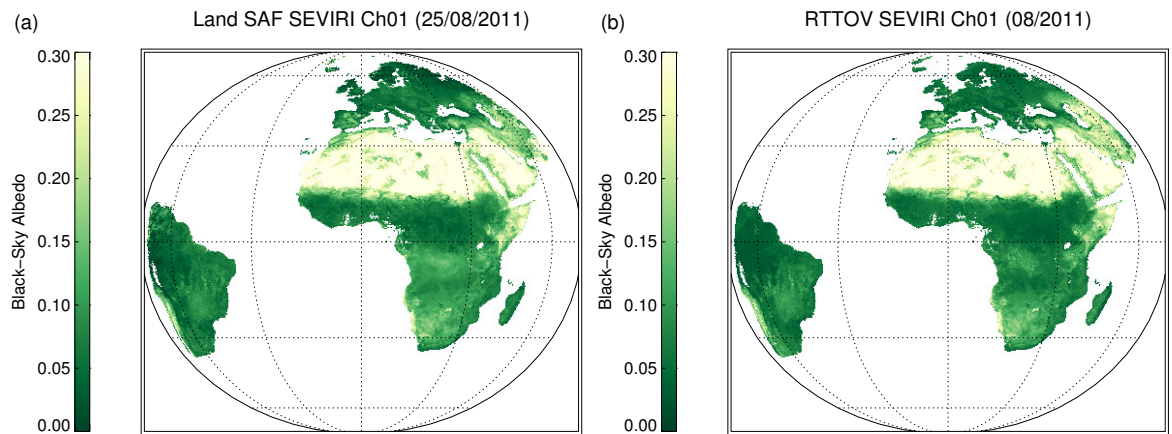


Figure 25: Land SAF narrowband BSA product on 25 August 2011 for SEVIRI channel 1 at $0.6 \mu\text{m}$ (a) and RTTOV narrowband BSA on August 2011 for SEVIRI channel 1 (b).

Overall, we found a good consistency in the RTTOV narrowband BSA as compared with the Land SAF product with higher biases between 0.01 and 0.03 in channel 2 (at $0.8 \mu\text{m}$). We found that the quality index of the RTTOV land VIS/NIR surface reflectance atlas was useful to understand areas where the comparison is less satisfactory (due to the presence of residuals clouds). It was also found that the correlation is better when the satellite zenith angle is lower than 65° . This threshold is needed to remove SEVIRI retrievals at the edge of the disk where the angular sampling is lower but also where the satellite BRDF retrievals are more difficult. More details and results about this validation are given in Vidot and Borbas (2013).

2.3 Updates to PC-RTTOV

A major update to PC_RTTOV is the introduction of the capability of performing radiance simulations in the presence of clouds. The method used for the simulation of the cloudy PC scores is

<p>The EUMETSAT Network of Satellite Application Facilities</p>		<p>RTTOV-11 Science and Validation Report</p>	<p>Doc ID : NWPSAF-MO-TV-032 Version : 1.1 Date : 16/8/13</p>
---	---	---	---

similar to that utilized for the simulation of the PC scores in clear skies (Matricardi 2010). The main difference resides in the fact that the training of the cloudy PC model has been carried out using cloudy spectra simulated using the scattering parameterisation featured in the standard RTTOV model. The dataset of atmospheric profiles used to train the cloudy PC model consists of profiles generated using the operational suite of the ECMWF forecast model. The dataset comprises 5760 vertical profiles of temperature, water vapour, ozone, cloud fraction, cloud liquid water and ice water content and ancillary information on surface properties. All the profiles have been obtained over the sea surface.

The cloudy PC_RTTOV model can accurately reproduce the cloudy spectra simulated by the conventional RTTOV model at a substantially reduced computational cost. In addition, the utilization of the PC based approach dramatically reduces the memory requirements associated with the use of the cloud overlapping scheme featured in RTTOV. It should be noted that the computation of the PC based cloudy radiances is subjected to a number of restrictions. Simulations can only be performed for IASI over sea surfaces; the concentration of CO₂, N₂O, CO and CH₄ trace gases cannot be varied (they are set to constant values specified in the PC score regression file) and continental-type water clouds cannot be introduced in the computations because the model has not been trained over land. It is also worth noting that surface emissivities cannot be specified by the user. They are in fact computed using the same dedicated model utilized for the training. In principle, the cloudy PC_RTTOV can also be used to simulate clear sky radiances because the training dataset includes clear sky spectra. It should be noted, however, that the training spectra are not based on line-by-line computations but on conventional RTTOV simulations.

As for the clear sky PC_RTTOV case, the user can select the number of predictors used in the cloudy PC score regression algorithm and the number of eigenvectors used in the reconstruction of the cloudy radiances. The rationale behind the choice of different combinations of eigenvectors/predictors is that the use of more eigenvectors/predictors results in more accurate, albeit less computationally efficient, simulations. PC score regression coefficients are available based on 300, 400, 500, and 600 predictors whereas the number of eigenvectors can be varied between 1 and 400. Whilst a typical choice can consist of 200 eigenvectors and 500 predictors, the user can vary these numbers to achieve speed vs. accuracy trade-offs that are optimal for specific applications. A detailed description of the cloudy PC_RTTOV model and an assessment of its accuracy can be found in Matricardi and McNally (2011).

Another update to PC_RTTOV is the introduction of a new format for the PC score regression coefficient file. The new coefficient file stores regression coefficients that can be used to directly simulate PC scores derived from different regions of the IASI spectrum. Three different regression sets are currently available. These can be used to simulate PC scores derived from the full IASI spectrum (the default PC_RTTOV choice), 165 long wave radiances and 297 short wave radiances respectively. Although the coefficient file also stores the eigenvectors to reconstruct the 165 and 297 radiances, we should stress that the main intent of the additional regression coefficients is to allow the user to experiment with the direct use of PC scores in an assimilation and/or retrieval system (e.g. see Matricardi and McNally 2013a). Details on the channels, the PC score regression algorithm and the choice of predictors can be found in Matricardi and McNally (2011) for the 297 channel case and in Matricardi and McNally (2013b) for the 165 channel case.

2.4 Addition of new aerosol scattering coefficients

2.4.1 Volcanic ash

The aerosol optical properties in the coefficients file are in the form of absorption and scattering cross-sections, backscatter coefficient and phase function at each infrared central wavelength. The absorption and scattering cross-sections are calculated by dividing the mass absorption or scattering coefficient (in m^{-1}) calculated using Mie theory by the number density (in m^{-3}). The backscatter coefficient is the integral of the backwards facing hemispheric values of the phase function.

The inputs to the Mie calculations, namely size distribution and refractive indices have been chosen after a literature search, considering recent observational data and a sensitivity study (Millington et al., 2012). The 2010 Eyjafjallajökull eruption in Iceland caused major disruption to aviation and its prolonged duration enabled a large amount of observational data to be collected. Refractive indices derived from a sample of Eyjafjallajökull ash (Dan Peters, University of Oxford, personal communication 2012) was compared to those published and was found to be similar to the widely used refractive indices of andesite in Pollack et al. (1973). Thus, andesite refractive indices (Pollack 1973) have been used in the generation of the RTTOV aerosol scattering coefficients.

The size distribution has a large impact on the magnitude of the absorption and scattering coefficients (Millington et al., 2012), and it can vary considerably between eruptions and particularly with distance from a volcano as the larger particles fall out faster than the smaller particles. The size distribution used in the generation of the RTTOV aerosol scattering coefficients is a log-normal distribution fitted to observations collected on the UK Facility for Airborne Atmospheric Measurements (FAAM) aircraft (Johnson et al., 2012). The FAAM flew 12 flights around the UK through ash clouds from the 2010 Eyjafjallajökull eruption. The log-normal distribution has a standard deviation (sigma) of 1.85 and a volume geometric mean diameter (D_g) of $3.8 \mu\text{m}$ (number geometric mean diameter of $12.20 \mu\text{m}$). This size distribution is taken to be representative of the airborne ash in a distal ash cloud (e.g. 1000 – 1500 km from volcano) for a similar type of eruption. The physical properties are shown in Figure 26.

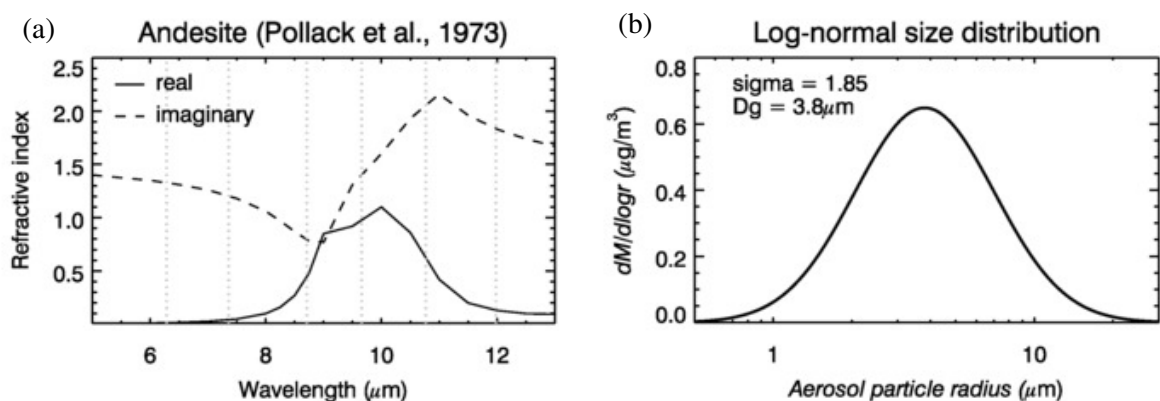


Figure 26: Physical properties of volcanic ash used in the generation of the RTTOV aerosol scattering coefficients. (a) Refractive indices of andesite (Pollack et al., 1973) plotted against wavelength, where the grey dotted lines mark the central wavelengths of SEVIRI infrared channels for reference. (b) Log-normal size distribution (Johnson et al., 2012) fitted to measurements of ash from Eyjafjallajökull in 2010.

2.4.2 Asian dust

The properties of the new Asian dust particle type are described in Han *et al* (2012) and are summarised here. The absorption and scattering coefficients and the phase functions are derived from Mie theory as for the other RTTOV particle types. The inputs to the calculations are the refractive index and the particle size distribution. The Asian dust refractive index comes from Volz (1972, 1973) as shown in Figure 27. The size distribution was obtained as a linear combination of the size distributions of the mineral nucleation, accumulation and coarse mode particle types (MINM, MIAM and MICM) from the OPAC database (already available in RTTOV) for radii between 0.01 and 60 μm . The weights were obtained by fitting to a particle size distribution derived from sky radiometer measurements made at Dunhuang, China (see Figure 28).

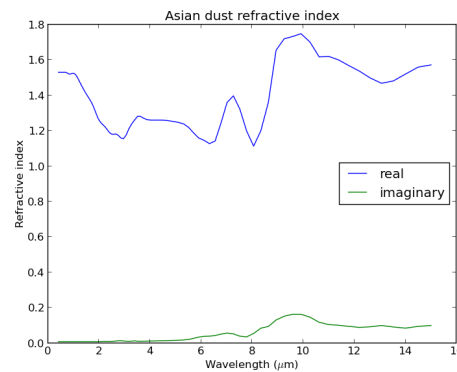


Figure 27: Refractive index for Asian dust type.

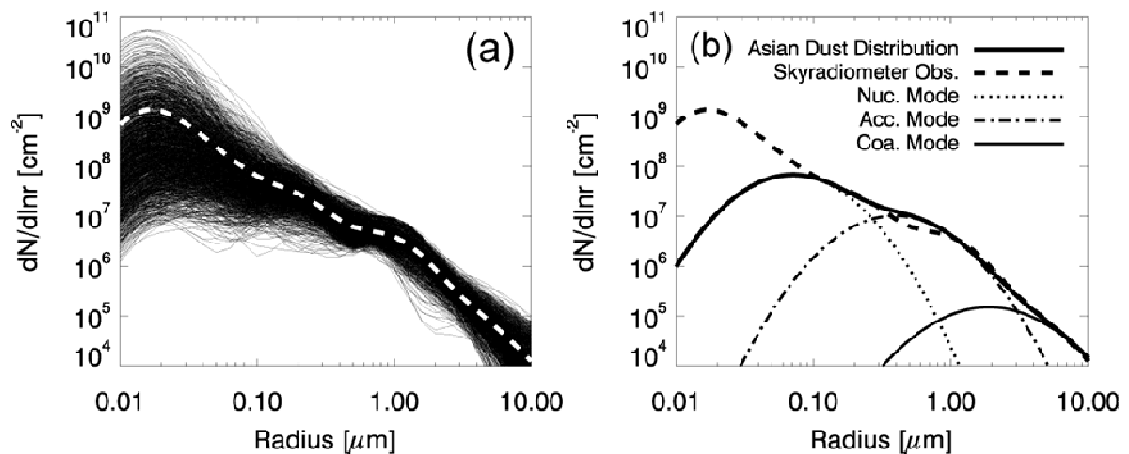


Figure 28: (a) Size distributions of Asian dust retrieved from sky radiometer measurements at Dunhuang, China (thin solid lines), and the mean size distribution (white dashed line). (b) Mean size distribution from the sky radiometer measurements (thick dashed line), three modes for mineral dust components from OPAC (nucleus mode: Nuc, accumulation mode: Acc, and coarse mode: Coa), and the best fit for the mean size distribution (thick solid line).

2.5 A New Parameterisation of Ice Cloud Optical Properties in Thermal Infrared

A new database of optical properties of ice cloud particles in the thermal infrared has been developed (Baran *et al.*, 2009; Baran *et al.*, 2011; Baran *et al.*, 2013) and parameterized for RTTOV. As compared with the ice cloud optical properties parameterization of previous RTTOV version (R10REP2010), this new database offers two new features: (1) It allows a direct parameterization of the optical properties from the RTTOV inputs for ice cloud (the cloud temperature T_C and the ice water content IWC) without the need of estimating the effective size of

ice cloud particle through four different empirical parameterizations, and (2) the optical properties of the Baran database were simulated for an ensemble of different ice cloud particle shapes which is expected to be more realistic than the two current RTTOV ice particles shapes (hexagonal or aggregates).

The Baran database is based on 20662 PSDs (Particles Size Distribution) that were assembled from different cloud temperatures (T_C) and ice water contents (IWC). The overall database covers a range of cloud temperature between 185 and 270 K and a range of IWC between approximately 10^{-5} and 1 g.cm^{-3} (see Figure 29-left).

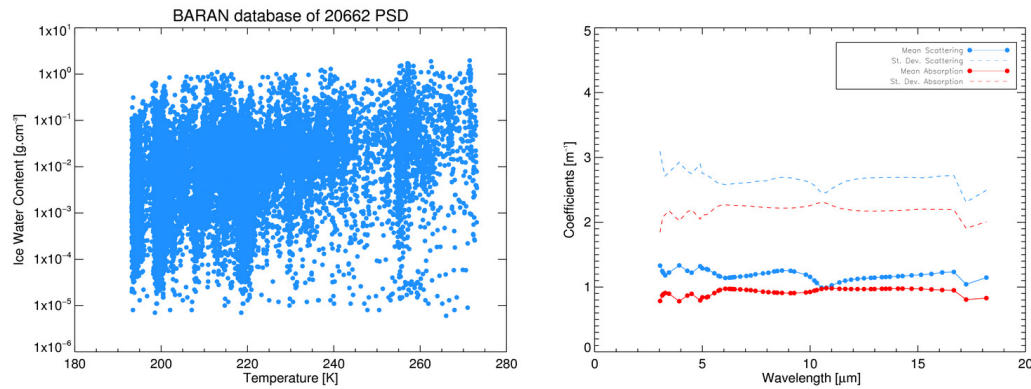


Figure 29. Left: Cloud Temperature and IWC distribution of the Baran database. Right: Mean and standard deviation of the scattering coefficients (in blue) and absorption (in red).

The database provides for each PSD, simulated volumetric extinction coefficient β_e (in m^{-1}), volumetric scattering coefficient β_s (in m^{-1}), single scattering albedo ω_0 and asymmetry parameter g at 57 wavelengths between 3 and 18 μm . Figure 29-right shows the mean absorption coefficient and the standard deviation of the absorption coefficient versus the wavelength (in red) and of the scattering coefficient (in blue) calculated as extinction minus absorption. Additionally, each associated phase function $P(\theta)$ (i.e., 20662 times 57) was simulated through an analytical formulation from the asymmetry parameter g .

In the thermal infrared, the Chou scattering scheme of RTTOV uses four parameters: absorption coefficient β_a , scattering coefficient β_s , the parameter b and the phase function P . The first three optical parameters are used for the calculation of the effective extinction employed in the radiative transfer equation to take into account the diffuse radiation (similar to Equation 20 of R9REP2008). The parameter b represents the fraction of backscattered radiation and is calculated from the phase function P (Equation 21 of R9REP2008). Here, we speed up the calculation of $\overline{P(\mu, \mu')}$, that theoretically requires three loops (two over solar and satellite zenith angles and one over azimuth difference angle), by tabulating the cosine of zenith angles between 0 and 1 with a large number of bins and linearly interpolated in the table. This method reaches an accuracy of 0.01° compared to an analytical calculation. We parameterize the RTTOV ice cloud optical properties through the relationship proposed by Baran et. al. (2013) i.e.:

$$\log_{10}[\beta(\lambda)] = A + BT_c + C \log_{10}(IWC) + DT_c^2 + E(\log_{10}(IWC))^2 + FT_c \log_{10}(IWC) \quad (2.5.1)$$

$$b(\lambda) \text{ or } g(\lambda) = A + BT_c + C \log_{10}(IWC) \quad (2.5.2)$$

where the coefficients A, B, C, (and D, E and F for β) depend on the wavelength λ and are different for each optical parameter. The coefficients were calculated by using a non-linear least squares

fitting procedure. On the panel of Figure 30 is represented the results at 8.7 μm . Figs. 30a to 30d show the estimated versus true b , g , absorption and scattering coefficients, respectively.

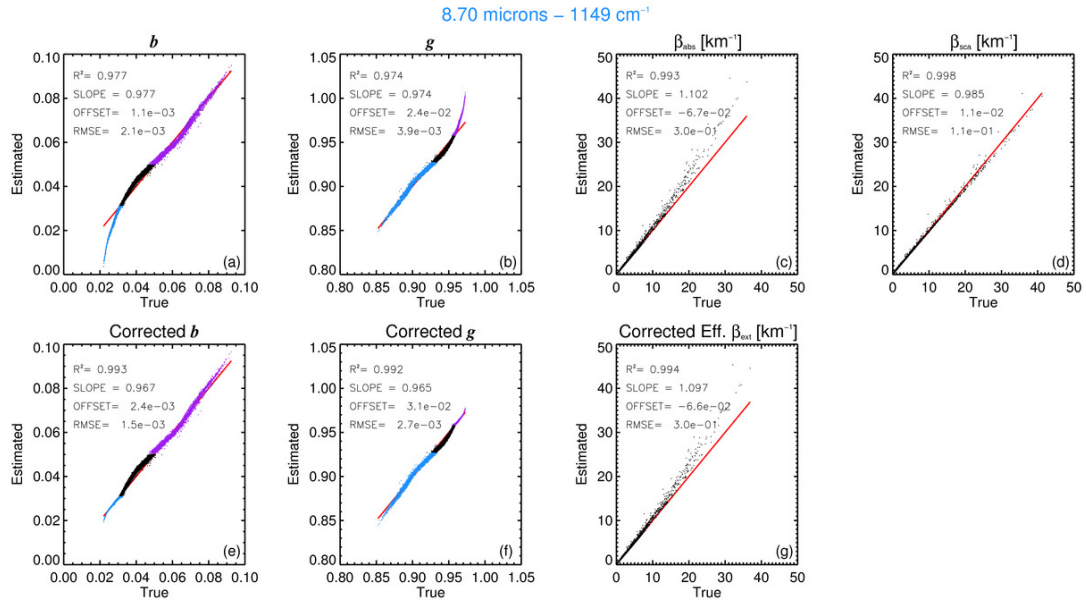


Figure 30. Estimated optical parameters versus true optical parameters at 8.7 μm for b (a), g (b), absorption coefficient (c) and scattering coefficient (d). Same results when the correction is applied on b (e) and g (f). Effective extinction (g) after application of correction on b .

Absorption and scattering are well retrieved by the parameterization but not that well for lower or higher b and g . To improve the estimation of b and g , we applied a correction by visually selecting 2 thresholds for b ($t_{b,1}(\lambda)$ and $t_{b,2}(\lambda)$) and for g ($t_{g,1}(\lambda)$ and $t_{g,2}(\lambda)$) to split the values into three parts (represented by different colours in Figs. 30a and 30b). For values above and below each threshold, we calculated a linear regression on these values and corrected the estimated values as for example for b :

$$b_{\text{cor}}(\lambda) = \frac{b(\lambda) - x_{b,0}(\lambda)}{x_{b,1}(\lambda)} \quad (2.5.3)$$

where $x_{b,0}(\lambda)$ and $x_{b,1}(\lambda)$ are the offset and the slope of the linear regression at a particular wavelength. Results of the correlation after applying the correction is shown in Figs. 30e and 30f for b and g , respectively. In both cases correlation coefficients are increased to better than 0.99. Because, we are interested in the calculation of the effective extinction, we show on Figure 30g the good correlation between the true effective extinction and the parameterized effective extinction with corrected b . The same methods were applied to each wavelength.

2.5.1 Validation of New Parameterisation of Ice Cloud Optical Properties in Thermal Infrared

The validation of the new parameterisation of ice cloud optical properties in the thermal infrared was conducted with an operational 2C-ICE product (Deng *et al.*, 2010) that contains IWC and effective size of ice crystal profiles retrieved from combined Radar/Lidar measurements from the Cloudsat and Calipso (onboard Calipso) on the A-Train constellation. We compared simulated brightness temperature (BT) and observations at 8.7 μm from the IIR instrument (onboard Calipso). We used the operational ECMWF-AUX product that contains collocated pressure, temperature,

specific humidity, ozone profiles as well as surface pressure and skin temperature. We selected all ice cloud occurrences during the period between 25-31 August 2010.

In this validation exercise, we compared the new parameterization of ice cloud with the other parameterizations of ice cloud from RTTOV-10. The other parameterizations were developed from 4 different relationships between IWC and effective diameter of the ice crystals (namely, OL95, W98, B02 and MF03, see section 2.9.5 of the R9REP2008) and for two different shapes of ice crystal, i.e. hexagonal (HEX) or aggregates (AGG). For RTTOV-10, it is also possible to input the effective diameter (Deff) profile of the ice clouds. Finally, there are 11 different options to simulate ice clouds. In the panels of Figure 31 are displayed the simulated brightness temperature for all different RTTOV ice cloud parameterization options versus observed brightness temperature from the IIR at 8.7 μm . We can see that the new parameterization of ice cloud is better correlated for three out of four previous parameterizations, but with a larger bias and RMSE. The main advantages are a simpler scheme and the fact that you get consistent optical properties across all wavelengths.

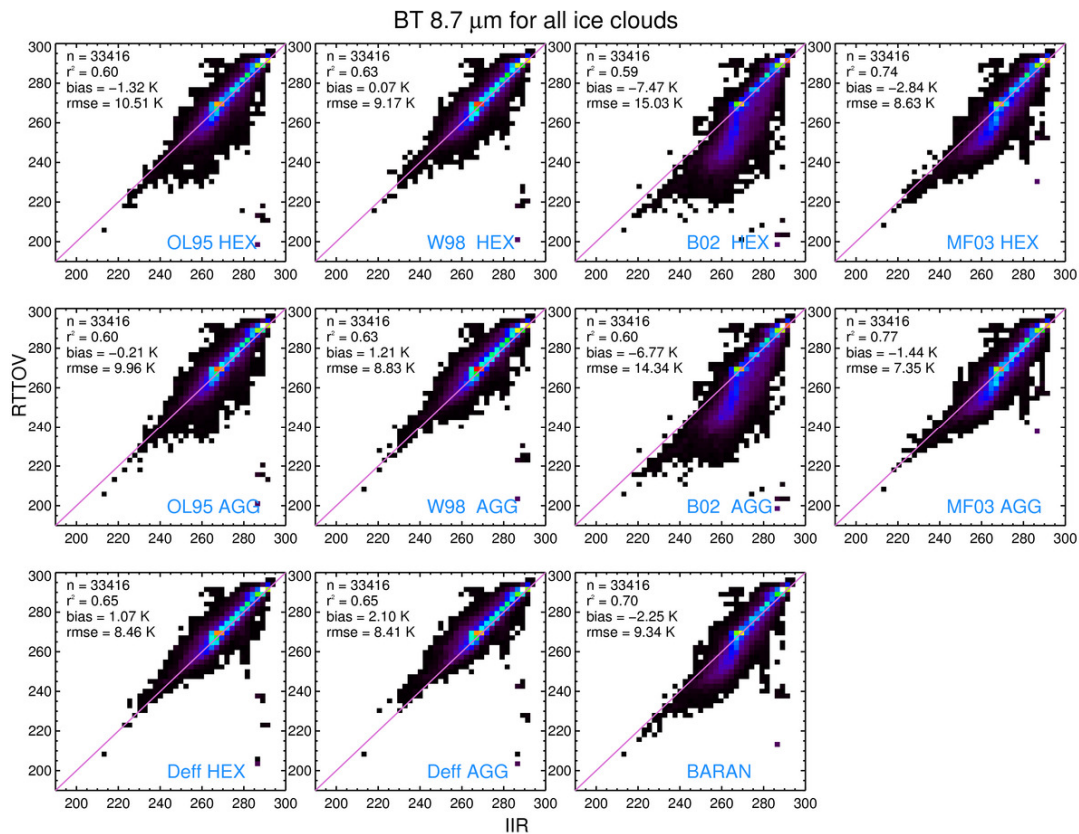


Figure 31. RTTOV versus IIR BT at 8.7 μm for all ice cloud RTTOV options. The upper 2 rows are for the ice cloud simulation in RTTOV-9 and 10 for both hexagons and aggregate crystals and the lower row is the new parameterisation from Baran et al (2011).

2.6 Non-LTE for IR sounders

2.6.1 Introduction

High-resolution shortwave infra-red sounder channels around the CO₂ v3 band (at 4.3 μm) are very clean sounding channels that only depend strongly upon CO₂ emission and peak between 10 – 100 hPa. However, at high altitude, solar pumping can overpopulate higher ro-vibrational energy levels. If collisions are no longer sufficiently able to thermally redistribute energy, this overpopulation can cascade down to lower levels so that one or more states may significantly violate the fundamental assumption of LTE (namely, that level populations are populated according to a Boltzmann distribution) and consequently a Planck function is no longer an appropriate source function.

Significant non-Local Thermodynamic Equilibrium (non-LTE) emission in CO₂ is observed primarily in the daytime in the atmosphere above 40 km (figure 32). As a result there is a significant deviation in observed radiances whereby non-LTE emission can add up to 10 Kelvin to the measured brightness temperature over that predicted by radiative transfer models which, by default, assume LTE throughout the atmosphere (figure 32). Consequently, temperature retrievals in this affected region are not possible with such large biases. Reducing this bias may allow assimilation systems and retrieval algorithms to use SWIR CO₂ channels for higher resolution stratospheric sounding than currently available with MW instruments.

Slow but accurate line-by-line (LBL) models such as LBLRTM (Clough et al., 2005) and GENLN2 (Edwards, 1992) have incorporated non-LTE effects by scaling the molecular absorption coefficients and Planck function according to the discrepancy between the local kinetic temperature and the CO₂ vibrational temperature profiles (calculated externally) (Lopez-Puertas and Taylor, 2001). This has been possible for some time but only more recently has the effect been parameterised for use in fast codes (DeSouza-Machado et al., 2007; Chen et al., 2013).

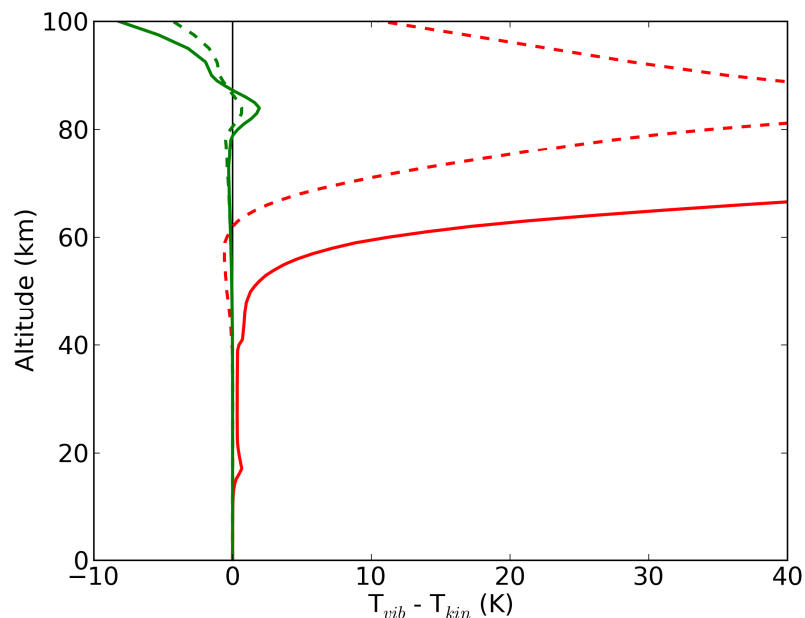


Figure 32: Difference in vibrational temperature versus kinetic temperature at 2349.1433 cm⁻¹ (SW, red) compared with 667.3801 cm⁻¹ (LW, green). Daytime profiles are shown as solid lines, nighttime profiles are dashed. Non-LTE emission is most evident in the shortwave profile and is much more prominent during the day.

<p>The EUMETSAT Network of Satellite Application Facilities</p>		<p>RTTOV-11 Science and Validation Report</p>	<p>Doc ID : NWPSAF-MO-TV-032 Version : 1.1 Date : 16/8/13</p>
---	---	---	---

The non-LTE radiance correction scheme used in RTTOV broadly follows that of CRTM described in Chen et al. (2013), i.e. a 2+2 predictor scheme that adds a ‘correction’ term to the LTE radiance as calculated by the fast radiative transfer model.

2.6.2 Calculating Non-LTE radiances

In order to account for non-LTE effects it is necessary to modify the source function, the absorption coefficient and the partition function to reflect the fact that the vibrational states for a particular molecule are no longer populated according to the Boltzmann distribution. This is done using a single characteristic vibrational temperature, T_{vib} , defined for each simulated species (specifically here for each isotopologue of CO₂), all calculated vibrational states and in each atmospheric layer, defined as,

$$T_{vib,i} = \frac{-hE_{vib}}{k \ln\left(\frac{n_i}{n_0}\right)}, \quad (2.6.1)$$

where n_i is the fractional level population of the i^{th} vibrational state, h is the Planck constant, and k is the Boltzmann constant.

For this work (and that of DeSouza-Machado et al., 2007 and Chen et al., 2013), the GRANADA code (Funke et al., 2012) was used to generate vibrational temperature profiles for 57 vibrational transitions across 4 isotopologues; CO₂, ¹³CO₂, C¹⁸O₂ and C¹⁷O₂, for every altitude of each (48) atmospheric profile extrapolated to 120 km. Up to this height at least, CO₂ rotational lines are assumed to be in LTE. In order to determine the population of each vibrational state, GRANADA iteratively solves the equations of statistical equilibrium (by considering collisional, chemical and radiative processes) until a self-consistent solution for the entire atmospheric profile is converged upon.

The calculated vibrational temperatures are subsequently used by LBLRTM to scale the Planck function and LTE absorption coefficients calculated using the LTE assumption. The method for performing non-LTE calculations broadly follows that set out in its predecessor code FASCOD2 (Ridgway et al. 1982), chiefly:

First, identify upper and lower state vibrational states of each spectral line which are non-thermally populated and compute the population enhancement ratio (departure coefficient), r_i , for each vibrational state,

$$r_i = \frac{n_i^{NLTE}}{n_i^{LTE}}. \quad (2.6.2)$$

For any given state, i , this can be re-expressed as,

$$r_i = \frac{\exp(-E_{vib}/kT_{vib}) / \sum_j g_j \exp(-E_{vib}/kT_{vib})}{\exp(-E_{vib}/kT_{kin}) / \sum_j g_j \exp(-E_{vib}/kT_{kin})} \quad (2.6.3)$$

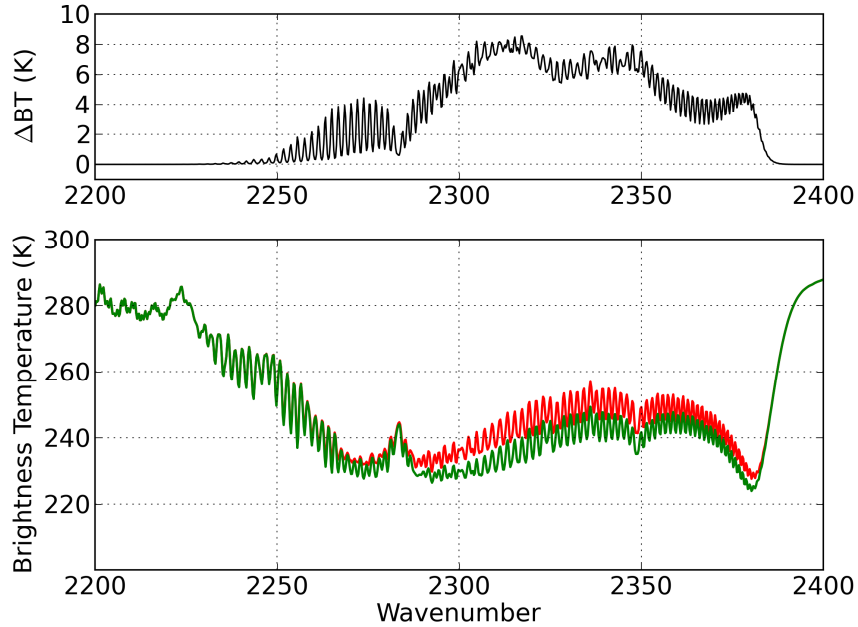


Figure 33: Bottom panel; Simulated non-LTE BTs (red) against LTE BTs (green) for IASI for profile 1 of the UMBC profile set. Top panel; non-LTE BT – LTE BT, the differences are greatest from around 2250 – 2386 cm^{-1} .

Here, the requirement for externally calculated vibration temperatures becomes apparent, as does the necessity for the user to input the statistical degeneracy, g , of each vibrational state that is to be included in the RT calculation.

Next, the absorption coefficient for a particular transition, α_{ul} , is modified accordingly,

$$\alpha_{ul}^{NLTE} = \frac{r_l - r_u \Gamma_{ul}}{1 - \Gamma_{ul}} \alpha_{ul}^{LTE}, \quad (2.6.4)$$

where Γ_{ul} is the classical Boltzmann factor for the transition, $u \rightarrow l$. Similarly, the source term can be modified so that in the NLTE case,

$$J_{ul}^{NLTE} = B_{ul} \frac{n_u^{NLTE}}{n_u^{LTE}} \frac{\alpha_{ul}^{LTE}}{\alpha_{ul}^{NLTE}}. \quad (2.6.5)$$

A more detailed treatment can be found in the KOPRA handbook (<http://www.imk-asf.kit.edu/english/312.php>) and technical details of the FASCOD2 implementation can be found in Ridgway et al. (1982). Using these modified terms, the radiative transfer calculation then proceeds in the normal fashion.

2.6.3 Obtaining a radiance correction

LBLRTM v12.2 was used to compute non-LTE radiances for a diverse profile set comprised of 48 profiles supplied by UMBC (Strow et al., 2003). This version of LBLRTM fixes a previous bug present in versions up to v11.7 where only the vibrational temperature profile of the $^{12}\text{C}^{16}\text{O}_2$

		RTTOV-11 Science and Validation Report	Doc ID : NWPSAF-MO-TV-032 Version : 1.1 Date : 16/8/13
---	---	---	--

isotopologue was used for a particular transition regardless of whether a different profile was provided. It has been suggested that this may cause an error of around 0.2 K (Chen et al., 2013).

Radiances were calculated for 13 sensor zenith angles and 6 solar zenith angles to generate a total of 3744 spectra to be used as regression data for the parameterisation.

In order to take account of non-LTE effects in RTTOV, an additive correction, ΔR_{ch} , is applied to the LTE radiance,

$$R_{ch}^{NLTE} = R_{ch}^{LTE} + \Delta R_{ch}, \quad (2.6.6)$$

where R_{ch} is the channel radiance as calculated by LBLRTM (with or without NLTE).

Channel radiances are obtained by convolving raw LBLRTM radiances (obtained at a resolution of 0.001 wavenumbers) with the spectral response function (SRF) of each instrument, upsampled to the same resolution as the LBLRTM radiance using cubic splines.

The coefficients for the correction scheme are only calculated at discrete points corresponding to the input sensor zenith angles, θ , and solar zenith angles, ϕ . The sensor zenith angle is defined up to $\sec(\theta) = 3.5$ (equivalent to $\theta = 73.4$ degrees). To reduce interpolation error, greater resolution is given to angles closer to nadir – fully, the 13 secants of the sensor zenith angles are 1.000, 1.125, 1.250, 1.375, 1.500, 1.750, 2.000, 2.250, 2.500, 2.750, 3.000, 3.500. The coefficients are calculated for the six solar zenith angles for which vibrational temperatures were originally calculated: 0, 40, 60, 80, 85, 90 degrees.

For each (θ_i, ϕ_j) couplet, ΔR is estimated using two temperature predictors such that

$$\Delta R(\theta_i, \phi_j) = c_0(\theta_i, \phi_j) + c_1(\theta_i, \phi_j)T_1 + c_2(\theta_i, \phi_j)T_2 \quad (2.6.7)$$

where c_{0-2} are coefficients derived from statistical regression (using a Levenberg-Marquardt minimisation technique to minimise mean-square-error) of the fit function against the training data (channel radiances) and T_1 and T_2 are the mean kinetic temperatures between 0.005 and 0.2 hPa (~60 - 85km) and 0.2 - 52 hPa (~20 - 60 km) respectively. These pressure layers roughly correspond to the mesospheric and stratospheric layers where the deviation of the kinetic temperature from the vibrational temperature for many transitions can become significant (see figure 33).

The final correction applied to the LTE channel radiance is computed using a bilinear interpolation operator to determine the weights, k_1 and k_2 , given to the four (bounding) nearest neighbours in $(\sec(\theta_i), \sec(\phi_j))$ space:

$$\begin{aligned} \Delta R_{ch} = & k_1 k_2 \Delta R(\theta_i, \phi_j) + \\ & (1 - k_1) k_2 \Delta R(\theta_{i\pm 1}, \phi_j) + \\ & k_1 (1 - k_2) \Delta R(\theta_i, \phi_{j\pm 1}) + \\ & (1 - k_1)(1 - k_2) \Delta R(\theta_{i\pm 1}, \phi_{j\pm 1}) \end{aligned} \quad (2.6.8)$$

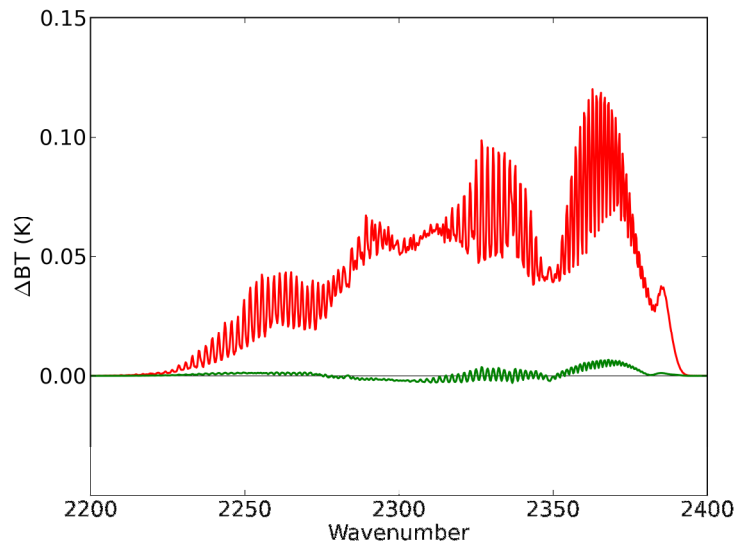


Figure 34: Root-mean-square fitting error over all profiles (for the IASI instrument) is shown in red. There is very little (< 0.01 K) bias (green) in the statistical regression. AIRS and CrIS fitting errors sit entirely inside the envelope of IASI values and thus are not shown here.

Figure 34 shows that the RMS fitting error (for IASI) over all profiles is on the order of 0.1 K which is very small compared to the gross bias (at 10 K). There is very little (< 0.01 K) bias across the channels in the statistical regression. Validation against independent observations has not yet been undertaken but will be available in a separate report.

2.7 Lambertian surface reflectance

There are concerns the default specular reflection assumption within RTTOV over land and sea-ice is a poor approximation particularly at microwave frequencies. Guedj *et. al.* (2010), Harlow (2009) and Harlow (2011) have all shown that the reflection over dry snow and multi-year sea-ice is better characterised by assuming a Lambertian approximation. True Lambertian reflection requires an integral over a range of angles to cover the hemisphere which would prove difficult (and costly) in the RTTOV framework. Fortunately Matzler (2005) has developed an approximation as a function of optical depth as shown in Figure 35.

So we can model the Lambertian scattering as a downwelling ray at $\sim 55^\circ \pm 3^\circ$ for lower optical depths. The effect of assuming specular reflection for a conical scanner (e.g. SSM/I) which views at ~ 53 degrees will be small (~ 0.2 K for a near surface sounding channel).

RTTOV to date has assumed specular reflection and models the downwelling component $B(\theta)$ that is reflected up into the radiometer in the following way:

$$B(\theta) = \tau_{surf}(\theta)(1 - e) \int_{surface}^{toa} B d\tau(\theta) \quad (2.7.1)$$

Where τ_{surf} represents the transmittance from surface to space at a viewing angle θ and the integral goes from the toa to the surface.

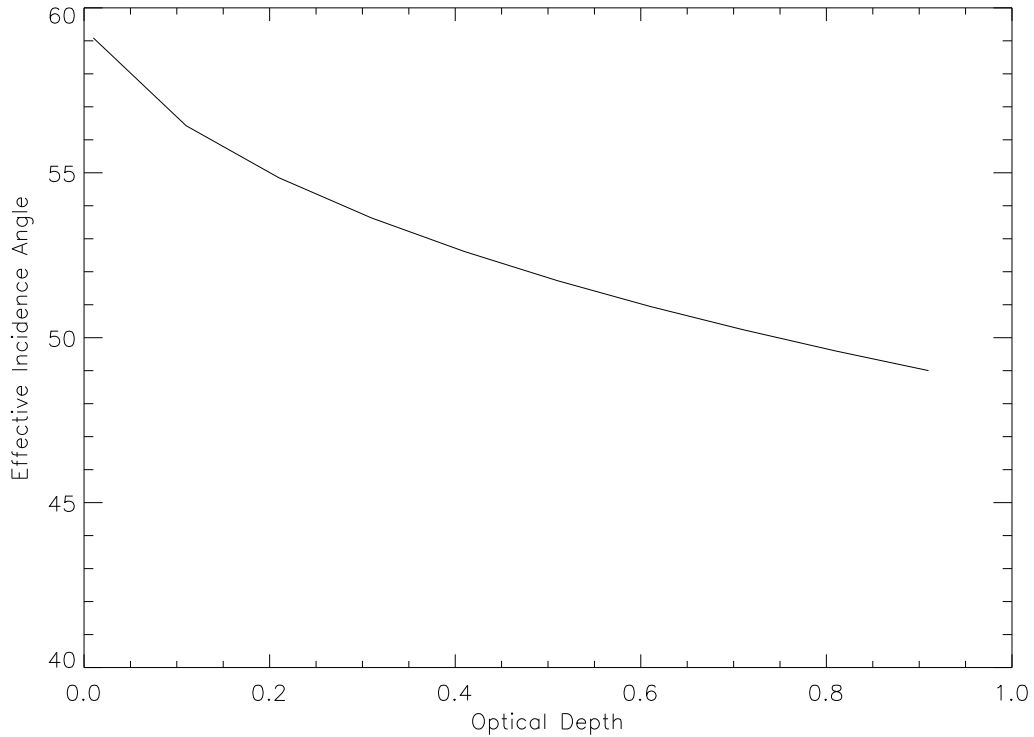


Figure 35. Effective incidence angle for Lambertian reflection as a function of optical depth

RTTOV precomputes the transmittance profiles for a desired zenith angle θ and for a uniform layer evaluates (2.7.1) in the following way:

$$B(\theta) = \tau_{surf}^2(\theta) \cdot (1 - e) \sum 0.5 * (B_i + B_{i+1}) \left\{ \frac{\tau_i(\theta) - \tau_{i+1}(\theta)}{\tau_i(\theta) \cdot \tau_{i+1}(\theta)} \right\} \quad (2.7.2)$$

where $\tau_i(\theta)$ is the transmittance from level i to space at viewing angle θ . This was the formulation in RTTOV-8 and earlier versions but since RTTOV-9 a “linear in tau option” was introduced to take into account the optical depth of the layer when calculating the source function (Matricardi, 2005; R9REP2008) where the optical depth of the layer is also included in the calculation of the source function. However this is only appropriate for upwelling radiances and so was not included in the downwelling radiation component considered here. For Lambertian reflection the downwelling ray is actually modelled as an effective angle θ_{eff} irrespective of the viewing angle θ_{view} .

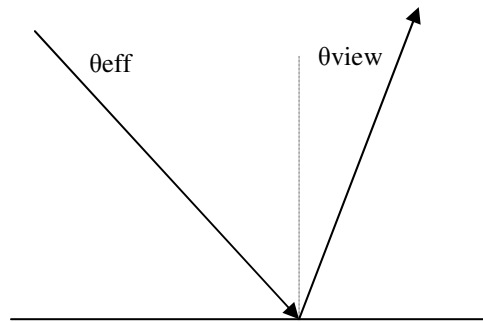


Figure 36. Definition of view angles

To model this the transmittance profile needs to be scaled to represent the transmittance profile for a viewing angle at θ_{eff} . The downwelling calculation now becomes

$$B(\theta) = \tau_{surf}(\theta) \cdot \tau_{surf}^p \cdot (1 - e) \sum 0.5 * (B_i + B_{i+1}) \left\{ \frac{\tau_i^p - \tau_{i+1}^p}{\tau_i^p \cdot \tau_{i+1}^p} \right\} \quad (2.7.3)$$

Where p is $\cos(\theta) \sec(\theta_{eff})$ i.e. for a nadir observation $p = 1.74$ when θ_{eff} is 55° . We can see from eq. 2.7.3 that any error in the downwelling calculation will be worse at lower emissivity – typically over ice and snow features.

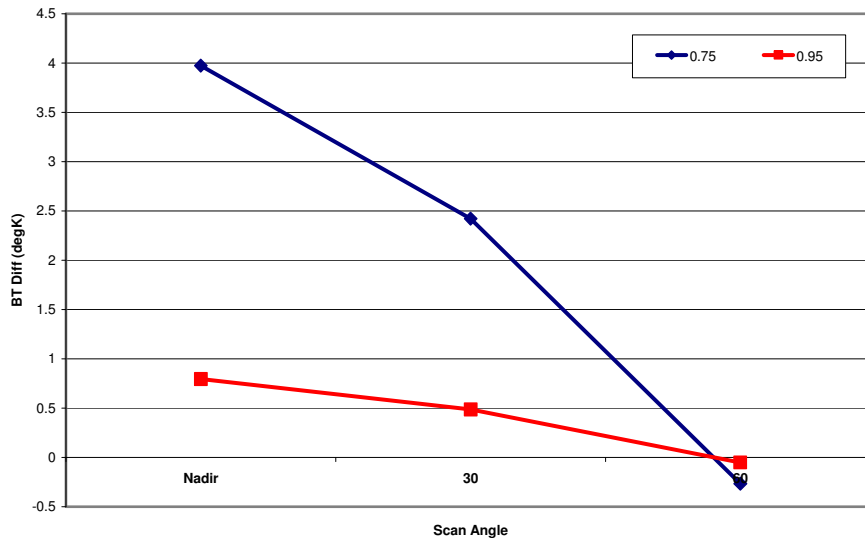


Figure 37. Lambertian - specular BT difference for ASMU-A channel 4 for a surface emissivity of 0.75 (blue) and 0.95 (red).

Assuming Lambertian reflectance the differences in TOA brightness temperatures from specular reflection are shown in Figure 37 for AMSU-A channel 4 for a range of scan angles. The biggest differences are for nadir views where they can be in excess of +4K for an emissivity of 0.75. Figures 38a and 38b show the difference between Lambertian and specular reflection for all the AMSU-A channels for emissivities typical of dry snow (0.75) and land (0.95). AMSU-A channel 3 is most affected with nadir differences up to 7K but channels 4, 5 and 15 also have differences of over 1K at nadir. Note the AMSU-B/MHS window channels (16, 17 and 20) are also affected by this revised surface reflection but are not shown here.

RTTOV-11 has been modified to allow the computation of the Lambertian reflected downwelling radiance if the appropriate logical switch is set in the call to RTTOV. Users will need to link this with the underlying surface type.

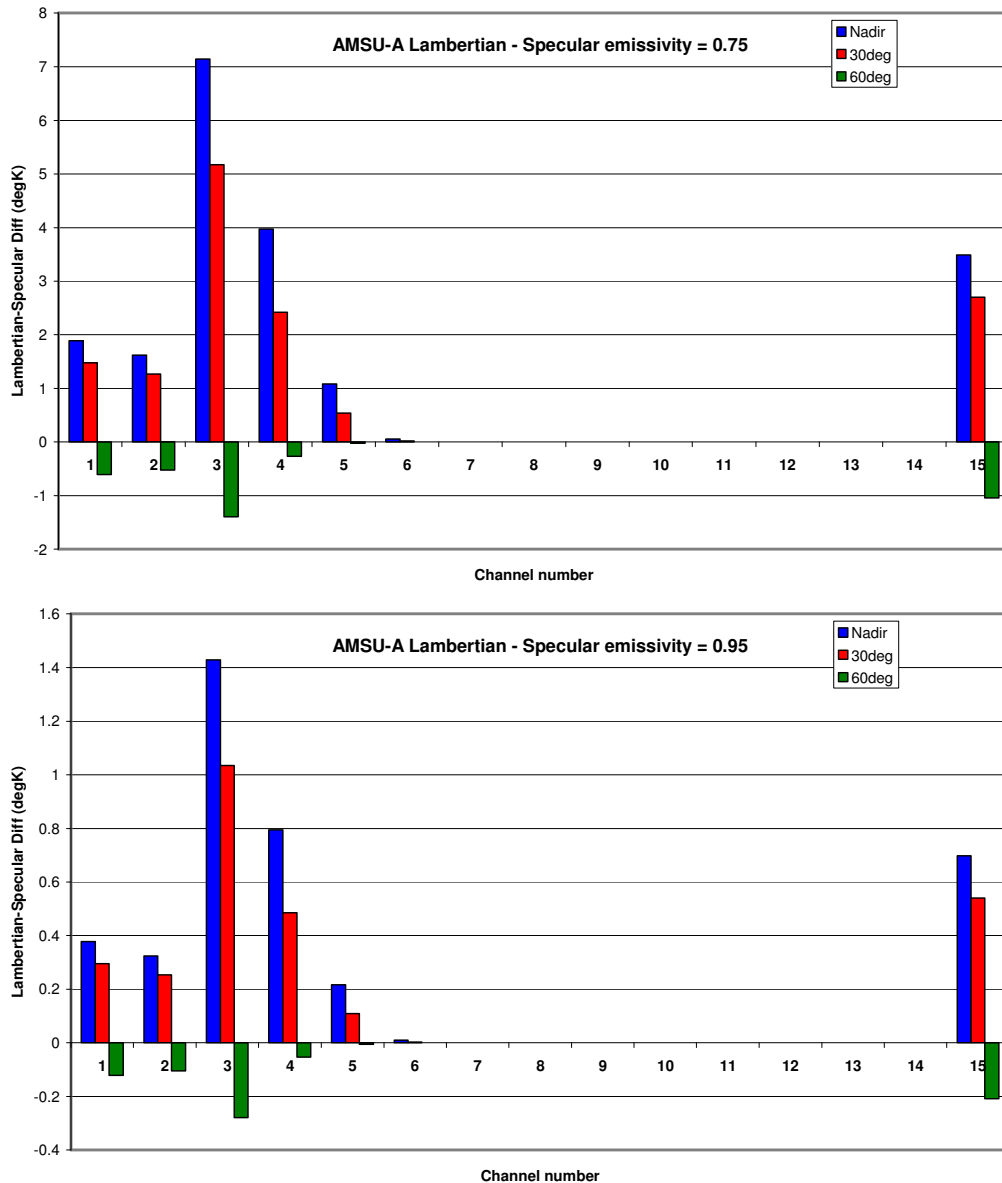


Figure 38. Lambertian-specular BT difference for all AMSU-A channels and 3 viewing angles. The top plot is for a surface emissivity of 0.75 and the bottom plot of 0.95. Note the different scale.

2.8 Improved SSU simulations

The Stratospheric Sounding Unit (SSU) has provided stratospheric soundings over a twenty-five year period and data is being reanalysed for climate studies.

SSU has three channels in the 15 μm CO_2 band. It is a pressure modulated radiometer (PMR) with a CO_2 gas cell on the optical path to each channel detector and a wide blocker filter, common to all channels, to restrict the spectral range of the radiation reaching the detector itself. The pressure in each cell is cyclically varied with a piston in an adiabatic manner, and the mean cell pressure, shown in Table 3, may be determined at any time from the frequency of the piston cycle.

SSU Channel	Mean Cell Pressure	Peak Weighting Function
1	100 hPa	15 hPa
2	35 hPa	5 hPa
3	10 hPa	1.5 hPa

Table 3. Relationship between nominal cell pressures for the SSU channels, and the associated peak in the weighting function

2.8.1 Updated coefficients for SSU

RTTOV-10 was released with a set of SSU coefficient files calculated by Kobayashi et al. (2009) for TIROS-N, NOAA-5, 6, 7, 9, 11, 14. TIROS-N has the numerical designation NOAA-5 within RTTOV, and, since NOAA-11 had two separate periods of operation, its coefficients were calculated for two different sets of cell pressures. For RTTOV-11 these coefficients have been updated.

The effect of the CO₂ cell, taking account of all lines passed by the wide filter $G(\nu)$, is defined by the gas correlation response functions $H_1(\nu)$, $H_2(\nu)$, $H_3(\nu)$ for the three channels. For each channel it is only the cyclical signal that will be detected, and the ‘two-cell’ approximation used in Brindley et al. (1999) was adopted, in which $H_j(\nu)$ is the difference between the transmittance across the cell for minimum cycle pressure and that for maximum cycle pressure:

$$H_j(\nu) = \tau_j^{\text{Pmin}}(\nu) - \tau_j^{\text{Pmax}}(\nu). \quad (2.8.1)$$

If the simulated transmittance from any given level to space at frequency ν in channel j is $\tau_j^{\text{atm}}(\nu)$, then the corresponding transmittance τ_j averaged over channel j will be given by

$$\tau_j = N^{-1} \int \tau_j^{\text{atm}}(\nu) \times (G(\nu) \times H_j(\nu)) d\nu, \quad (2.8.2)$$

where the normalisation is given by

$$N = \int G(\nu) \times H_j(\nu) d\nu. \quad (2.8.3)$$

The procedure used for generating RTTOV coefficients was essentially the same as for any other instrument. Using the line-by-line radiative transfer model LBLRTMv12.0, level-to-space monochromatic transmittances $\tau_j(\nu)$ for each of four gas combinations (well-mixed gases, and variable water vapour, carbon dioxide and ozone) were calculated over the channel passbands for a diverse set of atmospheric profiles. However, the range of CO₂ abundances in the profiles was first expanded to cover the lower values present during the operational lifetime of SSU, as evidenced by historical data from the Mauna Kea Observatory. In contrast to the case for a filter radiometer like HIRS, the channel averaging in (2.8.2) was performed at high resolution to preserve the detailed spectral variation within $H_j(\nu)$, and secant exponents between 1.0 and 2.25 were applied to the input transmittances $\tau_j(\nu)$ to provide six viewing angles. The SSU maximum scan angle of 40° from nadir, is about 10° smaller than HIRS on the same platform, so the secant range is here more than necessary. Finally, in the usual way, the resulting channel-averaged transmittances τ_j were regressed onto RTTOV predictors calculated from the profile variables to generate the coefficients. Predictors from the RTTOV-8 scheme were used, as this scheme is suitable for wide channel radiometers and is able to include all the variable gases for SSU.

The new coefficients used a later version of LBLRTM than Kobayashi et al., (2009) and an updated line database. They also included ozone as an additional variable gas, and were based on a more recently derived training set of profiles with more stratospheric levels. However, they used the same cell pressures, these being single values chosen for each SSU platform to best represent the historical pressure curves. In a comparison of top-of-atmosphere brightness temperatures for TIROS-N using the ‘new’ and ‘old’ coefficients, the differences, shown in Table 4, were small and mostly less than a tenth of a Kelvin. The three profiles used for this test, taken from the training set used to generate the coefficients, were the minimum envelope profile (zenith angle 10°), the maximum envelope profile (zenith angle 30°), and the mean profile (zenith angle 50°).

	Ch1	Ch2	Ch3
Profile-81 (min)	186.148 (186.183)	192.285 (192.409)	201.773 (201.760)
Profile-82 (max)	264.504 (264.577)	278.271 (278.435)	289.789 (289.975)
Profile-83 (mean)	221.278 (221.390)	232.850 (233.017)	244.197 (244.288)

Table 4. TIROS-N SSU channel brightness temperatures [K] from RTTOV for the min , max and mean profiles of the training set using, respectively, a zenith angle of 10°, 30° and 50°. Results based on the earlier Kobayashi coefficients are shown in brackets.

A statistical comparison of brightness temperatures based on an independent diverse set of 52 profiles is given in Table 5, showing the mean difference (new – old), the standard deviation from the mean difference, and the RMS difference. Only TIROS-N and NOAA-14 have been shown, since similar results were obtained for all other SSU platforms except NOAA-7.

SSU		TB: mean diff	TB: SD from mean	TB: RMS diff
TIROS-N	Ch 1	-0.1175	0.0723	0.1379
	Ch 2	-0.2268	0.1109	0.2525
	Ch 3	-0.3199	0.1588	0.3572
NOAA-14	Ch 1	-0.1206	0.0731	0.1410
	Ch 2	-0.2268	0.1112	0.2526
	Ch 3	-0.3019	0.1506	0.3374

Table 5. Comparison of RTTOV brightness temperatures [K] from new and existing SSU coefficients based on the independent profile set. Mean difference from the existing coefficients, standard deviation from the mean difference, RMS difference.

Thus RMS differences were less than a few tenths of a Kelvin, and increased with channel number, and therefore with increasing height of the weighting function peak. This increase was expected because the 51 level grid used for the new coefficients represents the peak of the weighting functions better than does the 44 level grid used by Kobayashi et al. NOAA-7, which is not recommended for use, shows an RMS difference of 0.6 K in Ch.3, which is probably due to the considerably lower cell pressure for that channel which had decreased rapidly after launch. This will have elevated the weighting function and accentuated the difference.

2.8.2 Change in cell pressure

The seals in the gas cells were not perfect, so RTTOV coefficients used to predict the channel optical depths for a given viewing path may not remain valid for the entire operational lifetime of the instrument. To reduce the impact of this, RTTOV-11 includes a parameterised correction scheme.

An analytical insight into the way the cell pressure, and other path variables, affects the transmittance to space, may be gained by assuming spectral lines are strong and non-overlapping, and by neglecting the temperature variation along the atmospheric path. An expression for the channel-averaged transmittance to space from a profile level j with pressure P_j along a generally slanting

atmospheric path with zenith angle θ may be obtained by integrating the corresponding expression for the weighting function in Taylor et al. (1972), and takes the form

$$\tau_{j,\theta} = \frac{1}{\left(A \sec \theta P_j^2 / P_{mean}^2 + 1\right)^{1/2}} \quad (2.8.4)$$

where $A = x / 2\Gamma L$, and x is the profile-dependent thickness of the CO₂ column at STP, Γ converts, in an average sense, the air-broadened CO₂ halfwidth to the corresponding self-broadened halfwidth, and L is the length of the gas cell.

The primary predictor, $P1$, for a run-time correction of the all-gas layer optical depth $\sigma_{j,\theta}$, derived as $\ln(\tau_{j-1,\theta} / \tau_{j,\theta})$ was based on (2.8.4), and a secondary predictor, $P2$, was used to address the residual variation. Thus

$$P1 = \ln \left[\frac{(A \sec \theta P_j^2 + P_{cell}^2)(A \sec \theta P_{j-1}^2 + P_{nom}^2)}{(A \sec \theta P_{j-1}^2 + P_{cell}^2)(A \sec \theta P_j^2 + P_{nom}^2)} \right] \quad (2.8.5)$$

$$P2 = \frac{P_{cell} - P_{nom}}{P_{cell} - P_j} \quad (2.8.6)$$

where P_j is the pressure at level j of the profile, P_{nom} and P_{cell} are the nominal and actual (user-defined) mean cell pressures for the given channel. In $P2$ the denominator is not allowed to fall below the layer depth. The corresponding coefficients were appended to the updated SSU coefficient files as an additional section.

As part of the validation of the correction scheme, RTTOV was first run without the correction scheme, using the updated coefficients based on the nominal channel cell pressures. It was then run with the correction scheme, which meant using the nominal coefficients as before, but applying the coefficients in the appended section of the file to predictors $P1$ and $P2$ based on values supplied for the 'actual' cell pressures P_{cell} for the three SSU channels. Results for the mean profile of the training set, again for just TIROS-N and NOAA-14, are shown in Table 6.

SSU		Without correction	With correction	Target
TIROS-N	Ch 1	223.489	223.873	223.880
	Ch 2	235.550	234.748	234.671
	Ch 3	245.994	245.126	245.052
NOAA-14	Ch 1	223.756	223.879	223.880
	Ch 2	235.613	234.752	234.671
	Ch 3	245.711	245.118	245.052

Table 6. Comparison of RTTOV brightness temperatures [K] for the mean profile of the training set using the updated coefficients with and without the new correction scheme.

The target cell pressures were here chosen to coincide with the nominal pressure for another SSU platform, NOAA-9, so that RTTOV coefficients would be available to obtain the third column in Table 6.

2.9 Optimising number of levels in radiometer coefficient files

RTTOV-10 introduced a new set of 51 levels for the fast optical depth. These were based on the earlier 43/44 levels with additional levels added at the top of the profile to improve the

representation in the stratosphere. They also included modifications to the two lowest levels in the profile. It was found subsequently that because these additional levels (in particular those at the top of the atmosphere) were added without reference to any analytic formula, the layer thicknesses of consecutive levels varied considerably at the top of the atmosphere and this could result in artefacts appearing in the Jacobians.

To mitigate this a new set of 54 levels were derived from a similar formula to that used to create the 101 levels used for high-resolution IR sounder coefficient files (Strow *et al*, 2003). The formula used to generate the levels is:

$$p(i) = (Ai^2 + Bi + C)^8 \quad (2.9.1)$$

where i is the level number (1 is the lowest level, so this is the opposite sense to RTTOV level numbering) and A , B and C are constants which are determined by setting $p(1) = 1050$, $p(33) = 300$ and $p(54) = 0.005$ hPa. The resulting 54 levels have slightly lower resolution than the 51 levels around 1-10 hPa, but equal or better resolution everywhere else in the profile. The new pressure levels are given in the RTTOV v11 user guide.

Figure 39 shows the layer delta-pressure for the 44, 51, 54 and 101 level profiles. Note the sharp discontinuity in the 51 level profile around level 12. The 54 level profile has smoothly varying layer thicknesses. Figure 40 shows Jacobians for several high-peaking AMSU-A channels for a profile on the 51 levels using a 51 level coefficient file: note the artefacts visible around 5 hPa (corresponding to level 12). Figure 41 shows the Jacobians for the same profile interpolated onto the 54 levels and using the 54 level coefficient file: no artefacts are visible. (Note the differing layer thicknesses result in different values for Jacobians for the two coefficient files).

Coefficients on 51, 54 and 101 levels were used to run simulations for the 52 diverse profile set. The 101 level profile has better vertical resolution everywhere compared to the other profiles so the 101 level radiances can be considered as a reference for comparisons. The 51 and 54 level radiances were compared to the 101 level radiances and the RMS differences are shown in Tables 7 and 8 for AMSU-A and HIRS. The only channels for which the RMS differences are larger for the new 54 levels are those which have a significant contribution from the 1-10 hPa region.

Channel	51L	54L
1	0.102	0.064
2	0.063	0.042
3	0.091	0.065
4	0.047	0.031
5	0.026	0.019
6	0.035	0.029
7	0.032	0.030
8	0.026	0.024
9	0.058	0.047
10	0.093	0.056
11	0.138	0.100
12	0.147	0.147
13	0.069	0.220
14	0.125	0.237
15	0.131	0.086

Table 7: RMS differences between 101L coefficients and 51L/54L coefficients for the 52 diverse profile set for AMSU-A. Green/red indicates the 54L RMS difference is lower/higher than that for 51L respectively.

Channel	51L	54L
1	0.078	0.045
2	0.055	0.067
3	0.034	0.038
4	0.044	0.034
5	0.049	0.035
6	0.046	0.036
7	0.050	0.037
8	0.059	0.025
9	0.107	0.076
10	0.074	0.045
11	0.172	0.141
12	0.246	0.259
13	0.027	0.010
14	0.022	0.014
15	0.022	0.017
16	0.036	0.027
17	0.015	0.008
18	0.011	0.002
19	0.025	0.008

Table 8: RMS differences between 101L coefficients and 51L/54L coefficients for the 52 diverse profile set for HIRS. Green/red indicates the 54L RMS difference is lower/higher than that for 51L respectively.

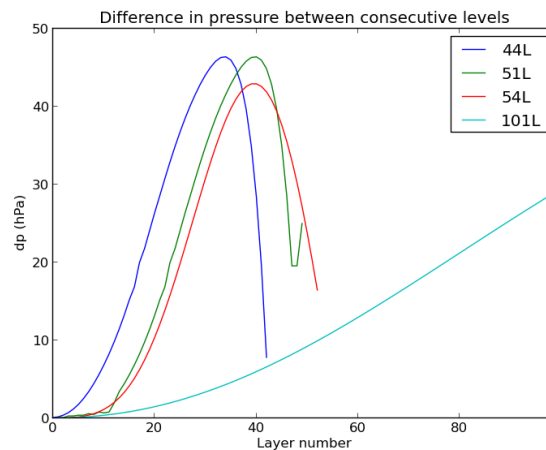


Figure 39: difference in pressure between consecutive levels for the standard RTTOV 44, 51, 101 and new 54 level profiles. Note the variable layer thickness and sharp jump around level 12 in the 51L profile.

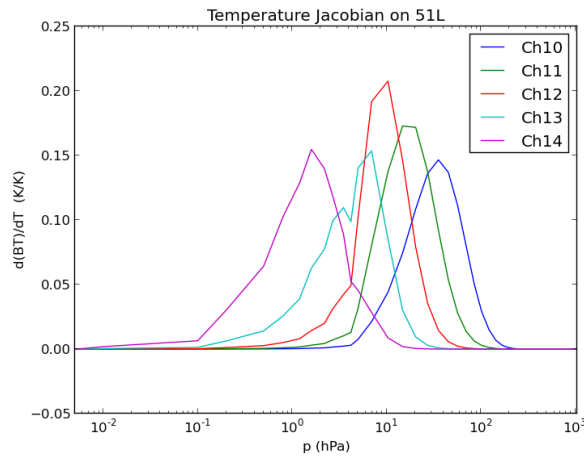


Figure 40: temperature Jacobians for high-peaking AMSU-A channels for an input profile and coefficient file on the RTTOV v10 51 levels: note the artefacts at around 5hPa.

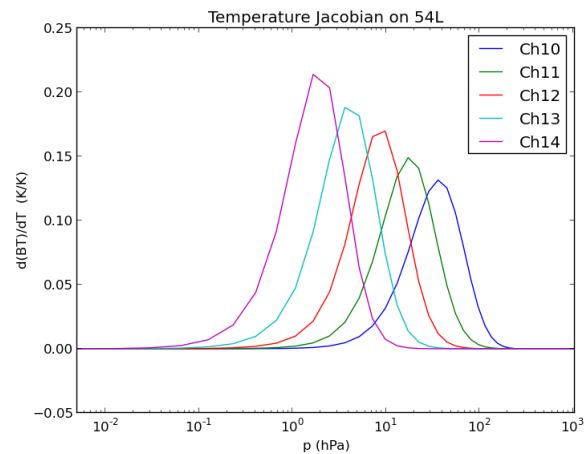


Figure 41: temperature Jacobians for high-peaking AMSU-A channels for an input profile and coefficient file on the new 54 levels.

2.10 Modifications to profile interpolation

The RTTOV interpolator introduced with RTTOV v9 was designed specifically so that Jacobians are interpolated correctly between user levels (typically GCM levels) and the coefficient levels. Typically the number of model levels exceeds the number of coefficient levels. When interpolating from a (relatively) dense set of levels to a (relatively) sparse set of levels, it is important that all of the input levels contribute to the interpolation. If a simple log-linear interpolation scheme is used, for example, then some input levels may not be used in the interpolation and this can result in “gaps” appearing in the resulting Jacobians (see Rochon *et al*, 2007). The Rochon interpolation scheme ensures that all input levels contribute to the interpolation, and furthermore, that each input level contributes with an equal weight in total to the interpolated profile.

However, when interpolating from (relatively) sparse to dense levels the Rochon interpolation can introduce oscillations in the interpolated profile. In RTTOV this typically happens when the optical depths calculated on the coefficient levels are interpolated back onto the user levels in preparation for the integration of the radiative transfer equation. The result is that Jacobians can exhibit jaggedness due to this second interpolation step (see figure 42).

To mitigate this for certain input/output layer combinations RTTOV v11 offers the capability to select between alternative interpolation methods. The default is the Rochon scheme. Users can also select log-linear interpolation which may offer a small performance improvement for direct model simulations (but should not generally be used for the adjoint or K models). A third option uses the Rochon interpolation for mapping from user to coefficient levels and log-linear interpolation for mapping from coefficient to user levels. If the input levels are significantly more dense than the coefficient levels (which is common for modern GCMs) then this option can significantly reduce the observed jaggedness (see figure 43). It does not eliminate the problem entirely however, so it is planned to offer further interpolation options in the future which will result in smoother Jacobians.

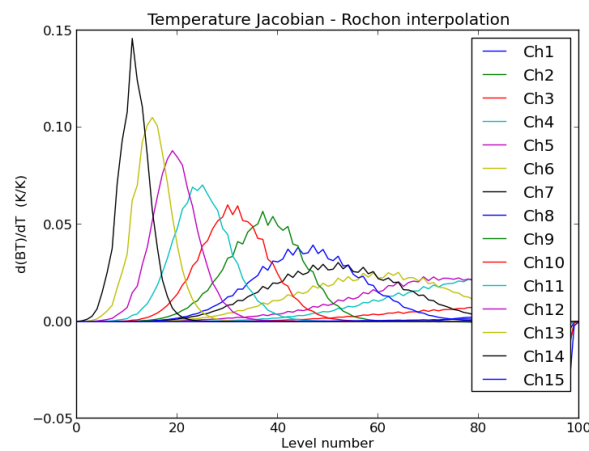


Figure 42: AMSU-A temperature Jacobians for a 101L input profile and 54L coefficient file using Rochon interpolation only.

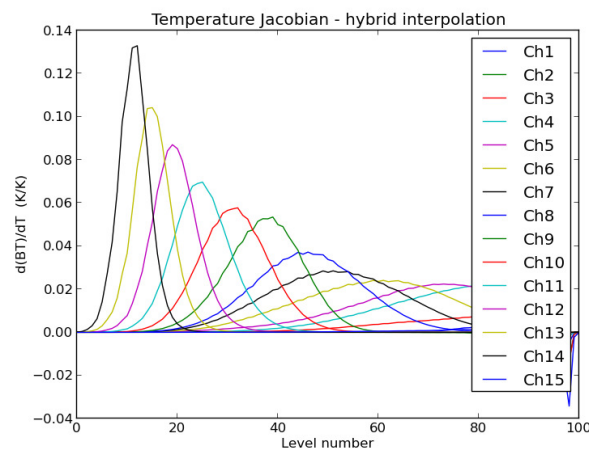


Figure 43: AMSU-A temperature Jacobians for a 101L input profile and 54L coefficient file using Rochon interpolation to map from user to coefficient levels and log-linear interpolation to map from coefficient to user levels.

<p>The EUMETSAT Network of Satellite Application Facilities</p>		<p>RTTOV-11 Science and Validation Report</p>	<p>Doc ID : NWPSAF-MO-TV-032 Version : 1.1 Date : 16/8/13</p>
---	---	---	---

2.11 Refinements in the Line-by-Line transmittance databases

2.11.1 Infrared transmittances

For all of the RTTOV-11 IR and VIS/NIR coefficient files the LBLRTMv12.2 model developed at AER (Clough et al., 2005) has been used together with the MTCKD continuum absorption version 2.5.2. For the LBL computations the AER v3.2 molecular database was used. AER v3.2 is built from HITRAN 2008 (Rothman et al., 2009) with notable improvements for molecules listed below:

- H₂O line positions and intensities are from Coudert et al. (2008),
- CO₂ line parameters were built using the CO₂ line mixing database of Lamouroux *et al.* (2010).
- CH₄ include line coupling parameters at 1300 and 3000cm⁻¹.
- O₂ is from HITRAN update for O₂ (Nov 2009). This was a complete replacement of the HITRAN 2008 O₂ line list.

Absorbing gases considered for line absorption are H₂O, CO₂, O₃, N₂O, CO, CH₄, O₂, NO, SO₂, NO₂, HNO₃, OCS and N₂, in addition with cross-sections of molecules CCl₄, CFC-11, CFC-12 and CFC-14. Except for RTTOV v9 trace gas predictors coefficients, H₂O and O₃ are the only varying gases. CO₂ is considered as a varying gas for the v8 predictors.

There have also been improvements to the LBLRTM model which include:

- i) New CO₂ line mixing coefficients
- ii) Introduction of temperature dependence of CO₂ continuum in the CO₂ band head region
- iii) Modification of CO₂ continuum coefficients between 2000 and 3000 cm⁻¹
- iv) Modification of H₂O self continuum coefficients between 2000 and 3200 cm⁻¹

Training profiles are from the 83 diverse profile set from the 91L ECMWF analyses interpolated to 101 levels (Chevallier et al., 2006).

Relative to RTTOV v10, the boundary layer concentration of the fixed gases has been scaled to 392.9 ppmv for CO₂ 325 ppbv for N₂O, 1.809 ppmv for CH₄, 0.0865 ppbv for CCl₄, 0.2366 ppbv for CFC-11, 0.5255 ppbv for CFC-12, 0.0795 ppbv for CFC-14 (corresponding to 2012 concentrations).

Line-by-Line (LBL) calculation outputs are nadir layer optical depth at LBL spectral resolution. Interpolation on to 54 levels is done from LbL nadir optical depths (log-linear interpolation). Top of atmosphere to level transmittances at diverse secant angles are calculated from nadir optical depths.

Two LbL databases are built for later convolution of instrument spectral response functions, the first is for infrared radiometers [500 – 3300 cm⁻¹] with a spectral resolution of 0.25 cm⁻¹, and for visible and near infrared radiometers [2000 – 25500 cm⁻¹] or [0.392 – 5 μm] with a spectral resolution of 1.0 cm⁻¹. Secondly for the infrared hyperspectral instruments these use the LbL database convolved to 0.001 cm⁻¹ resolution.

On the top of Figure 44 is displayed the infrared total transmittance in percent (top) for all molecules considered above calculated from LBLRTMv11.1 (in blue) and from LBLRTMv12.2 (in red). For calculations, the profile number 83 and secant number 1 were considered. On the bottom of Figure 44 is displayed the difference between total transmittances from v12.2 minus v11.1. The major change above 2000 cm⁻¹ is mainly explained by the difference in water vapour continuum. On the bottom of Figure 45 is displayed the difference between v12.1 (that was used for RTTOV v10.2 coefficients) and v12.2. No large differences are found between these two versions.

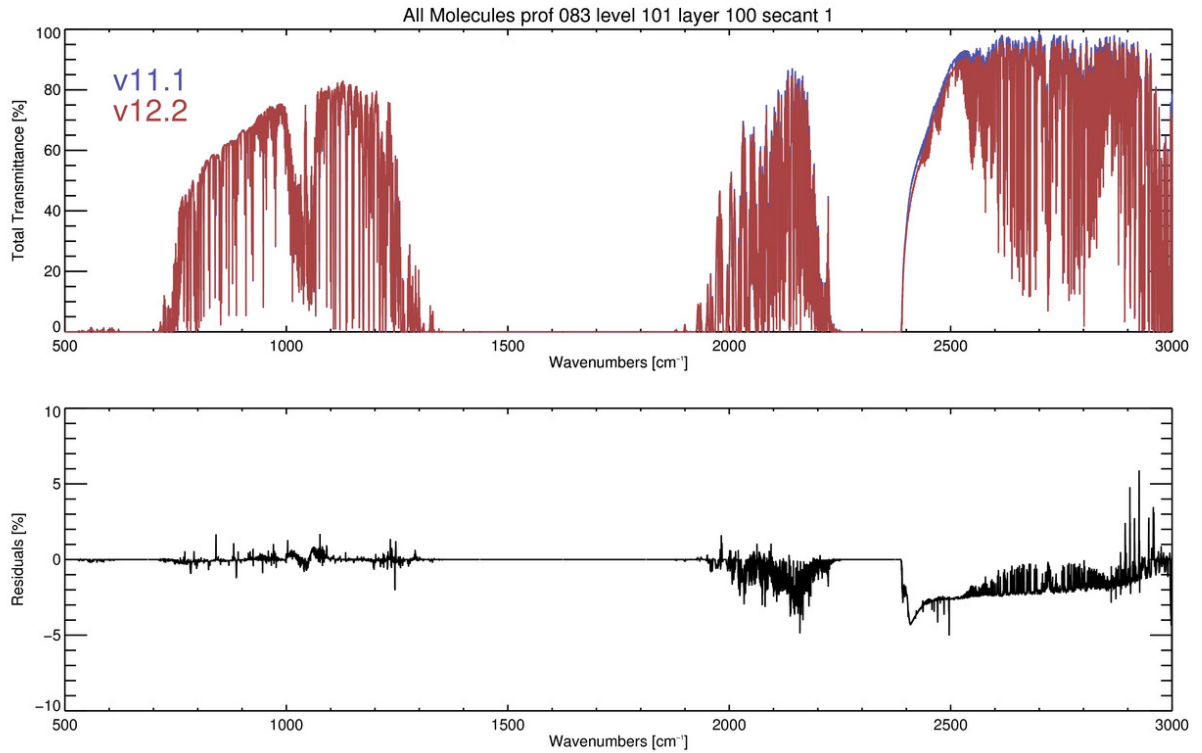


Figure 44. Infrared total transmittance in percent (top) and residuals (bottom) for all molecules from LBLRTMv11.1 (in blue) and from LBLRTMv12.2 (in red). Profile number 83, 101 levels and nadir were considered.

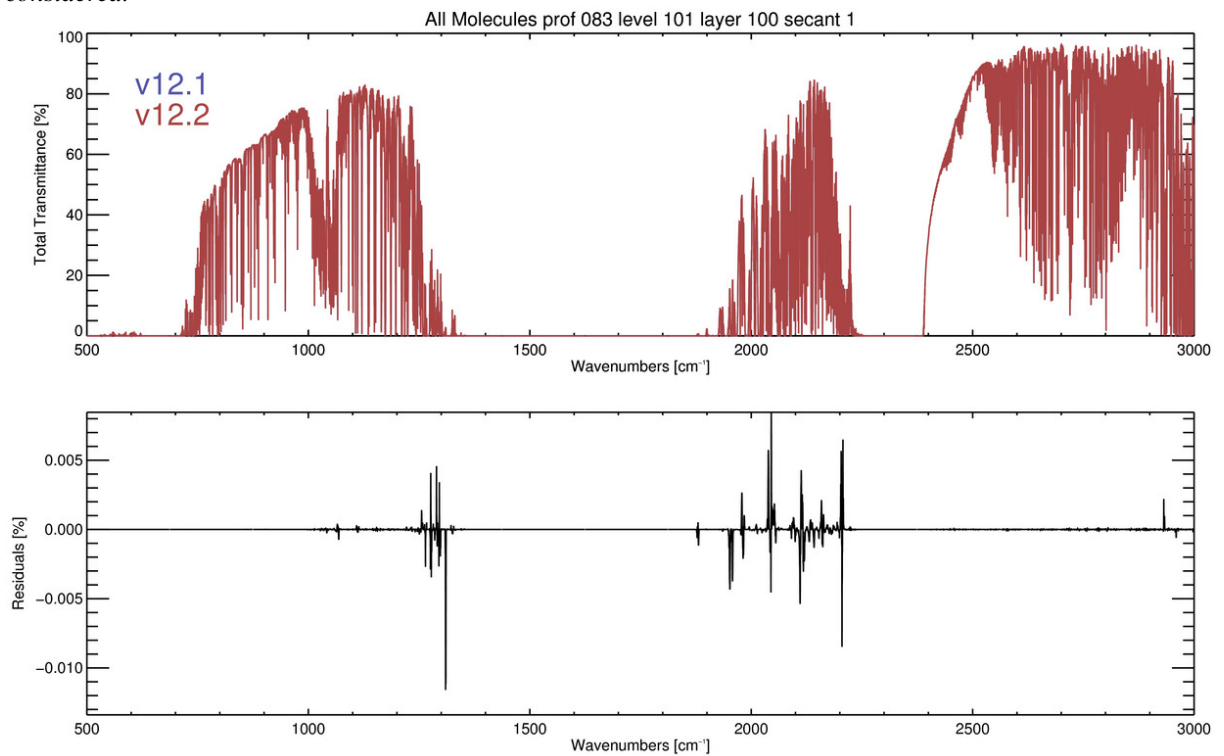


Figure 45. Infrared total transmittance in percent (top) and residuals (bottom) for all molecules from LBLRTMv12.1 (in blue) and from LBLRTMv12.2 (in red). Profile number 83, 101 levels and nadir were considered.

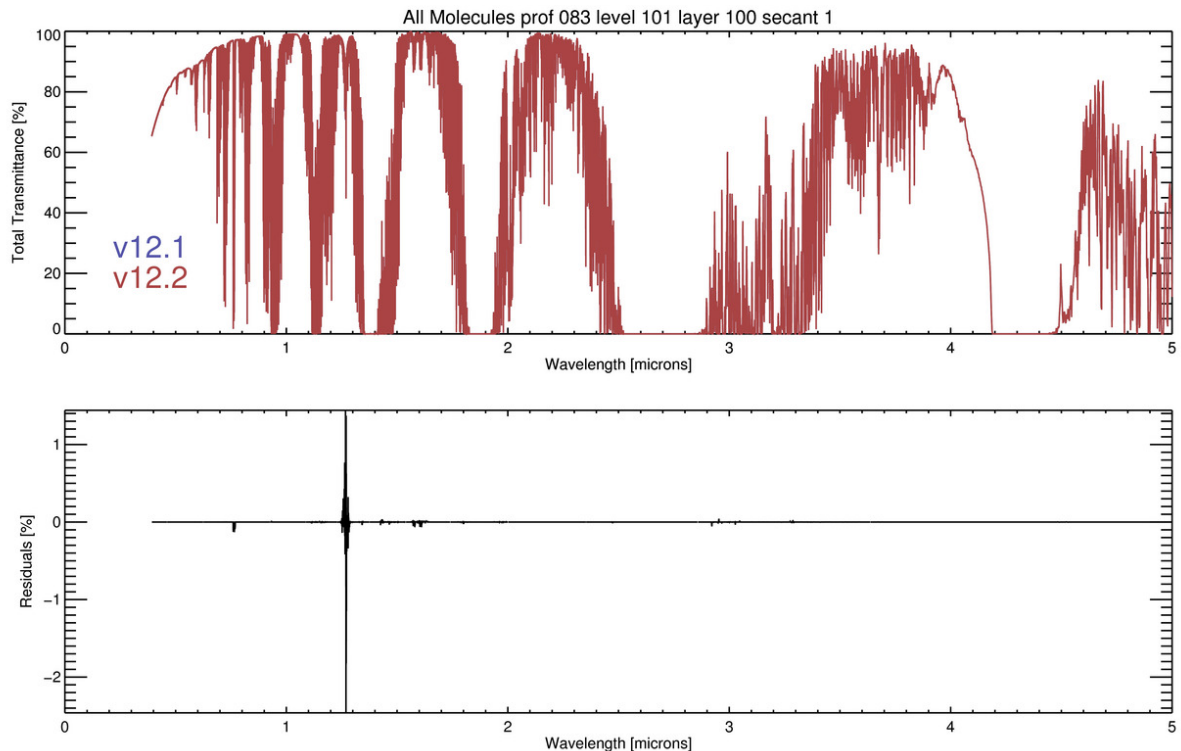


Figure 46. Visible and near Infrared total transmittance in percent (top) and residuals (bottom) for all molecules from LBLRTMv12.1 (in blue) and from LBLRTMv12.2 (in red). Profile number 83, 101 levels and nadir were considered.

On Figure 46 is displayed the visible and near infrared total transmittance for v12.1 and for v12.2. Here, the differences are explained by the improvement in O₂ and CO₂ line parameters.

2.11.2 Microwave transmittances

The AMSUTRAN line-by-line model calculates channel-averaged transmittances to space for the RTTOV microwave sensors, with water vapour as the only variable gas, and with oxygen, nitrogen and, optionally, ozone as the mixed gases. As for RTTOV-10, ozone is only included for channels near 183 GHz, where it exhibits a systematic decrease in brightness temperature of a few tenths of a degK. There have been no modifications to the LBL microwave transmittance code for RTTOV-11.

2.12 Changes to the microwave scattering code for RTTOV-11

Recent developments for RTTOV-SCATT have focused on improving the pre-computed tables of bulk optical properties in order to produce more realistic simulations of scattering at higher microwave frequencies (e.g. above 30 GHz). Especially in deep convective areas where frozen hydrometeors dominate the radiative transfer, the existing optical tables tend to generate excessive scattering at 30 GHz to 50 GHz and insufficient scattering at 150 GHz to 183 GHz.

The existing optical tables are computed using Mie theory, which is now considered to be inadequate to represent frozen hydrometeors (e.g. Kulie et al. 2010, Petty and Huang 2010). It is better to use discrete dipole simulations to account for their complex three dimensional shapes. Hence, the facility has been added to generate optical tables for RTTOV-SCATT using the discrete dipole databases of Liu (2008), who simulated the optical properties of a variety of ice columns,

plates, rosettes and two idealised snowflakes. The correct choice of size distribution is also crucial, and more flexibility has been added there too. In the ECMWF system, the statistics of FG departures can be substantially improved by using a Liu sector snowflake and the Field et al. (2007) size distribution, rather than the old Mie sphere (see figure 47).

Although more flexibility has been added to the generation of the RTTOV-SCATT optical tables, we have not yet updated the official distribution. The official files remain based on Mie theory for snow and ice hydrometeors. Work is ongoing to decide the best choices of size distribution and discrete dipole particle shape, after which the official tables will be updated. However, users can already experiment to see what works best in their own applications. All this will be more fully documented in a forthcoming report by Geer and Baordo (2013).

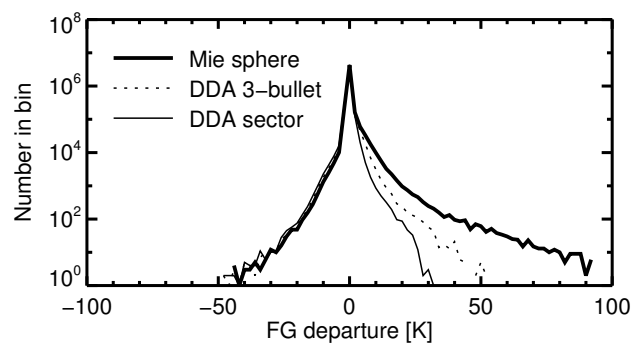


Figure 47. Histograms of first guess departures in the ECMWF system for the 52.8 GHz channel on SSMIS, using a variety of different scattering models for the snow hydrometeor type. For the discrete dipole (DDA) models, a Field et al. (2007) size distribution has been used. For the Mie sphere, Marshall-Palmer has been used.

3. Testing and Validation of RTTOV-11

To ensure no bugs have entered in the RTTOV code during the introduction of the above changes an extensive set of tests were applied to the new model before it was released to users. There was also an extensive series of comparisons carried out, not described here, between RTTOV-10 and RTTOV-11 transmittances, radiances, jacobians and surface emissivities from the direct, TL, AD and K codes to check there are no differences during the code development except those anticipated. The tests conducted are in the RTTOV-11 test plan document and users can run these tests to verify the performance of the code on their platform when they first install RTTOV.

To ensure there are no significant unexpected changes from RTTOV-10 the new RTTOV-11 code is validated in several ways:

- The RTTOV-11 top of atmosphere radiances computed using the latest (LBLRTMv12.2, 54L) model transmittances from a 52 ECMWF profile independent set (Chevallier, 2000) for HIRS, ASMU-A, ASMU-B and IASI. This tests the differences of the brightness temperatures simulated by RTTOV-11 with the new coefficients (LBLRTMv12.2, 54L) and previous versions of RTTOV and coefficients.
- The jacobians for RTTOV-11, RTTOV-10 and RTTOV-9 are compared for AMSUA (v7 predictors 54L) for the 52 profile set on 44L (43L for RTTOV-9).
- Comparisons of RTTOV-11 and RTTOV-10 simulations with observations using the ECMWF IFS for many sensors including HIRS, AMSU and IASI.

		RTTOV-11 Science and Validation Report	Doc ID : NWPSAF-MO-TV-032 Version : 1.1 Date : 16/8/13
---	---	---	--

The validation results described below are for ATOVS and IASI but the performance of the new RTTOV-11 model for all other instruments is similar. In addition where changes have been made to the calculations for RTTOV-11 (e.g. Non-LTE, Lambertian scattering) then specific validation tests are made as described in section 2 or in the references.

3.1 Validation of top of atmosphere radiances

3.1.1 Comparison of simulations

The primary outputs from RTTOV are the top of atmosphere radiance for each channel and so this is the main parameter for which the RTTOV-11 simulations are checked and compared with the corresponding RTTOV-9 and 10 values. The main reason for differences between RTTOV-10 and RTTOV-11 computed radiances are due to the new line-by-line transmittances with more up to date spectroscopy. Comparisons between RTTOV-10 (v10.2) and RTTOV-11 (v11.1) were made according to the parameters listed in Table 9 for calculations on a 52 diverse profile set. The mean differences were then plotted in the following figures.

Parameters	RTTOV-9	RTTOV-10	RTTOV-11
Number of layers for optical depth calculation	43 (0.1-1013hPa) except for IASI: 101 (0.005-1050hPa)	51 (0.005-1050hPa) except for IASI: 101 (0.005-1050hPa)	54 (0.005-1050hPa) except for IASI: 101 (0.005-1050hPa)
Input Profile set direct/jacobians	52 Profiles on 101L/43L	52 Profiles on 101L/44L	52 Profiles on 101L/44L
IR Transmittances			
Spectroscopic data for HIRS and IASI test runs	GENLN2/HITRAN-96 (HIRS) LBLRTMv11.1/ HITRAN2006/GEISA (IASI)	LBLRTMv12.1/ AER 3.1 (HIRS) LBLRTMv11.1/ HITRAN2006/GEISA (IASI)	LBLRTMv12.2/ AER 3.2 (HIRS) LBLRTMv11.1/ HITRAN2006/GEISA (IASI)
Emissivity assumed	0.98	0.98	0.98
Optical depth predictors	Version 7 HIRS Version 9 IASI	Version 7 HIRS Version 9 IASI	Version 7 HIRS Version 9 IASI
MW Transmittances			
Spectroscopic data	Liebe 89/92 Mean layer values	Liebe 89/92 Curtis-Godson	Liebe 89/92 Curtis-Godson
Emissivity assumed	0.6	0.6	0.6
Optical depth predictors	Version 7	Version 7	Version 7

Table 9. The parameters assumed for the RTTOV-9, RTTOV-10 and RTTOV-11 radiance and Jacobian comparisons

The results are shown for NOAA-15 HIRS channels in Figure 48 using version 7 predictors throughout. The first comparison was to compare the effect of the change to a new line-by-line radiative transfer model to compute the transmittances (see section 2.11.1) These results show that different biases will be seen when RTTOV-11 replaces RTTOV-10 or RTTOV-9 but that the differences between v10 and v11 are small (<0.05K) except for the high peaking stratospheric channel where the different layering has had an impact on the computed radiance. Differences with RTTOV-9 are greater (up to 0.35K) due to more significant changes in the layering including the improved treatment at the top of the profile introduced with RTTOV-10 and also RTTOV-9 coefficients being based on much older underlying spectroscopy. Note the 51L coefficients used for RTTOV-10 can also be used with RTTOV-11 and give the same results as RTTOV-10.

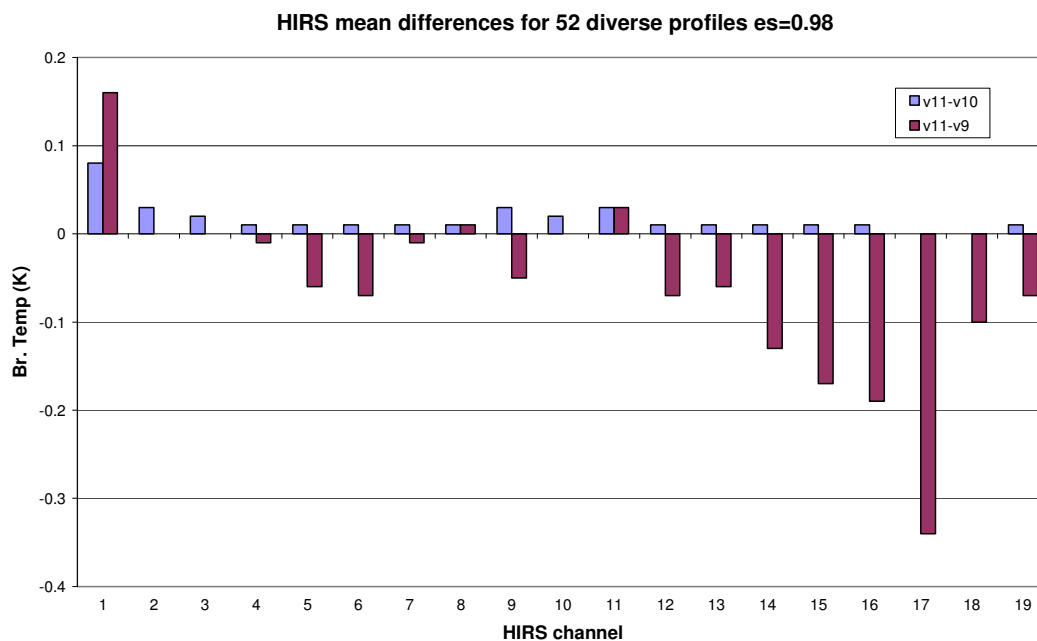


Figure 48. Differences between RTTOV-11 and RTTOV-10/RTTOV-9 HIRS simulations averaged over 52 diverse atmospheric profiles.

For NOAA-15 AMSU-A channels the results are shown in Figure 49 using version 7 predictors. The v11 – v10 differences are small (<0.25K) due to the move from 51L to 54L whereas the v11 – v9 differences can be up to 2K due to the different layering (43L to 54L), change from mean layer to Curtis-Godson and the revised treatment at the top of the profile.

For AMSU-B/MHS channels the v11-v10 differences are smaller (<0.05K) as shown in Figure 50. The change in radiative transfer (mean-layer to Curtis-Godson) and coarser layering (43L) result in larger differences for v11 – v9.

Finally the differences for a selection of IASI channels is show in Figure 51 using the version 9 predictors which include trace gases. There are no differences between v11 and v10 as the coefficient files are identical. For RTTOV-9 there are small differences (<0.1K) in the high peaking channels due to the revised treatment of the top layer in RTTOV which was introduced in RTTOV-10. A new IASI version-9 predictor coefficient file including trace gases will be generated for RTTOV-11 after the release of the code with the latest spectroscopy.

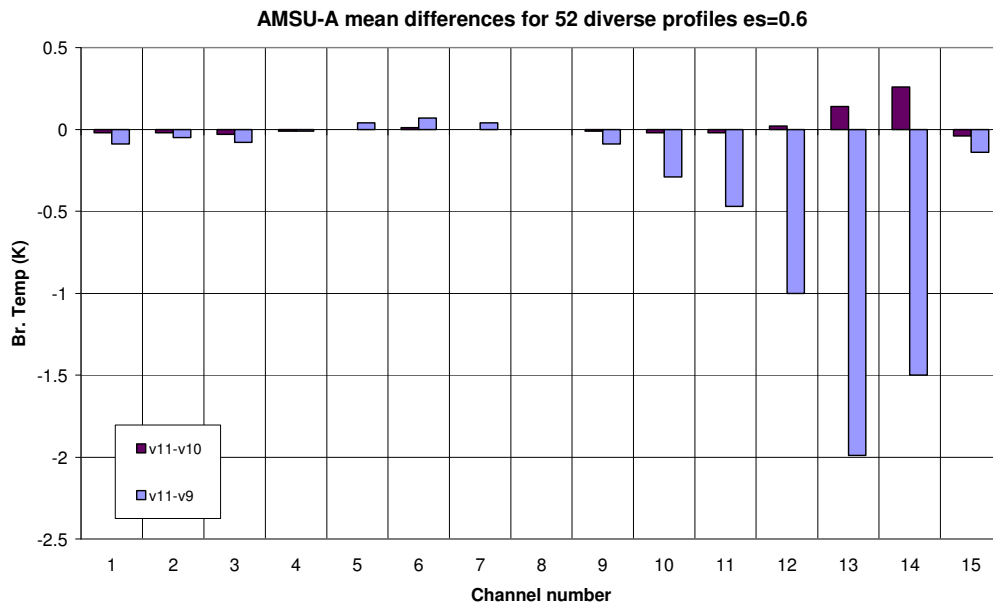


Figure 49. Differences between RTTOV-11 and RTTOV-10/RTTOV-9 AMSU-A simulations averaged over 52 diverse atmospheric profiles.

Total transmittances were also compared as shown in Figure 52 for AMSU-A and Figure 53 for HIRS but the different layering between models made it difficult to compare layer transmittances between RTTOV-10 and 11 as the interpolation will always introduce some small differences. The HIRS transmittance differences are bigger due to the new underlying spectroscopy used in the coefficients.

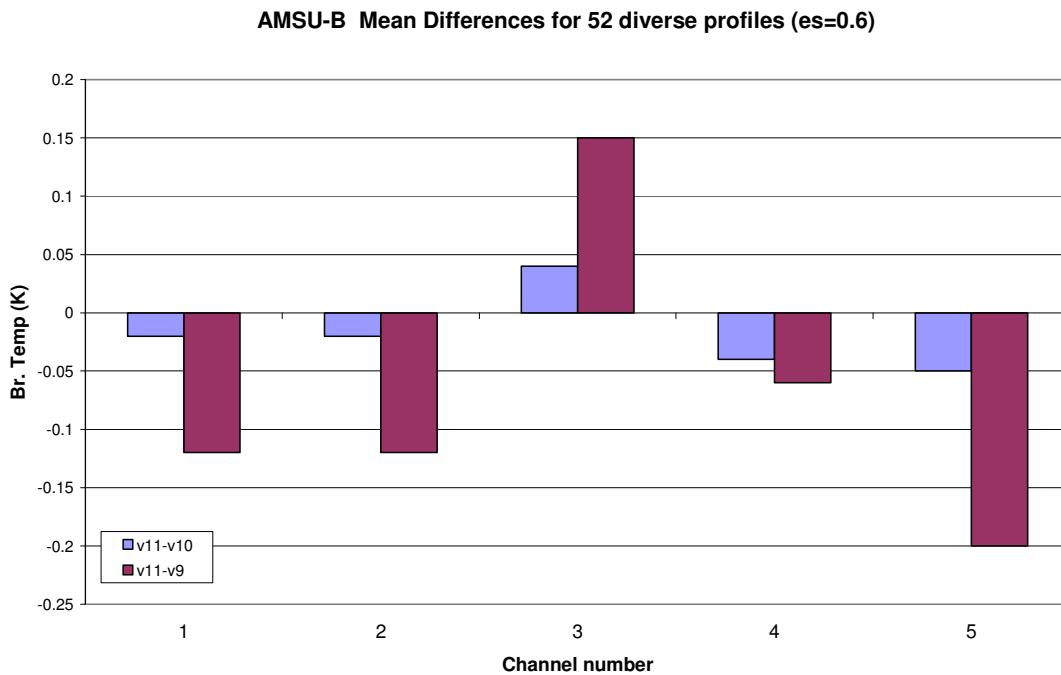


Figure 50. Differences between RTTOV-11 and RTTOV-10/RTTOV-9 AMSU-B/MHS simulations averaged over 52 diverse atmospheric profiles.

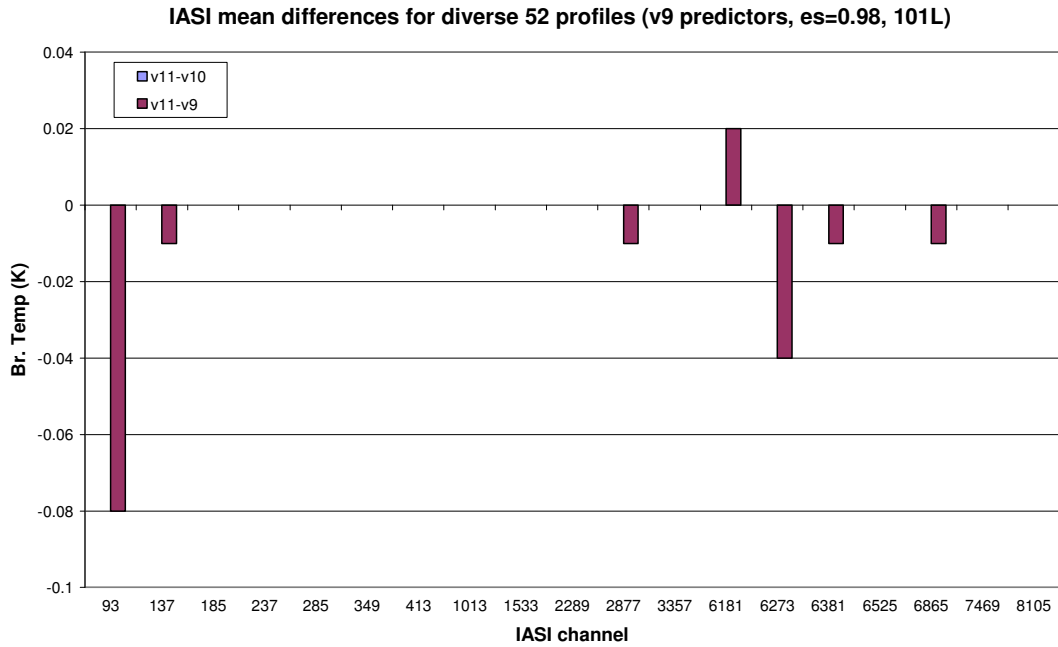


Figure 51. Differences between RTTOV-11 and RTTOV-10/RTTOV-9 IASI simulations averaged over 52 diverse atmospheric profiles.

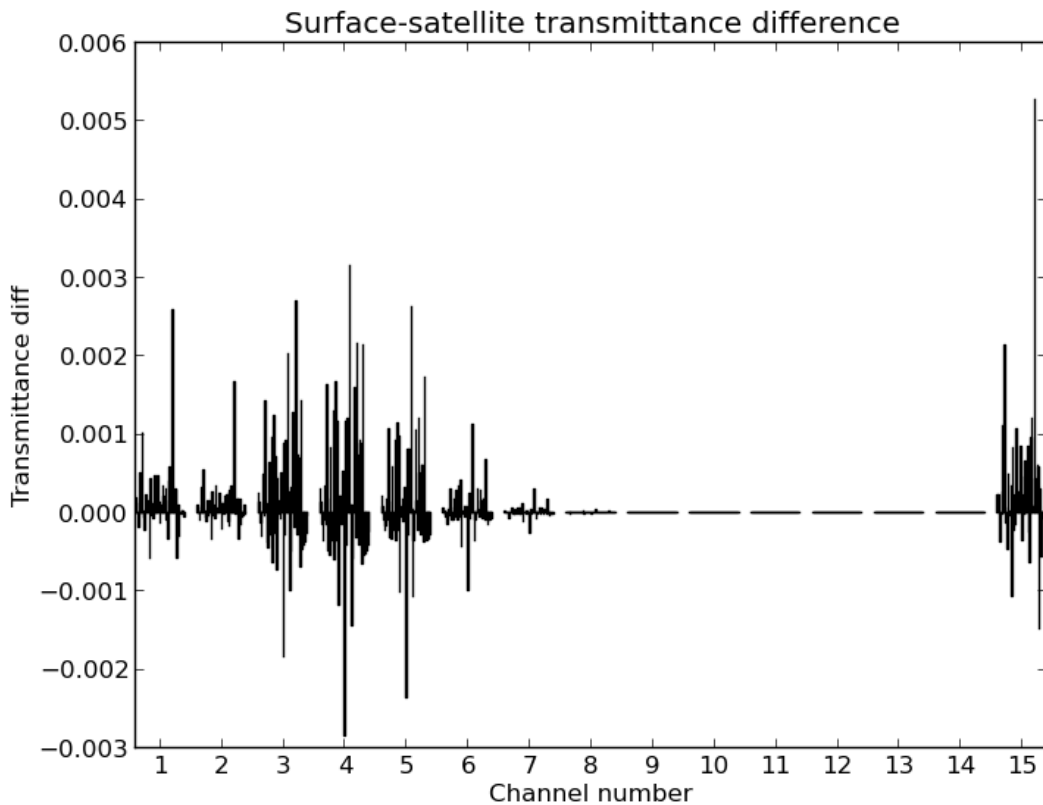


Figure 52. Differences between RTTOV-11 and RTTOV-10 in total column transmittances for AMSU-A channels for all 52 diverse profiles.

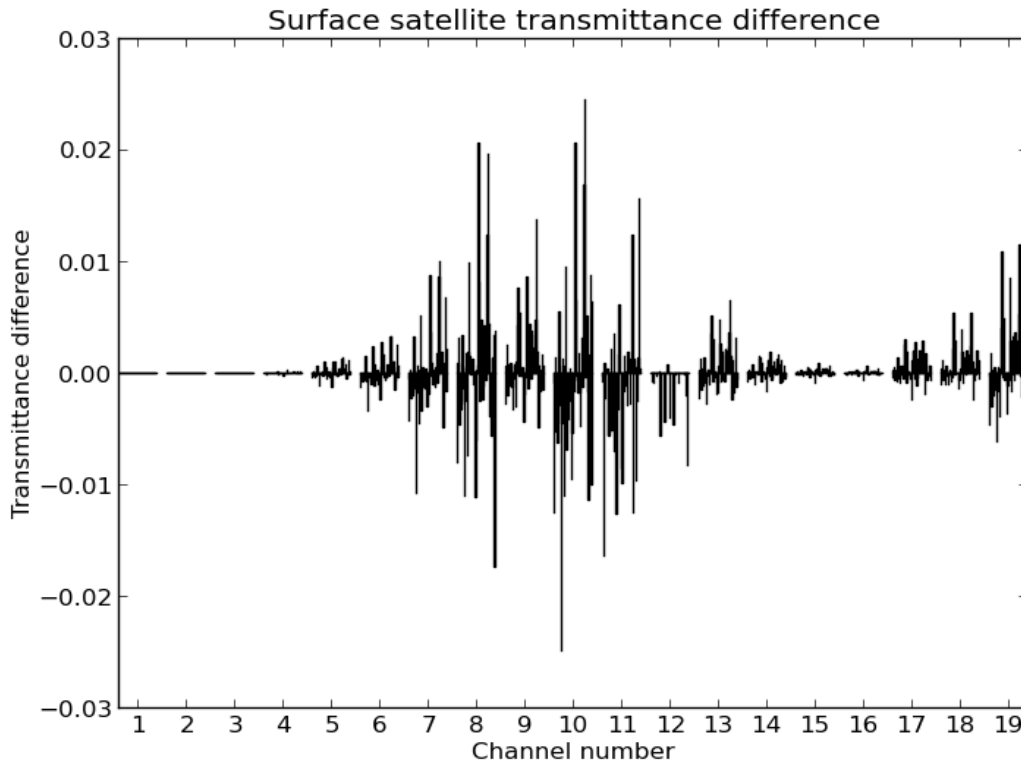


Figure 53. Differences between RTTOV-11 and RTTOV-10 in total column transmittances for HIRS channels for all 52 diverse profiles.

3.1.2 Comparison with observations

A comparison of RTTOV-10 and RTTOV-11 radiances with coincident observations is made using the ECMWF IFS model fields for several different instruments. A two month run of the IFS model from 1 June 2012 to 1 August 2012 was run with the RTTOV-10 (control) and RTTOV-11 (experiment) using the ECMWF 12 h 4DVAR system, with a reduced spatial resolution of T511 (40 km) and 137 levels in the vertical (with the model top at 0.01 hPa). As there are no changes specific to the IFS-version of the use of RTTOV-11 and the same coefficient files were used in both experiments (RTTOV-11 files are the same as the RTTOV-10 files) RTTOV-11 should give almost identical results to the RTTOV-10 code.

Figure 54 shows statistics of differences between first guess departures (solid black line) with RTTOV-11 and RTTOV-10 over the Northern Hemisphere extra-tropics for NOAA-18 AMSU-A, AQUA AIRS and TRMM TMI for a 12 h period covering 1 June 2012, 0Z. As expected, the non-zero differences between the first guess departures from the two experiments are only due to slightly different samples being used, due to small differences in the quality control checks. The new RTTOV-11 code gives no difference in the simulated brightness temperature compared to the RTTOV-10 when the same profile is provided, for all infrared and microwave sensors assimilated.

In the following we will give a characterisation of the OMB (observation-first guess) and OMA (observation-analysis) departure statistics, based on statistics for METOP-A AMSU-A (Fig. 55) and AIRS (Fig. 56) collected from 1 June 2012 to 1 August 2012. The change to RTTOV-11 does not show any significant differences in standard deviations. The biases are all similar as expected, with small differences being due to slightly different samples being used. For other assimilated

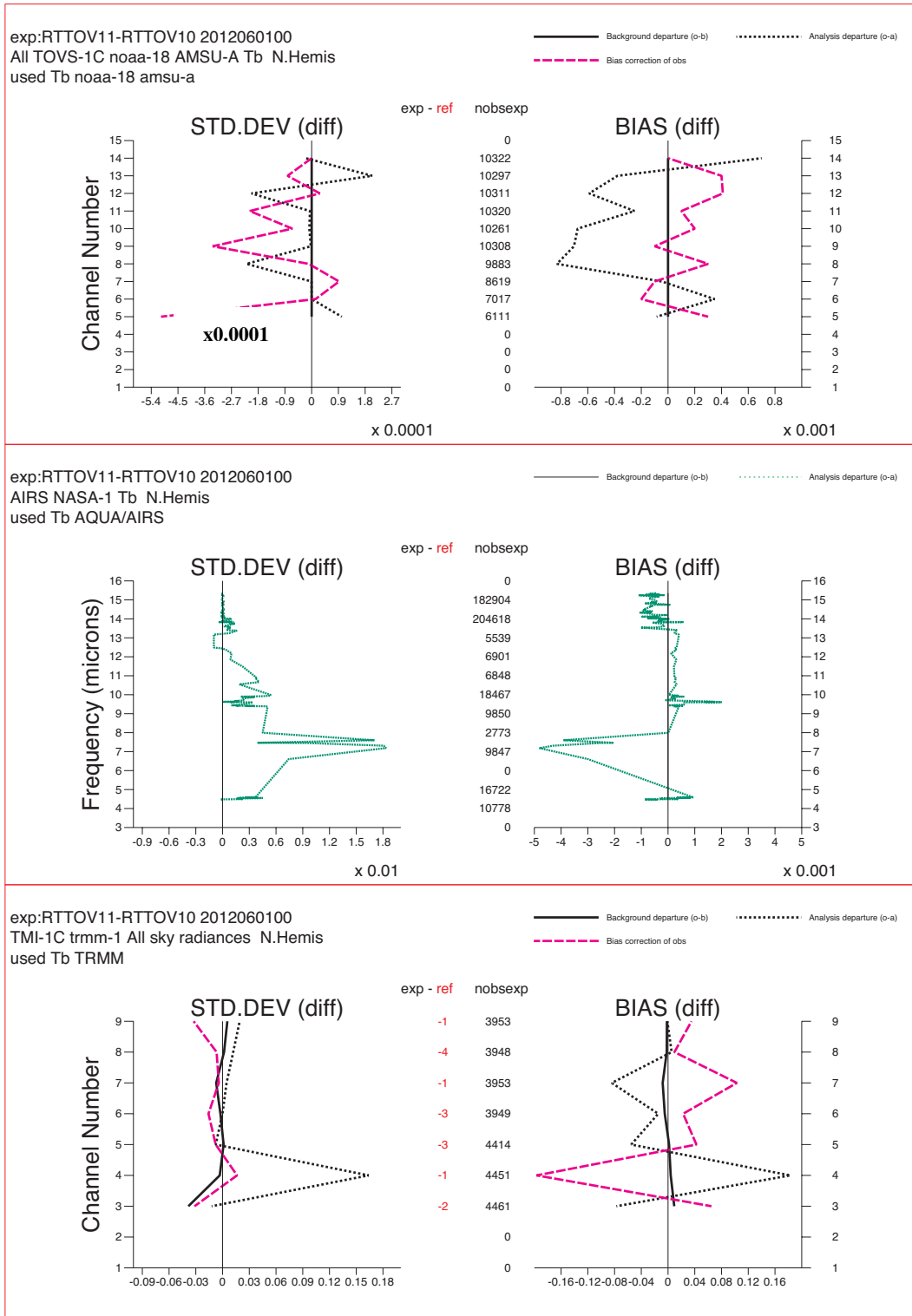
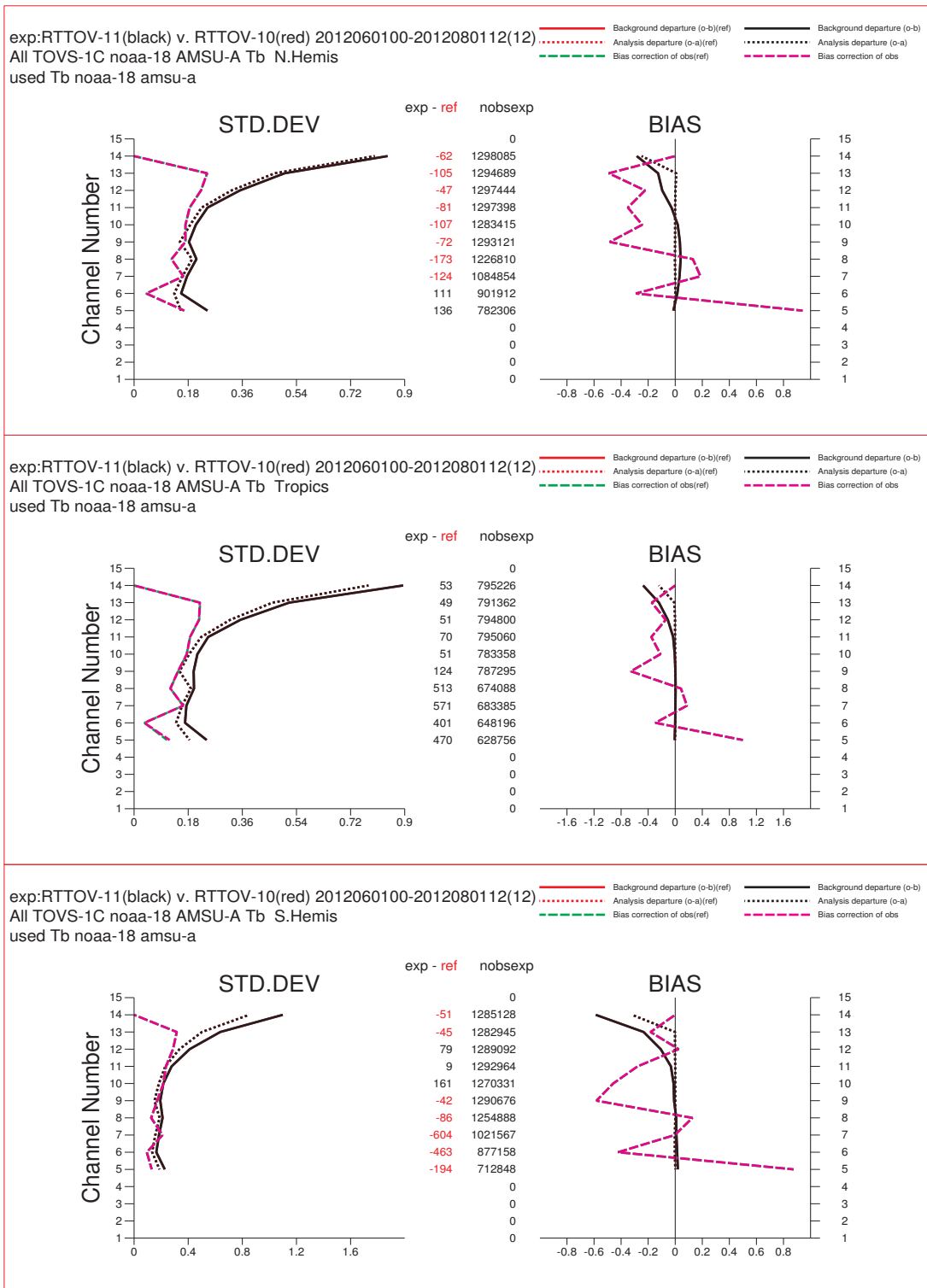


Figure 54. Departure statistics of differences between the RTTOV-11 experiment and the RTTOV-10 control experiment for NOAA-18 AMSU-A (top), AQUA AIRS (middle) and TRMM TMI (bottom) over the Northern Hemisphere extratropics for a 12 h period covering 1 June 2012, 0Z. The solid black line shows the difference between first guess departures from the two experiments, the dotted black line the difference between the analysis departure statistics. The difference in bias correction values from the two experiments is shown in magenta line. The number of observations for the RTTOV-11 experiment is given in the middle, including the difference between the RTTOV-11 and the RTTOV-10 control experiment. The statistics are based in used observations. Note below each plot is a scaling factor to apply to the axis values.



n)

for the period 1 June -1 July 2012. Statistics for the RTTOV-11 experiment are shown in black, whereas statistics for the RTTOV-10 control experiment are shown in red (though obscured by black lines), with solid lines showing first guess departure statistics (observation-first guess) and dotted lines analysis departure statistics. Bias corrections are also shown, for the RTTOV-11 experiment in magenta and for the control experiment in green. The number of observations for the RTTOV-11 experiment is given in the middle, including the difference between the RTTOV-11 and the RTTOV-10 control experiment. The statistics are based on assimilated observations.

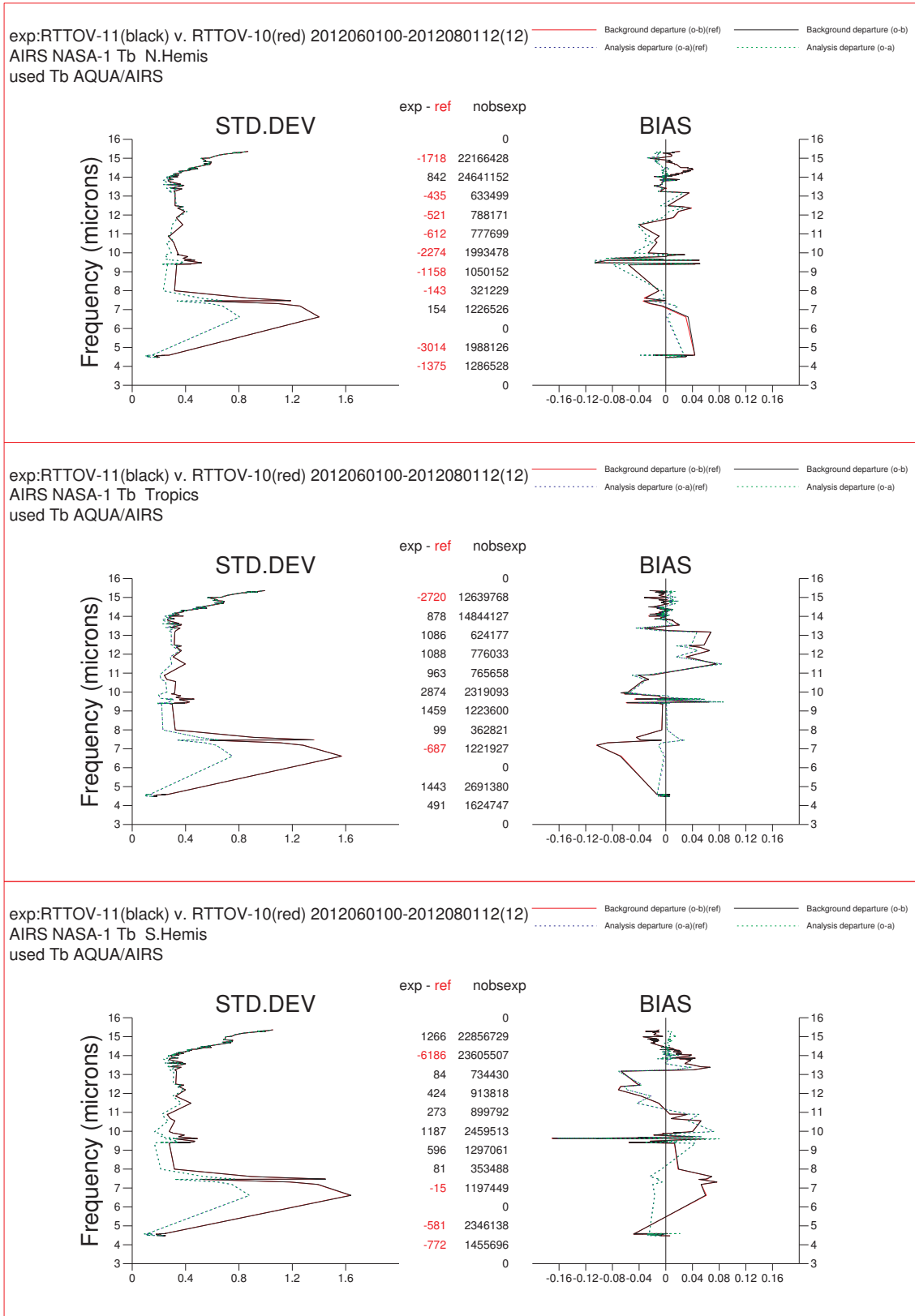


Figure 56. As Fig. 55 but for AIRS on AQUA.

observations, there is no significant impact on the departure statistics, suggesting no significant change to the quality of short range forecast or the analysis.

3.2 Comparison of Jacobians

The accuracy of the jacobians computed by RTTOV is important to document for radiance assimilation users as they are instrumental in modifying the NWP model analysis. The differences in jacobians between RTTOV-11 and RTTOV-10/9 are illustrated here for the 15 channels of AMSU-A but the same characteristics are shown by all sounders. The jacobians were computed using the coefficients listed in Table 9 and for the 52 diverse profile set which are independent from the coefficient generation. A surface emissivity of 0.6 was assumed for all channels. To allow comparisons back to RTTOV-9 the jacobians were compared on 44 levels (43 for RTTOV-9) using the default interpolation (Rochon et. al. 2007) from coefficient levels to user input levels in RTTOV-10 and 11 and 43L coefficients for RTTOV-9 with no interpolation. The mean Jacobians for the 52 profiles are shown in Figure 57 for the 15 AMSU-A channels.

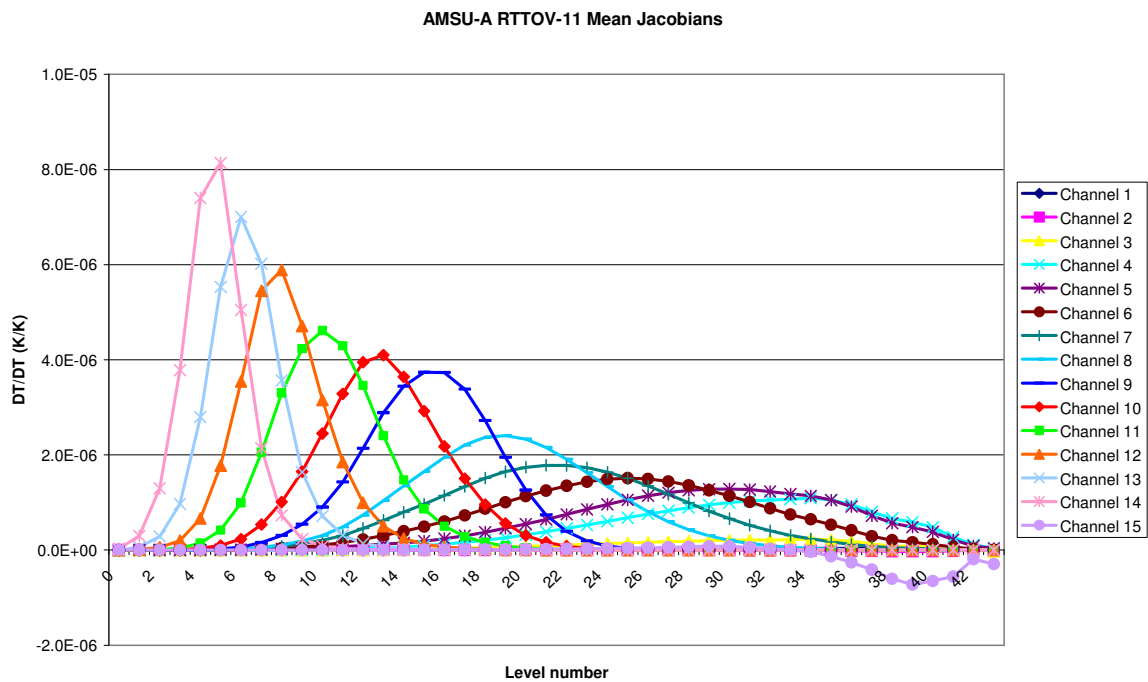
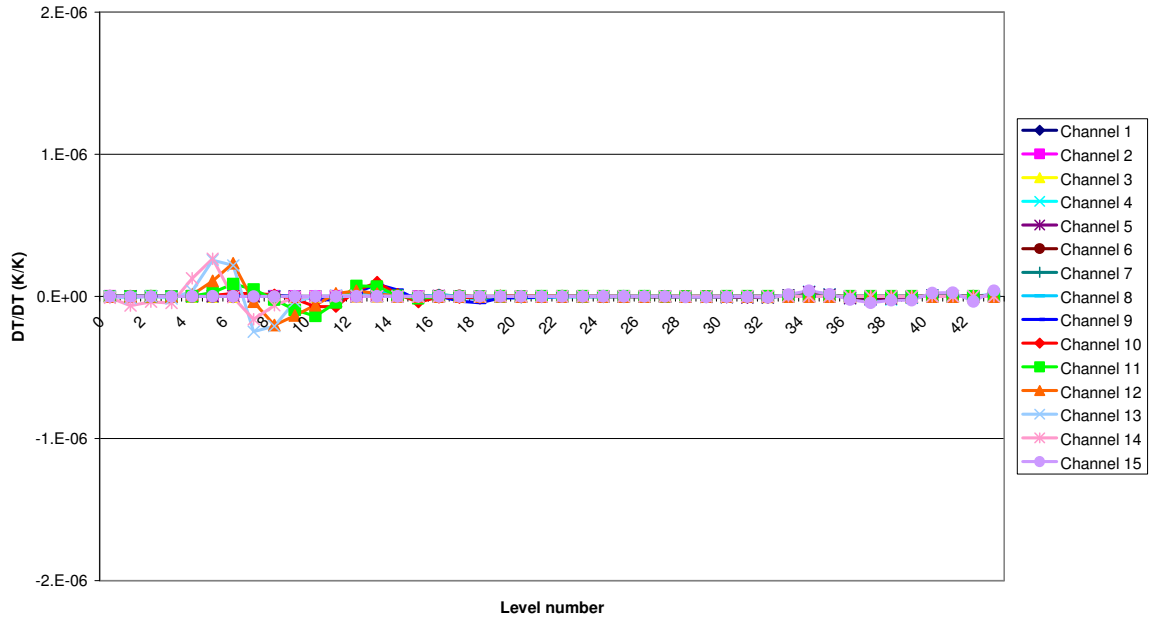


Figure 57. Mean jacobians for 52 diverse profiles and fixed surface emissivity of 0.6 for all 15 AMSU-A channels computed by RTTOV-11.

The differences in the computed Jacobians are shown in Figure 58. For RTTOV-10 to RTTOV-11 the differences are small and related to the increase in the levels (51 to 54) on which the optical depth calculation is performed. For RTTOV-9 to RTTOV-11 the differences are more significant and for the high peaking channels they just relate to the improved treatment of the profile top from RTTOV-10 onwards. The smaller differences seen for channel 15 which peaks close to the surface are due to the move from layer mean averages to Curtis-Godson computed layer radiances which was also implemented in RTTOV-10.

AMSU-A RTTOV-11 - RTTOV-10



AMSU-A RTTOV-11 - RTTOV-9

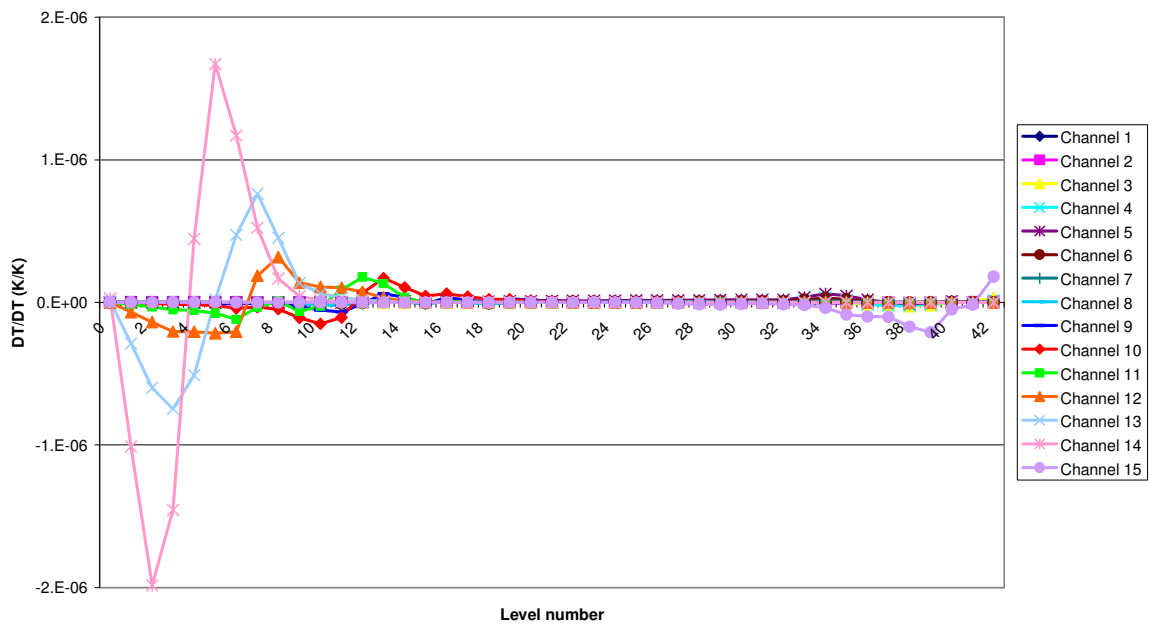


Figure 58. Mean differences in jacobians for 52 diverse profiles and fixed surface emissivity of 0.6 for all 15 AMSU-A channels for RTTOV-11 minus RTTOV-10 (top panel) and RTTOV-11 minus RTTOV-9 .

		RTTOV-11 Science and Validation Report	Doc ID : NWPSAF-MO-TV-032 Version : 1.1 Date : 16/8/13
---	---	---	--

4. Summary

The latest version of RTTOV, RTTOV-11 has been enhanced in a number of ways described in this report and also optimised to run faster on all platforms (see performance report on RTTOV-11 web page). The new version of the model has been validated in several ways to show the same or improved performance for the prediction of satellite top of atmosphere radiances both for clear air, cloudy, aerosol and precipitating profiles and is backward compatible to the previous version of RTTOV. The changes have been validated as described in this document or in the references given.

Referring to the main list of changes made between RTTOV-10 and RTTOV-11 given in section 2 the following summary can be made:

Extension of wavelength range which can be simulated to enable visible and near infrared channels simulations.

Realistic visible and near infrared clear sky radiances can now be computed using RTTOV. Simple cloud affected radiances can also be calculated which provide good qualitative imagery but more work is needed on a better fast model for scattering in the visible channels by clouds and aerosols to obtain quantitative radiances suitable for assimilation and physical retrievals.

New land surface BRDF atlas to specify input surface reflectance for visible channel simulations.

This atlas is required to enable the simulation of reflected visible/NIR radiances.

Improved profile interpolation from user levels to RTTOV levels and back again

The jagged Jacobians seen in the default interpolation scheme in RTTOV-10 when going from many levels (user) to fewer levels (RTTOV) have mainly been removed with new interpolation options. Work is on-going to improve this further.

Improved definition of RTTOV coefficient file levels for IR and MW radiometers

To ensure smooth jacobians the levels in the RTTOV coefficient files have been increased from 51 to 54 levels so that the layer thickness for all the layers are similar and follow an analytical expression.

New volcanic ash and Asian dust aerosol particle types.

New coefficient files now allow a more realistic simulation of infrared scattering by volcanic ash and Asian dust particles.

New Baran parameterisation for ice particle optical parameters

A new ice cloud parameterisation for the infrared which only depends on cloud top temperature and ice water content provides improvements to the simulation of cirrus cloud effects.

Capability to include non-LTE effects for high resolution IR sounders

To modify the computed SWIR spectrum for stratospheric sounding channels to allow for non-LTE effects a simple parameterisation scheme has been implemented. Validation of this correction with observations remains to be done.

Option to treat surface as a Lambertian reflector for the reflected downwelling radiance

Over snow and sea-ice the reflection of downwelling radiation is thought to be more Lambertian than specular, the latter being the only option in RTTOV until now. An option to compute the Lambertian reflection for MW channels has been included in RTTOV-11. This should improve the simulation of MW radiances in the polar regions.

		RTTOV-11 Science and Validation Report	Doc ID : NWPSAF-MO-TV-032 Version : 1.1 Date : 16/8/13
---	---	---	--

PC-RTTOV can now be run over clear and cloudy ocean and for IASI PCs can now be computed for limited spectral bands

Two enhancements to the original PC-RTTOV implemented in RTTOV-10. Both clear and cloudy radiances over the ocean can now be computed as PCs. Secondly subsets of the IR spectrum can be chosen for the PC computation (e.g. LW, SWIR)

All IR coefficients updated with latest spectroscopy from LBLRTMv12.2 and AER 3.2

The latest underlying spectroscopic parameters are now used to compute the coefficients for the visible and IR sensors.

Updated SSU coefficients based on latest spectroscopy LBLRTMv12.0 and option to allow for changes in cell pressure.

A new capability to allow for changes in cell pressure of the SSU has been implemented. This remains to be verified using reanalyses.

Updated HIRS and AMSU-A spectral responses used to provide alternative coefficients which should be more accurate

Studies have show that the channel spectral responses both for HIRS and ASMU-A have shifted once in –orbit. To allow for this an alternate set of coefficient files are now available using these shifted spectral responses. This should result in reduced biases seen between observations and simulations.

Improvements to microwave scattering

Substantial improvements in scattering radiative transfer in the microwave can be obtained from updated coefficient files that will soon be made available through the NWP-SAF website. However, the default RTTOV-11 files do not yet benefit from these improvements.

5. Acknowledgements

The RTTOV-11 developments and validation described here were carried out as part of the EUMETSAT funded NWP-SAF activities by the Met Office, ECMWF and MétéoFrance. In addition contributions from several scientists, visiting and associate scientists are gratefully acknowledged. They are Sarah Millington (Met Office), Eva Borbas (CIMSS/UW) and Mark Liu (JCSDA/NOAA).

6. References

Baran A.J., Connolly P.J., Lee C. (2009). Testing an ensemble model of cirrus ice crystals using midlatitude in situ estimates of ice water content, volume extinction coefficient and the total solar optical depth. *J. Quant. Spectrosc. Radiat. Transfer* **110** 1579–1598.

Baran A.J., Connolly P.J., Heymsfield A.J., Bansemmer A. (2011). Using in situ estimates of ice water content, volume extinction coefficient, and the total solar optical depth obtained during the tropical ACTIVE campaign to test an ensemble model of cirrus ice crystals. *Q. J. Roy. Meteorol. Soc.* **137**: 199–218.

Baran, A. J., Cotton, R., Furtado, K., Havemann, S., Labonnote, L.-C., Marengo, F., Smith, A. and Thelen, J.-C. (2013), A self-consistent scattering model for cirrus. II: The high and low frequencies. *Q.J.Roy. Meteorol. Soc.* doi: 10.1002/qj.2193

Borbas E and Ruston B.C. (2010). The RTTOV UWiremis IR land surface emissivity module, *Report NWPSAF-MO-VS-042*, 24 pp.

		RTTOV-11 Science and Validation Report	Doc ID : NWPSAF-MO-TV-032 Version : 1.1 Date : 16/8/13
---	---	---	--

Brindley H.E., A.J. Geer and J.E. Harries (1999). Climate variability and trends in SSU radiances: a comparison of model predictions and satellite observations in the middle stratosphere, *J. Clim.*, **12**, 3197-3219.

Bucholtz A., (1995). Rayleigh-scattering calculations for the terrestrial atmosphere. *Applied Optics*, **34**, 15, 2765-2773.

Carrer D, Roujean J-L, Meurey C. (2010). Comparing Operational MSG/SEVIRI Land Surface Albedo Products From Land SAF With Ground Measurements and MODIS. *IEEE Trans. Geosci. Remote Sens.* **48**: 1714–1728.

Chen, Y., Y. Han, P. van Delst, and F. Weng, 2013: Assessment of Shortwave Infrared Sea Surface Reflection and Nonlocal Thermodynamic Equilibrium Effects in Community Radiative Transfer Model Using IASI Data. *J. Atmos. Oceanic Technol.* doi:10.1175/JTECH-D-12-00267.1, in press

Chevallier F, Di Michele S, McNally AP. (2006). Diverse profile datasets from the ECMWF 91-level shortrange forecasts. *NWP SAF Report No. NWPSAF-EC-TR-010*.

Clough, S. A., M. W. Shephard, E. J. Mlawer, J. S. Delamere, M. J. Iacono, K. Cady-Pereira, S. Boukabara, and P. D. Brown (2005). Atmospheric radiative transfer modeling: a summary of the AER codes, Short Communication, *J. Quant. Spectrosc. Radiat. Transfer*, **91**, 233-244.

Coudert, L. H., Wagner, G., Birk, M., Baranov, Yu I., Lafferty, W. J., and Flaud, J-M. (2008). The H216O molecule: Line position and line intensity analyses up to the second triad, *J. Mol. Spectrosc.*, doi:10.1016/j.jms.2008.03.021.

Deng M., Mace GG, Wang Z, Okamoto H. 2010. Tropical Composition, Cloud and Climate Coupling Experiment validation for cirrus cloud profiling retrieval using CloudSat radar and CALIPSO lidar, *J. Geophys. Res.* 115 : D00J15, DOI:10.1029/2009JD013104.

Gao F, Schaaf C, Strahler A, Roesch A, Lucht W, Dickinson R. 2005. MODIS bidirectional reflectance distribution function and albedo Climate Modeling Grid products and the variability of albedo for major global vegetation types. *J. Geophys. Res.* **110** : D01104, DOI:10.1029/2004JD005190.

DeSouza-Machado, S. G., L. L. Strow, S. E. Hannon, H. E. Motteler, M. Lopez-Puertas, B. Funke, and D. P. Edwards, 2007: Fast forward radiative transfer modeling of 4.3 μm nonlocal thermodynamic equilibrium effects for infrared temperature sounders. *Geophys. Res. Lett.*, **34** 5 pages

Edwards, D., 1992: GENLN2: A general line-by-line atmospheric transmittance and radiance model. *NCAR Tech. Note 367+STR, Natl. Cent. for Atmos. Res., Boulder, Colo.*

Eyre J.R. and H.M. Woolf 1988: Transmittance of atmospheric gases in the microwave region: a fast model. *Applied Optics* **27** 3244-3249

Eyre J.R. 1991: A fast radiative transfer model for satellite sounding systems. *ECMWF Research Dept. Tech. Memo.* **176** Available at http://www.ecmwf.int/publications/library/ecpublications/_pdf/tm/001-300/tm176.pdf

Field, P. R. and Andrew J. Heymsfield and Aaron Bansemer, 2007: Snow Size Distribution Parameterization for Midlatitude and Tropical Ice Clouds, *J. Atmos. Sci.*, **64**, 4346-4365

Funke, B., M. López-Puertas, M., García-Comas, M. Kaufmann, M. Höpfner, and G. P. Stiller, 2012: GRANADA: A Generic Radiative traNsfer AnD non-LTE population algorithm. *J. Quant. Spectrosc. Radiat. Transfer*, **113**, 1771–1817.

Geer, A. and Baordo (2013) Improved scattering radiative transfer for frozen hydrometeors at microwave frequencies. *To be submitted to Quart. J. R. Met. Soc.*

		RTTOV-11 Science and Validation Report	Doc ID : NWPSAF-MO-TV-032 Version : 1.1 Date : 16/8/13
---	---	---	--

Geiger B, Carrer D, Franchisteguy L, Roujean J-L, Meurey C. (2008). Land Surface Albedo Derived on a Daily Basis From Meteosat Second Generation Observations. *IEEE Trans. Geosci. Remote Sens.* **46** 3841 – 3856.

Guedj, S.; Karbou, F.; Rabier, F.; Bouchard, A. (2010). Toward a Better Modeling of Surface Emissivity to Improve AMSU Data Assimilation Over Antarctica, *Geoscience and Remote Sensing, IEEE Transactions on Geoscience and Remote Sensing*, **48**, no.4, pp.1976-1985, doi: 10.1109/TGRS.2009.2036254

Han, H.-J., B.-J. Sohn, H.-L. Huang, E. Weisz, R. Saunders, and T. Takamura, (2012). An improved radiance simulation for hyperspectral infrared remote sensing of Asian dust, *J. Geophys. Res.*, **117**, D09211, doi:10.1029/2012JD017466.

Harlow, RC, (2009). Millimeter microwave emissivities and effective temperatures of snow covered surfaces: Evidence for Lambertian surface scattering, *IEEE. Trans. Geosci. Remote Sens.*, **47**(7): 1957-1970.

Harlow, RC (2011). Sea ice emissivities and effective temperatures at AMSU-B frequencies: An analysis of airborne microwave data measured during two Arctic campaigns, *IEEE Trans. Geosci. Remote Sens.*, **49**, no. 4, pp. 1223 - 1237, April 2011.

Johnson, B., K. Turnbull, P. Brown, R. Burgess, J. Dorsey, A. J. Baran, H. Webster, J. Haywood, R. Cotton, Z. Ulanowski, E. Hesse, A. Woolley, and P. Rosenberg (2012), In situ observations of volcanic ash clouds from the FAAM aircraft during the eruption of Eyjafjallajökull in 2010, *J. Geophys. Res.*, **117**, D00U24, doi:10.1029/2011JD016760.

Kobayashi, S., Matricardi, M., Dee, D. and Uppala, S. (2009) Towards a consistent reanalysis of the upper stratosphere based on radiance measurements from SSU and AMSU-A. *Quart. J. R. Met. Soc.*, **135**1, 2086-2099.

Kulie, M.S and R. Bennartz, T. J. Greenwald, Y. Chen and F. Weng, (2010) Uncertainties in microwave properties of frozen precipitation: implications for remote sensing and data assimilation. *J. Atmos. Sci.*, **67**, 3471-3487.

Lamouroux, J., H. Tran, A. L. Laraia, R. R. Gamache, L. S. Rothman, I. E. Gordon, J.-M. Hartmann, Updated database plus software for line-mixing in CO₂ infrared spectra and their test using laboratory spectra in the 1.5-2.3 μm region, (2010) *J. Quant. Spectrosc. Radiat. Transfer*, DOI: 10.1016/j.jqsrt.2010.03.006, 2010.

Liu, G. (2008). A database of microwave single-scattering properties for nonspherical ice particles, *Bull. Am. Met. Soc.*, **111**, 1563-1570.

Liu J, Schaaf CB, Strahler AH, Jiao Z, Shuai Y, Zhang Q, Roman M, Augustine JA, Dutton EG. (2009). Validation of Moderate Resolution Imaging Spectroradiometer (MODIS) albedo retrieval algorithm: Dependence of albedo on solar zenith angle. *J. Geophys. Res.* **114** : D01106. DOI:10.1029/2008JD009969

Lopez-Puertas, M., and F. Taylor. (2001) NONLTE Radiative Transfer in the Atmosphere. *World Scientific Publishing Company*.

Lucht W, Schaaf CB, Strahler AH. (2000). An Algorithm for the retrieval of albedo from space using semiempirical BRDF models. *IEEE Trans. Geo. Rem. Sens.* **38**: 977–998.

Matricardi, M. (2003) RTIASI-4, a new version of the ECMWF fast radiative transfer model for the infrared atmospheric sounding interferometer. *ECMWF Tech Memo* **425**.

Matricardi, M., Chevallier F, Kelly G, Thepaut J-N 2004: An improved general fast radiative transfer model for the assimilation of radiance observations. *Q. J. Roy. Meteorol. Soc.* **130** 153-173

Matricardi, M. 2005 The inclusion of aerosols and clouds in RTIASI, the ECMWF fast radiative transfer

		RTTOV-11 Science and Validation Report	Doc ID : NWPSAF-MO-TV-032 Version : 1.1 Date : 16/8/13
---	---	---	--

model for the infrared atmospheric sounding interferometer. *ECMWF Tech. Memo.* **474**.

Matricardi M. 2010: A principal component based version of the RTTOV fast radiative transfer model. *Q. J. Roy. Meteorol. Soc.* **136** 1823-1835.

Matricardi M and T. McNally 2011: The direct assimilation of IASI short wave principal component scores into the ECMWF NWP model. *EUMETSAT Contract No. EUM/CO/07/460000475/PS*.

Matricardi M. and McNally 2013a: The direct assimilation of Principal Components of IASI spectra in the ECMWF 4D-Var. *Q. J. Roy. Meteorol. Soc.* doi: 10.1002/qj.2156

Matricardi M and T. McNally 2013b: The direct assimilation of principal components of IASI spectra in the ECMWF 4D-Var: extension to IASI band 1 and IASI band 2. *EUMETSAT Contract No. EUM/CO/07/460000475/PS*.

Matzler, C. 2005 On the determination of surface emissivity from Satellite observations. *Geoscience and Remote Sensing Letters*, **2**, 160-163.

Millington, S. C., R. W. Saunders, P. N. Francis, and H. N. Webster (2012), Simulated volcanic ash imagery: A method to compare NAME ash concentration forecasts with SEVIRI imagery for the Eyjafjallajökull eruption in 2010, *J. Geophys. Res.*, **117**, D00U17, doi:10.1029/2011JD016770.

Petty, G. W. and Wei Huang, 2010: Microwave backscatter and extinction by soft ice spheres and complex snow aggregates, *J. Atmos. Sci.*, **67**, 769-787.

Pollack, J. B., O. B. Toon, and B. N. Khare (1973), Optical properties of some terrestrial rocks and minerals, *Icarus*, **19**, 372–389, doi:10.1016/0019-1035(73)90115-2.

Ridgway, W. L., R. A. Moose, and A. C. Cogley (1982) Atmospheric transmittance/radiance computer code FASCOD2. *SONICRAFT INC CHICAGO IL, Defense Technical Information Center, 1981*.

Rochon, Y.J., L. Garand, D.S. Turner, and S. Polavarapu, 2007: Jacobian mapping between vertical coordinate systems in data assimilation, *Q. J. Roy. Meteorol. Soc.* **133** 1547-1558.

Rothman, L. S., et al. (2009) The HITRAN 2008 molecular spectroscopic database, *Journal of Quantitative Spectroscopy and Radiative Transfer*, **110**, Issues 9–10, 533-572, DOI:10.1016/j.jqsrt.2009.02.013, 2009.

R7REP2002 RTTOV-7 science and validation report available at:
http://research.metoffice.gov.uk/research/interproj/nwpsaf/rtm/rttov7_svr.pdf

R8REP2006 RTTOV-8 science and validation report available at:
http://research.metoffice.gov.uk/research/interproj/nwpsaf/rtm/rttov8_svr.pdf

R9REP2008 RTTOV-9 science and validation report available at:
http://research.metoffice.gov.uk/research/interproj/nwpsaf/rtm/rttov9_files/rttov9_svr.pdf

R10REP2010 RTTOV-10 science and validation report available at:
http://research.metoffice.gov.uk/research/interproj/nwpsaf/rtm/docs_rttov10/rttov10_svr_1.11.pdf

Saunders R.W., M. Matricardi and P. Brunel 1999a: A fast radiative transfer model for assimilation of satellite radiance observations - RTTOV-5. *ECMWF Research Dept. Tech. Memo.* **282** (available from <http://www.ecmwf.int/publications/library/do/references/list/14>).

Saunders R.W., M. Matricardi and P. Brunel 1999b: An Improved Fast Radiative Transfer Model for Assimilation of Satellite Radiance Observations. *Q. J. Roy. Meteorol. Soc.*, **125**, 1407-1425.

<p>The EUMETSAT Network of Satellite Application Facilities</p>		<p>RTTOV-11 Science and Validation Report</p>	<p>Doc ID : NWPSAF-MO-TV-032 Version : 1.1 Date : 16/8/13</p>
---	---	---	---

Strow, L.L., Hannon, S.E., Souza-Machado, S.D., Motteler, H.E., Tobin, D., 2003. An Overview of the AIRS Radiative Transfer Model. *IEEE Trans. on Geoscience and Remote Sensing*, 41, 2, 303-313.

Taylor F.W., J.T. Houghton, G.D. Peskett, C.D. Rodgers and E.J. Williamson, (1972). Radiometer for Remote Sensing in the Upper Atmosphere. *Applied Optics*, 11, 135-141.

Vidot J and Borbas E, 2013. Land surface VIS/NIR BRDF atlas for RTTOV-11: Model and Validation against SEVIRI Land SAF Albedo product. *Submitted to Q. J. R. Meteorol. Soc.*

Volz, F. E. (1972), Infrared refractive index of atmospheric aerosol substances, *Appl. Opt.*, 11, 755–759, doi:10.1364/AO.11.000755.

Volz, F. E. (1973), Infrared optical constants of ammonium sulfate, Sahara dust, volcanic pumice, and flyash, *Appl. Opt.*, 12, 564–568, doi:10.1364/AO.12.000564.

End of report